# Snow transport in extreme environments: from small to large scale modeling

## Daniela BRITO MELO

École
polytechnique
fédérale
de Lausanne

2023

Once you start looking at snow,
you cannot stop.
— Charles Fierz

To Pedro,
the ghost co-author of everything I do

# Acknowledgements

My first words of appreciation go to my supervisor, Prof. Michael Lehning, who supported me and believed in me during these years. I am deeply grateful for his guidance and encouragement whenever I needed, for all the long scientific discussions, for always being open to my ideas, and for giving me the opportunity to make this thesis what I wanted it to be.

Moreover, I would like to express my deepest appreciation to Varun Sharma, Franziska Gerber, Alec Petersen, Armin Sigmund, Francesco Comola, and Charles Amory, without whom this work would not have been possible. Thank you, Varun and Fränzi, for working tirelessly with me and for your constant support, availability, and kindness. Thank you, Alec, for being my wind tunnel partner, for guiding me in the world of experimental analysis, and for making all of this so much fun. Thank you, Armin, for always being available to discuss and collaborate with me - I deeply value our exchange of ideas, and for being a constant and trustful presence throughout this PhD. Thank you, Francesco, for your initial guidance, for putting me up-to-speed with the physics of saltation, and for all the writing tips. Finally, thank you, Charles, for collaborating in the analysis of the experimental data you have collected, for your availability to discuss, and for your constant encouragement.

I am also grateful to Prof. Filippo Coletti for his part in making the wind tunnel adventure possible and for all the interesting discussions. Many thanks also to Benjamin Walter and Matthias Jaggi for their support on the wind tunnel and field experiments.

I am also thankful to all the CRYOS-SLF team (current and previous members) for all the good moments and adventures since day 1. In this regard, special thanks to Adrien, Tatjana, Mahdi, and Shokoufeh for their friendship and warmth. Thank you as well to the administrative personnel of CRYOS, Jessica and Isabelle, for their support and care, and to the members of the SLF workshop, for always finding a way to communicate with me and for their collaboration during my stay in Davos.

In addition, I could not have undertaken this journey without Pedro, the ghost co-author of everything I do. Thank you for all the nights and weekends discussing snow saltation, for all the time you have dedicated to my manuscripts, and for being by my side, always and tirelessly.

Thanks should also go to my family and friends back home, in particular to my loving parents whose love I feel everyday, to my brother who always finds a way to make me stop complaining

**Acknowledgements**

and send me back to work, to my parents-in-law who have also embraced this journey with love and joy, to my little cousins Madalena and Duarte for forgiving me for moving far away from them and for keep loving me nonetheless, and to Maria, my PhD-sister, for being such an inspiration for me and for boosting my confidence so many times.

Lastly, I would like to acknowledge the snow scientific community for their openness to discussion and for providing extra clarifications about their work whenever I have requested.

*Lausanne, 26 July 2023*                                                                                           D. B. M.

# Abstract

The cold regions on Earth, such as the polar and high mountain regions, are snow covered for at least a part of the year. These snow-covered surfaces are highly dynamic, particularly under the influence of strong winds. The aeolian or wind-driven transport of snow occurs when the wind is sufficiently strong to lift the snow particles from the surface. It controls the mass balance of the snowpack under windy conditions and influences the sublimation of snow and ice surfaces. Despite its importance, the representation of snow transport in climate models has high uncertainties because the associated physical processes are complex and highly variable in space and time. One of the main challenges is the accurate representation of snow transport close to the ground, where snow particles are transported by a process called saltation. This shallow layer can comprise most of the horizontal mass flux and sets the lower boundary condition for modeling snow suspension clouds.

In order to investigate the complex wind-particle-bed interactions characteristic of snow particles in saltation, we use a Large Eddy Simulation flow solver coupled with a Lagrangian model that describes the particles trajectory and their interaction with the snow surface. In particular, the model is used to study the influence of snow surface properties on snow saltation dynamics, as well as the validity of the parameterizations used in large-scale models. It is confirmed that interparticle cohesion and grain size heterogeneity can increase the overall saltation mass flux at high friction velocities. Moreover, some simplified models agree reasonably well with the simulations for given bed characteristics, while others clearly do not. In addition, we show that the prevailing parameterizations that describe the saltation system in atmospheric models are based on contradictory assumptions: while some scaling laws are typical of a saltation system dominated by aerodynamic entrainment, others represent a saltation system controlled by splash. Using numerical simulations, we show that both regimes can exist, depending on the friction velocity.

These findings are used to improve the coupled atmosphere-snowpack model CRYOWRF. The parameterizations employed are adjusted so that they become consistent with the current understanding on snow saltation dynamics. By so doing, the comparison between simulation results and mass flux measurements is significantly improved.

This work offers a comprehensive analysis of the snow saltation system and its scaling laws, and showcases how detailed numerical models can be used to improve large-scale models

## Abstract

of snow transport and sublimation. These efforts improve the understanding of the physical phenomena taking place at the polar and high mountain regions, and contribute to a more accurate assessment of the surface mass balance at those sites.

**Keywords**: Snow transport, snow saltation, surface mass balance, polar regions, high-mountain regions, LES, CRYOWRF

# Résumé

Les régions froides de la Terre, telles que les régions polaires et les hautes montagnes, demeurent enneigées une partie significative de l'année. Ces surfaces enneigées sont assez dynamiques, notamment sous l'influence de vents forts. Le transport éolien de la neige survient lorsque la force du vent est suffisamment élevée. Il gouverne le bilan massique du manteau neigeux en conditions venteuses et influence la sublimation de neige et de glace. Malgré son importance, la représentation du transport de neige dans les modèles climatiques comporte des incertitudes significatives, principalement en raison de la complexité des phénomènes hautement variables dans l'espace et le temps. L'un des défis majeurs réside dans la représentation du transport de neige à proximité du sol où les particules sont transportées par un processus dénommé saltation. Cette fine couche peut englober la majorité du flux massique horizontal et établit la condition limite inférieure pour la modélisation de la neige en suspension.

Afin d'étudier les interactions entre le vent, les particules et le manteau neigeux, nous utilisons un solveur LES (*Large Eddy Simulation*) couplé à un modèle lagrangien décrivant la trajectoire des particules et leur interaction avec la surface de neige. Ce modèle est employé pour étudier l'influence des propriétés de la neige sur la dynamique de la saltation, ainsi que la validité des paramétrisations utilisées dans les modèles à grande échelle. Les résultats confirment que la cohésion entre les particules et l'hétérogénéité de leurs dimensions peuvent accroître le flux massique horizontal de particules lorsque la vitesse de frottement est élevée. En outre, certains modèles simplifiés s'accordent bien avec les simulations, tandis que d'autres dévient clairement. D'autre part, nous démontrons que les paramétrisations décrivant le système de saltation dans les modèles atmosphériques reposent sur des hypothèses contradictoires : certaines se basent sur des lois caractéristiques d'un système de saltation dominé par l'entraînement aérodynamique, tandis que d'autres décrivent un système contrôlé par l'éjection de particules. À l'aide de simulations, nous mettons en évidence l'existence de ces deux régimes en fonction de la vitesse de frottement.

Les résultats sont utilisés pour améliorer le modèle atmosphère-manteau neigeux CRYOWRF et les paramétrisations implémentées sont corrigées. Par conséquent, la comparaison entre les résultats des simulations et les mesures de flux massique est significativement améliorée. Cette étude fournit une analyse exhaustive du phénomène de saltation de neige et de ses lois

physiques. En outre, nous démontrons comment des modèles numériques détaillés peuvent être utilisés pour améliorer les modèles de transport et sublimation à grande échelle. Ces efforts permettent une meilleure compréhension des phénomènes physiques se produisant dans les régions polaires et en haute montagne, tout en contribuant à une évaluation plus précise du bilan de masse de ces régions.

**Mots clefs :** transport éolien de la neige, saltation, bilan de masse du manteau neigeux, régions polaires, hautes montagnes, LES, CRYOWRF

# Contents

# List of Figures

# List of Tables

# 1 Introduction

**Why study snow and its interaction with the wind?**

Snow-covered regions on Earth are mainly located at high latitudes of the Northern Hemisphere, high mountain areas, and in Antarctica. Every year, the extent of the snow cover in the Northern Hemisphere reaches a total of approximately 47 million km$^2$, which corresponds to 18% of its surface area (Robinson & Estilow, 2021). Due to its extent and high reflectivity (albedo), snow reflects a significant part of the incoming solar radiation back to space and, therefore, plays an important role on the global climate system. In addition, snow is characterized by a low thermal conductivity, which protects the underlying ground and its living organisms from cold air temperatures (Maccario et al., 2015). Seasonal snow in mountain ranges worldwide is also a vital source of fresh water, which is stored during winter and released during spring. The water that results from snow melt is required for domestic use, agriculture, and hydropower production, among others (e.g., Boisramé & Carroll, 2023; Tobias et al., 2023; Zhang et al., 2023). In some countries, snow is an important asset for the tourism industry, but also a risk to the safety of people and infrastructure due to the occurrence of avalanches (Ortner et al., 2023). The study of snow and its dynamics is, therefore, a multidisciplinary field, which captures the attention of climatologists, hydrologists, and engineers, to mention just a few. Taking into account the key role of snow in so many aspects of life on Earth and its sensitivity to a changing climate, it is not surprising that its study has attained even greater importance over the last decade.

The study of the geophysical processes taking place in the polar and high mountain regions is particularly challenging due to their remoteness and extreme atmospheric conditions. These challenging conditions for scientists and measurement instruments hinder the complete understanding and quantification of the different phenomena taking place at those sites. For instance, the number and geographical distribution of on-site measurements of meteorological quantities and of the status of the snow cover are limited, which has negative consequences for the development and validation of analytic and numerical models. As a result, the existing atmospheric and snow models are yet unable to fully represent the dynamics of the snowpack and to accurately predict the accumulation and depletion of snow and ice. These quantities

influence the surface mass balance of big ice sheets like Antarctica and Greenland, whose mass loss can have a significant impact on sea level rise.

The surface mass balance of snow-covered regions is the difference between the processes leading to a mass gain (mainly precipitation) and those that lead to a mass loss (e.g., melting and sublimation). In addition to the mentioned processes, the aeolian or wind-driven transport of snow, generally named drifting or blowing snow, is yet another contributor to the surface mass balance. This phenomenon occurs when the wind velocity is sufficiently high to lift the snow particles from the surface. During snow transport events, the wind flow erodes the snowpack in the most exposed regions and leads to snow re-deposition in sheltered areas. Therefore, snow transport can be both a positive and a negative contributor to the surface mass balance. The wind flow also interacts with falling snow, which leads to the preferential deposition of precipitation (Lehning et al., 2008).

The impact of the aeolian transport of snow on the mass and energy balances of a snow cover is manifold. On the one hand, the transport of snow by the wind increases the snow height heterogeneity and leads to the formation of bedforms, like sastrugi, dunes, ripples (Filhol & Sturm, 2015), as well as cornices at the leeward side of mountain crests (Hancock et al., 2020; Yu et al., 2023). This influences the surface roughness and, therefore, the near-surface flow and the advective heat fluxes. On the other hand, during snow transport events, snow sublimation is enhanced because the snow particles aloft are more exposed to the dry air flow (Dai & Huang, 2014; Déry et al., 1998; Liston & Sturm, 2004). In addition to the snow mass loss, the sublimation of snow particles aloft impacts the near-surface temperature and moisture fields.

At local scales, the snow height variability induced by snow erosion and re-deposition hinders the assessment of snow precipitation from direct snow height observations (Mott & Lehning, 2010). In addition, the top layer of the snow cover becomes harder and denser due to the deposition of snow particles that were previously aloft (Sommer et al., 2018). This influences the ability of the wind to re-mobilize the snow and has implications for the occurrence of avalanches (Lehning et al., 2008). Regarding the latter, the compact snow layer that forms during snow transport events can become an additional slab on top of a weak layer, which mechanical failure can lead to avalanche release (Gaume & Puzrin, 2021). Moreover, the snow erosion that occurs on the windward side of mountain crests can decrease the distance between the snow surface and a potentially buried weak layer, which influences the stability of the slope. At the catchment scale, snow redistribution affects the water budget and the snow melt runoff patterns, which are of great importance for water management (Pomeroy & Gray, 1990).

**The need to improve large scale models**

The terms drifting and blowing snow are commonly used to distinguish between weak and strong snow transport events. During drifting snow events, it is frequently assumed that the

snow particles do not rise above 2 m height above the ground, while during blowing snow events the snow grains are expected to reach higher regions of the atmosphere (AMS American Meteorological Society, 2012). Nevertheless, in order to simplify the nomenclature, the term blowing snow is preferred throughout the text to designate snow transport events. These events are very frequent in Antarctica, specifically in the coastal areas, which are subjected to strong katabatic winds throughout the year (Lenaerts et al., 2012; Palm et al., 2017). Blowing snow sublimation is also maximum along the coast due to the higher temperatures and lower values of relative humidity in comparison with the Antarctic plateau (Gallée, 1998; Gerber et al., 2023; Palm et al., 2017). On average, the Antarctic surface mass balance is controlled by snowfall, but snow sublimation is the main mass ablation process (Gerber et al., 2023; Lenaerts et al., 2012; Palm et al., 2017). In some regions of East Antarctica, like the Neumayer station and Adélie Land, blowing snow sublimation removes approximately 17% and 19% of the snowfall, respectively (Lenaerts & van den Broeke, 2012; van den Broeke et al., 2010). In Terra Nova Bay, East Antarctica, snow transport is expected to remove up to 50% of the snowfall due to the combination of blowing snow sublimation and the transport of snow particles to the ocean (Scarchilli et al., 2010). In addition, clouds of blowing snow particles with a height of hundreds of meters have been observed in Antarctica (Palm et al., 2017). They are expected to influence the radiative budget and the cloud properties (Hofer et al., 2021).

The contribution of blowing snow transport and sublimation to the surface mass balance mentioned above can only be quantified if these processes are captured in large-scale atmospheric models. The early model of Pomeroy (1989) represented an important step in this direction, followed by the works of Gallée (1998) and Déry et al. (1998). Today, blowing snow schemes can be found in several atmospheric models (Amory et al., 2021; Lenaerts et al., 2012; Sharma et al., 2023; van Wessem et al., 2018; Vionnet et al., 2014), as well as in distributed snow models, which use a prescribed wind velocity field as an input to the model (Lehning et al., 2008).

However, despite its importance and the different modeling advancements, the contribution of blowing snow transport and sublimation to the surface mass balance of snow-covered regions is still challenging to predict. For example, while the regional atmospheric model RACMO (van Wessem et al., 2018) estimates a total of $102 \pm 5$ Gt y$^{-1}$ of blowing snow sublimation over the Antarctic continent (except the Antarctic Peninsula), the amount of blowing snow sublimation derived from satellite observations (Palm et al., 2017) over the Antarctic continent (except the region south of the 82°S parallel) yielded $393 \pm 196$ Gt y$^{-1}$. The estimates of blowing snow transport and sublimation obtained with models and measurements often disagree, which highlights the need to improve the snow transport formulations implemented in atmospheric models.

**Snow saltation: the bottleneck in the modeling of snow transport**

The motion of snow particles is generally conceptualized in three modes: creep, saltation, and suspension (Bagnold, 1941). Creep corresponds to the rolling and sliding of snow particles, or to small hops with a maximum height of approximately the particle diameter. Creeping

particles are typically too large and heavy to be lifted by the wind. Saltation defines the ballistic motion of snow particles close to the surface, with a maximum height of no more than 10 to 15 cm (Gordon et al., 2009). These particles are either lifted by the turbulent flow (aerodynamic entrainment) or ejected by an impacting snow particle (splash). After impacting the surface, the saltating particles might deposit or bounce off into a new trajectory (rebound). This region close to the surface where most particles are transported in saltation is named the saltation layer. Suspension is the motion of small snow particles transported above the saltation layer. These particles are advected by the wind for long distances and up to high regions of the atmospheric boundary layer.

The general approach in atmospheric and snow models is to parameterize the snow particle concentration and mass flux in the saltation layer and to compute the spatial and temporal distribution of snow particles in suspension by taking into account horizontal particle advection, particle settling, and vertical turbulent mixing of particles aloft (Amory et al., 2021; Lehning et al., 2008; Sharma et al., 2023; van Wessem et al., 2018; Vionnet et al., 2014). The bottom boundary of the snow suspension scheme is defined at the top of the saltation layer, where particle concentration is specified as a function of the near-surface wind velocity and some snow surface characteristics. The contribution of creep to the mass flux of snow particles is either neglected or assumed to be included in the snow saltation parameterization. Snow sublimation is usually estimated with the model of Thorpe and Mason (1966). The process of snow sublimation extracts heat and adds moisture from/to the near-surface flow, which is generally taken into account in the energy and moisture budgets of the near-surface atmosphere.

Shortcomings in the modeled blowing snow mass flux and sublimation can be related to uncertainties in the input parameters, such as the near-surface wind velocity, which greatly depends on the description of the surface topography (Lenaerts et al., 2012; Mott & Lehning, 2010; Raderschall et al., 2008), or to inaccuracies in the blowing snow scheme itself. In fact, and concerning the latter, it seems that the resultant quantities of interest are significantly sensitive to the snow saltation parameterizations that are used. For instance, using the atmospheric model MAR, Amory et al. (2021) obtained an improved agreement between the simulated and measured blowing snow mass fluxes at D47 (Adélie Land, Antarctica) mainly by adjusting the minimum shear stress exerted by the flow that leads to the onset of snow drift. Another example can be given, this time with the atmospheric model RACMO: van Wessem et al. (2018) reduced the computed blowing snow sublimation over the Antarctic continent (except the Antarctic Peninsula) from $181 \pm 9$ Gt y$^{-1}$ to $102 \pm 5$ Gt y$^{-1}$ by halving the snow particle concentration at the top of the saltation layer. The parameters discussed in these two examples influence the frequency of blowing snow events and the total mass flow rate of particles in suspension. Moreover, they significantly affect the rate of blowing snow sublimation.

**Challenges and solutions**

As discussed above, a rigorous description of snow saltation in atmospheric models is of the utmost importance to model blowing snow mass flux and sublimation. However, its devel-

opment has been often overlooked. The saltation models commonly used in the mentioned atmospheric and snow models rely on simple analytic equations based on the assumption of steady-state saltation, that is, an equilibrium state between the grains in motion and the wind field (Doorschot & Lehning, 2002; Pomeroy & Gray, 1990; Sørensen, 2004). For instance, the early model of Pomeroy and Gray (1990) has been used in the blowing snow schemes of RACMO (Lenaerts et al., 2012; van Wessem et al., 2018) and MAR (Amory et al., 2015; Amory et al., 2021), while a different approach, based on the model on Sørensen (2004), was considered in the atmospheric model Meso-NH (Vionnet et al., 2014). The latter was also adopted by Sharma et al. (2023) when coupling the Weather Research and Forecasting model (WRF) (Skamarock et al., 2019) with a blowing snow scheme and the snow model SNOWPACK (Lehning et al., 1999). These various saltation models consider different simplifying assumptions and parameters. They disagree on key aspects of the saltation dynamics, such as the scaling of the particle mass flux with the wind speed. In addition, the parameters used are based on a limited number of experimental measurements. Therefore, they are unable to characterize snow saltation over a variety of snow surfaces. In fact, no detailed assessment regarding the validity of these different models, simplifying assumptions and parameters exists in the literature. Therefore, the accuracy of the snow saltation models implemented in blowing snow schemes is still largely unknown.

The complexity of modeling snow saltation is related to the turbulent flow features and the snow particle characteristics. In contrast with sand beds, snow beds change continuously: soon after deposition, snow grains form interparticle ice bonds between each other; the characteristics of a snow bed (for instance, particle size distribution, interparticle bonds, and grain shape) evolve with time due to metamorphic processes; and snow particle size and shape change during saltation events due to fragmentation (Comola et al., 2017) and sublimation (Sharma et al., 2018).

Detailed models of saltation allow us to simulate both the flow and snow bed particularities. By approximately resolving the turbulent flow, particle trajectories and surface processes, these models can be used to improve our understanding of particle-wind interaction and to evaluate some of the assumptions made in simple saltation models. In the last two decades, Reynolds-Averaged Navier-Stokes (RANS) and Large Eddy Simulation (LES) flow solver techniques were used, coupled with Lagrangian models for particle dynamics (e.g., Almeida et al., 2006; Dupont et al., 2013; Groot Zwaaftink et al., 2014; Okaze et al., 2018; Shao & Li, 1999). Moreover, splash laws based on conservation principles were also proposed and used to describe steady-state saltation (Comola & Lehning, 2017; Kok & Renno, 2009; Lämmel et al., 2017).

Sophisticated measurement techniques based on imaging and particle tracking algorithms have provided detailed observations of near-surface particle motion and insight into the role played by high-frequency wind turbulence on snow saltation dynamics (e.g., Aksamit & Pomeroy, 2016, 2018; Groot Zwaaftink et al., 2014; Paterna et al., 2016, 2017). In particular, Paterna et al. (2016) have shown some evidence that velocity fluctuations significantly influence the vertical mass flux of saltating snow. Aksamit and Pomeroy (2018) have observed that

both low- and high-frequency turbulence structures impact snow saltation dynamics. These findings strongly support the need for an accurate description of the turbulent flow field when modeling the wind-particle interaction intrinsic to snow saltation.

Recent theoretical and numerical advances (Comola, Gaume, et al., 2019; Comola & Lehning, 2017) have shed light on the role played by granular bed properties, such as grain size distribution and interparticle cohesion, in granular splash mechanisms. In addition, field measurements of snow saltation (Aksamit & Pomeroy, 2016) have shown that the snow surface hardness influences the mean vertical profiles of particle velocity and mass flux during intermittent saltation. However, the effect of snow surface properties on saltation development and scaling laws is still largely unknown. For example, there are no quantitative estimates on how particle size distribution and interparticle cohesion influence particle speed and surface shear stress during saltation. Consequently, the effect of surface properties on the particle mass flux is still unclear.

Detailed numerical models based on RANS or LES cannot be used in atmospheric models, which require simple and computationally inexpensive algorithms. Nevertheless, they provide an excellent test bench to fully understand the implications of the simplifying assumptions that are used and to evaluate the errors they might introduce. In particular, the Large Eddy Simulation - Lagrangian Stochastic Model (LES-LSM) (Comola, 2017), which couples an LES flow solver with a Lagrangian model to simulate the particle trajectories and the surface processes of aerodynamic entrainment, rebound, and splash, is a remarkable tool for this investigation.

Improvements in the modeling of snow transport in large-scale models can be achieved through the upscaling of these numerical models that simulate the complex particle-fluid-bed interactions. For instance, the atmospheric model CRYOWRF (Sharma et al., 2023) can gain from these new developments. Taking into account that it includes a detailed description of the snowpack structure, its blowing snow scheme is potentially able to simulate both the effect of the wind velocity and of the snow surface characteristics on the frequency and intensity of blowing snow.

**Objectives and thesis structure**

The main objective of this thesis is to improve large-scale estimates of the aeolian transport of snow. In order to pursue this goal, the saltation system is investigated using the different theoretical, numerical, and experimental findings existing in the literature (chapter 2), as well as LES-LSM numerical simulations (chapters 3, 4 and 5). Finally, in chapter 6, the ability of the atmospheric model CRYOWRF to represent the frequency and intensity of blowing snow events is assessed, and improvements are proposed based on the previous findings. A short summary of each chapter is provided below:

- **Chapter 2:** A detailed analysis of the snow saltation parameterizations available in the

literature, as well as of the theoretical, numerical, and experimental arguments that support them is presented in this chapter. This exhaustive review brings to light some of the inconsistencies in the snow saltation parameterizations currently implemented in atmospheric models. In addition, it highlights the aspects of the snow saltation dynamics that are not yet fully understood and that need further investigation.

- **Chapter 3:** The LES-LSM model is presented and described. Particular attention is given to the modeling options and to the chosen simplifying assumptions. This discussion clarifies the capabilities and limitations of the model and supports the subsequent analysis of the simulation results. Moreover, it shows the need for further investigation in the field, in particular the development of experimental studies with natural snow. The experimental work presented in Appendix A is a result of such realization and a contribution in this realm.

- **Chapter 4:** The LES-LSM model is used to investigate the effect of the snow surface characteristics on the saltation dynamics. The ability of the model to simulate steady-state saltation and its detailed features is firstly shown. Then, the effect of grain size and interparticle cohesion on the different quantities of interest is discussed. By comparing the simulation results with the parameterizations proposed in the literature, conclusions are drawn about their ability to represent the saltation system.

- **Chapter 5:** The LES-LSM model is used to investigate the premises behind the snow saltation parameterizations and their relation with the dynamics of saltating snow. This analysis brings together the variety of scaling laws obtained with models and experiments and offers an explanation for the observed disagreement. In addition, it challenges a core assumption in saltation modeling related to the relative importance of aerodynamic entrainment in comparison to particle splash.

- **Chapter 6:** The CRYOWRF model is used to simulate the region around coastal Adélie Land, East Antarctica, for which extensive field measurements of blowing snow mass flux are available. The simulations are performed over one year in order to assess the ability of the model to represent the frequency and intensity of blowing snow events throughout different seasons. Based on the previous findings, the accuracy of the blowing snow scheme is discussed and modifications are proposed. It is shown that the proposed modifications significantly improve the comparison between simulations and measurements.

**Publications and author contributions**

- An edited version of chapters 2 and 5 is part of a manuscript which is currently under review at *The Cryosphere*:

  Melo, D. B., Sigmund, A., and Lehning, M. (2023). Understanding snow saltation parameterizations: lessons from theory, experiments and numerical simulations. *EGUsphere*, pages 1–37. https://doi.org/10.5194/egusphere-2023-488

DBM performed the simulations, implemented the post-processing scripts and made the literature review. DBM, AS and ML contributed to the analysis of the results. AS and DBM contributed to the code development and its maintenance. ML supervised the work and secured its funding. DBM prepared the manuscript with contributions from all co-authors.

- An edited version of chapters 3 and 4 is part of a peer-reviewed article published at the *Journal of Geophysical Research: Atmospheres*:

Melo, D. B., Sharma, V., Comola, F., Sigmund, A., and Lehning, M. (2022). Modeling snow saltation: The effect of grain size and interparticle cohesion. *Journal of Geophysical Research: Atmospheres*, 127, e2021JD035260. https://doi.org/10.1029/2021JD035260

DBM, VS and FC defined the scope and objectives of the article. DBM performed the simulations and the post-processing of the results. DBM, VS, FC, AS and ML contributed to the analysis of the results. ML supervised the work and secured its funding. DBM prepared the manuscript with contributions from all co-authors.

- An edited version of chapter 6 will be submitted for publication:

Melo, D. B., Gerber, F., Amory, C., Sigmund, A., Lehning, M. Modeling blowing snow with CRYOWRF at Adélie Land, East Antarctica. In preparation.

DBM and FG performed the simulations and the post-processing of the results. CA provided additional field measurements and guaranteed the correct interpretation of the data set. DBM, CA, ML, AS and FG contributed to the analysis of the results. ML supervised the work and secured its funding. DBM prepared the current version of the text.

# 2 Snow saltation parameterizations

In this chapter, the different snow saltation parameterizations available in the literature and their use in atmospheric models are presented and discussed. Focus is given to the most common approximations within the steady-state framework, as well as to the theoretical, numerical and experimental arguments that support them. After a short introduction about the steady-state assumption (section 2.1), the parameterizations used to compute the transport rate (section 2.2) and the vertical profiles of particle concentration, streamwise velocity and mass flux (section 2.3) are analyzed. These quantities are needed to compute the particle concentration at the top of the saltation layer - the lower boundary condition for the advection and diffusion of suspended particles. The main goal of this chapter is to highlight where consensus and disagreement exist in order to help the reader develop a critical view on the currently used snow saltation parameterizations. The main conclusions are summarized in section 2.4.

## 2.1 The steady-state assumption

Let us denote by $x$ [m], $y$ [m] and $z$ [m] the streamwise, crosswise and vertical directions, respectively, in a Cartesian coordinate system. In this reference frame, we consider a turbulent air flow driven by a constant streamwise pressure gradient over a flat, homogeneous and erodible surface. It is assumed that the wind field is statistically steady and that the time-averaged wind velocity do not vary along the streamwise and crosswise directions. Under these conditions, the saltation system is considered statistically steady and invariant along the horizontal directions (steady-state saltation).

Close to the surface and in the absence of saltating particles, the time-averaged fluid shear stress, $\tau = \rho_a u_*^2$ [Pa], can be assumed constant in height, where $\rho_a$ [kg m$^{-3}$] is the air density and $u_*$ [m s$^{-1}$] is the friction velocity (Prandtl, 1935). During saltation, there is an exchange of momentum between the fluid and the particles, which leads to a decrease in the fluid shear stress in the saltation layer (Owen, 1964; Raupach, 1991). Above the saltation layer, the time-averaged fluid shear stress is still well approximated by $\tau$, however, at the surface, it

reaches a smaller value denoted by $\tau_s = \rho_a u_{*,s}^2$ [Pa], where $u_{*,s}$ [m s$^{-1}$] is the surface friction velocity.

The assumption of steady-state saltation implies zero net erosion and deposition of particles from/on the granular bed. In this way, for a given friction velocity outside the saltation layer, $u_*$ (henceforth friction velocity), the rate at which particles are transported by the wind stays at an equilibrium value. The saltation system is therefore characterized by a self-regulatory behaviour: a local increase in the particle flow rate above its equilibrium value locally extracts more momentum from the wind, reducing its velocity; this decreases the ability of the air flow to accelerate the particles in saltation and, consequently, decreases the particle flow rate back to its equilibrium value (e.g., Bagnold, 1941; Owen, 1964).

The premises behind the steady-state saltation assumption contrast with the reality of snow-covered regions, which are rarely flat or homogeneous. In addition, the wind field in mountainous terrain can seldom be characterized as statistically steady. Nevertheless, steady-state saltation is frequently assumed, based on the notion that the saltation system can adapt very rapidly to changes in the wind velocity (e.g., Anderson et al., 1991). Wind tunnel and field measurements have revealed a strong coupling between the saltation system and the wind velocity fluctuations (Aksamit & Pomeroy, 2018; Paterna et al., 2016). However, these interactions cannot be represented in atmospheric models, which require simple and computationally light models that cannot capture the full complexity of the wind-particle interaction. In addition, the time scales of atmospheric models do not encompass the full wind field variability. In this context, when deriving snow saltation parameterizations for large-scale models, the assumption of steady-state saltation is regarded as a reasonable approximation.

## 2.2    The transport rate

The transport rate of saltating particles, $Q$ [kg m$^{-1}$ s$^{-1}$], corresponds to the flow rate of particles moving in saltation per unit width. From its definition, $Q$ can be computed by multiplying the mass of particles in saltation per unit surface area by the average particle streamwise velocity.

The transport rate can also be computed as a function of the wind field characteristics by performing a balance of linear momentum in the streamwise direction to the saltating particles and to the fluid flow. Let us assume that the only force applied to a given saltating particle in the streamwise direction is the aerodynamic force. In this case, the average aerodynamic force in the streamwise direction applied to a particle along a hop equals the average rate of change of the particle streamwise momentum, $m(v_x^i - v_x^e)/t_p$, where $m$ [kg] is the particle mass, $v_x^i$ [m s$^{-1}$] and $v_x^e$ [m s$^{-1}$] are the streamwise components of the particle velocity at impact and ejection from the surface, respectively, and $t_p$ [s] is the duration of the particle hop (Figure 2.1a). The balance of linear momentum in the streamwise direction applied to the fluid flow is simplified by assuming steady-state saltation conditions and by neglecting the pressure gradient. According to Newton's third law, the aerodynamic force applied to a
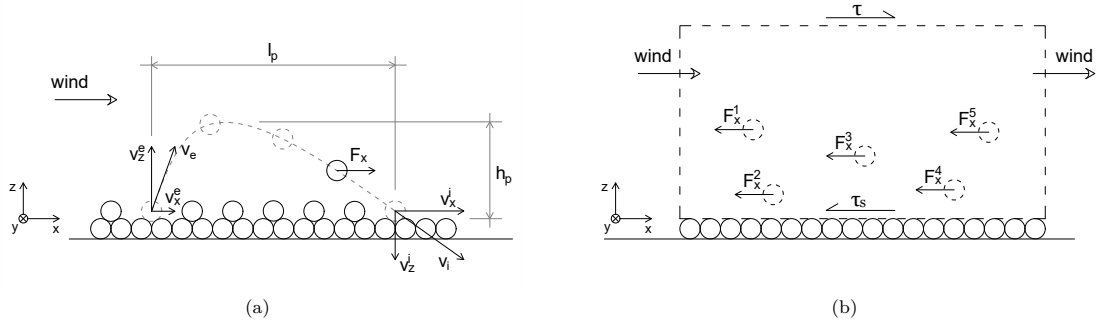
Figure 2.1: (a) Schematic of a particle hop: representation of the particle hop height and length, the instantaneous aerodynamic force in the streamwise direction applied to a particle, $F_x$ [N], and the particle ejection and impact velocities, $v_e$ [m s$^{-1}$] and $v_i$ [m s$^{-1}$] (please note that the ejection and impact velocities often have a crosswise component which is not represented in the figure). (b) Forces and stresses applied to the fluid flow in the streamwise direction in a given control volume spanning from the surface to a height above the saltation layer (only five particles are illustrated as an example).

particle is equal in magnitude and opposite to the force applied to the fluid. Therefore, the sum of aerodynamic forces in the streamwise direction applied to all particles in saltation per unit surface area equals the difference in shear stresses, $\tau - \tau_s$ (Figure 2.1b). From these considerations and assuming that the variety of particle hops can be approximated by an average trajectory (characteristic path) (e.g., Bagnold, 1941; Durán et al., 2011; Kok et al., 2012; Ungar & Haff, 1987), the following expression for the transport rate is obtained:

$$Q = (\tau - \tau_s) \frac{\langle v_p \rangle \langle t_p \rangle}{\langle \Delta v_{x,s} \rangle} = (\tau - \tau_s) \frac{\langle l_p \rangle}{\langle \Delta v_{x,s} \rangle} \tag{2.1}$$

where $v_p$ [m s$^{-1}$] is the hop-averaged particle streamwise velocity, $\Delta v_{x,s} = v_x^i - v_x^e$ [m s$^{-1}$] is the difference between the impact and ejection streamwise velocities, and $l_p = v_p t_p$ [m] is the particle hop length in the streamwise direction (henceforth hop length). The angle brackets, $\langle \rangle$, represent averages over the ensemble of particles in saltation. Therefore, $\langle v_p \rangle$ denotes the average particle streamwise velocity.

When deducing equation 2.1, other forces along the streamwise direction, such as the electrostatic forces and those from interparticle collision, were neglected. These forces are expected to be smaller than the particle weight and the aerodynamic forces and are generally neglected in the modeling of saltation in air (Anderson & Hallet, 1986; Maxey & Riley, 1983).Their effects on sand and snow saltation were studied by several authors (e.g., Durán et al., 2011; Huang et al., 2007; Kok & Renno, 2006, 2008; D. S. Schmidt et al., 1998; Yu et al., 2022), but further investigation is needed to fully assess their impact on the particle trajectory (Kok et al., 2012). Moreover, the use of average quantities to describe the various particle trajectories introduces an error in the calculation of the transport rate, which is not sufficiently discussed in the literature (e.g., Shao & Mikami, 2005). Nevertheless, equation 2.1 is the basis for several simple

parameterizations (e.g., Bagnold, 1941; Kok et al., 2012; Pomeroy & Gray, 1990; Sørensen, 1991; Ungar & Haff, 1987) and is expected to yield a reasonable approximation for the scaling of $Q$ with $u_*$. The variety of parameterizations proposed for $Q$ arise from different expressions for $\tau_s$, $\langle \Delta v_{x,s} \rangle$ and $\langle l_p \rangle$. These quantities are discussed in the next sub-sections.

### 2.2.1   The surface shear stress

The onset of saltation occurs when the surface shear stress grows above a given threshold, which allows the aerodynamic entrainment of surface particles to take place (Bagnold, 1941). This threshold shear stress is named the fluid threshold, $\tau_{ft}$ [Pa]. By definition, $\tau_{ft} = \rho_a u_{*,ft}^2$, where $u_{*,ft}$ [m s$^{-1}$] is the fluid threshold friction velocity. According to Owen (1964), during steady-state saltation, the particles are continuously set in motion by aerodynamic entrainment and the particle bombardment at the surface is only responsible for dislodging or loosening the grains. Naturally, he claims that saltation can only be sustained if $\tau_s$ is equal or greater than a minimum value that allows the entrainment of loose grains, previously dislodged by impacting particles. Owen (1964) goes one step further and hypothesizes that the surface shear stress stays at this minimum value at which saltation is sustained and is, therefore, invariant with respect to $u_*$ (Owen's hypothesis): if $\tau_s$ is lower than this threshold, no aerodynamic entrainment of previously dislodged particles occurs; and if it is larger than that threshold more particles are entrained which ultimately restores $\tau_s$ to its original value. According to Owen, the minimum surface shear stress required to sustain saltation is equal to the impact threshold, $\tau_{it} = \rho_a u_{*,it}^2$ [Pa]: the lower fluid shear stress outside the saltation layer for which saltating particles maintain a steady-state motion (Bagnold, 1941). $u_{*,it}$ [m s$^{-1}$] is named the impact threshold friction velocity. Due to the contribution of the impacting particles to dislodging the grains, Owen (1964) expects the impact threshold to be smaller than the fluid threshold. Indeed, Bagnold (1941) showed with wind tunnel experiments developed with sand that the shear stress needed to keep saltating particles in motion is smaller than that required to initiate saltation from rest.

The experimental assessment of Owen's hypothesis is challenging because it implies high frequency measurements of the wind velocity close to the surface within a saltation layer (e.g., B. Li & McKenna Neuman, 2012). The measurements of Walter et al. (2014) revealed a non-monotonic evolution of $\tau_s$ with $u_*$. As the friction velocity was continuously raised above the fluid threshold friction velocity, the measured $\tau_s$ firstly reduced and then increased. In general, a relatively small variation of $\tau_s$ with $u_*$ and a relatively large standard deviation of the measurements were obtained. In addition, some numerical models that include a statistical description of rebound and splash obtained a significant variation of the surface shear stress with respect to $u_*$ (Kok & Renno, 2009; Nemoto & Nishimura, 2004; Werner, 1990), while other predicted a negligible change (Niiya & Nishimura, 2017). Doorschot and Lehning (2002), who modeled steady-state saltation with a simplified numerical model, have also obtained a slight variation of $\tau_s$ with the rise of $u_*$. From the different trends obtained by measurements and models, it is clear that the self-regulatory behaviour of steady-state saltation is not necessarily

characterized by a constant surface shear stress, invariant with respect to $u_*$, but that different equilibrium states can emerge depending on the wind and particle characteristics. In this way, Owen's hypothesis is expected to oversimplify the saltation dynamics (Kok et al., 2012). Nonetheless, the assumption that $\tau_s$ does not vary with $u_*$, but depends solely on the bed characteristics, is regarded as an acceptable first order approximation (Niiya & Nishimura, 2022; Walter et al., 2014). Therefore, it might be appropriate for simple models and parameter-izations, even if aerodynamic entrainment is not considered the main entrainment process (e.g., Pomeroy & Gray, 1990; Sørensen, 1991, 2004). Regarding the effect of the snow cover characteristics on the value of $\tau_s$, very little is know. When modeling sand saltation, Kok and Renno (2009) obtained an increase of $\tau_s$ with the increase of the particle diameter (see Figure 13 in Kok et al., 2012), but no similar studies featuring snow saltation are available.

In the blowing snow schemes of the atmospheric models RACMO, MAR, Meso-NH and CRY-OWRF (Amory et al., 2021; Lenaerts et al., 2012; Sharma et al., 2023; Vionnet et al., 2014), $\tau_s$ is assumed invariant with respect to $u_*$ and approximated by the fluid threshold, $\tau_{ft}$. The assumption that $\tau_s = \tau_{ft}$ is partly based on the model proposed by Owen (1964). However, it neglects the effect of particle impacts in dislodging the grains that justifies Owen's claim that $\tau_s$ must be smaller than $\tau_{ft}$. The assumption that $\tau_s = \tau_{ft}$ also implies that the fluid shear stresses for saltation initiation and cessation are equal, which is a useful assumption (note that equation 2.1 reduces to zero when $\tau$ equals $\tau_s$). However, it is not in agreement with saltation models developed for sand (e.g., Kok et al., 2012). For the case of snow saltation, the relationship between $\tau_s$ and $\tau_{ft}$ is still not clear. For instance, while the numerical model of Nemoto and Nishimura (2004) predicts $\tau_s > \tau_{ft}$, the one from Niiya and Nishimura (2017) predicts $\tau_s < \tau_{ft}$. Both trends are found with the model of Doorschot and Lehning (2002) depending on the characteristics of the snow cover. In this way, further investigation is needed to better assess the value of $\tau_s$ during snow saltation and the impact of the currently used assumption on the accuracy of the transport rate.

### 2.2.2 The ejection and impact velocities

When assessing the transport rate, Bagnold (1941) assumed that the ratio $\langle l_p \rangle / \langle \Delta v_{x,s} \rangle$ scales with $\langle v_z^e \rangle / g$, where $v_z^e$ [m s$^{-1}$] is the vertical component of the ejection velocity and $g$ [m s$^{-2}$] is the acceleration of gravity. One arrives to this result by solving the ballistic motion of a particle in saltation subjected to some simplifying assumptions (see for instance, Sørensen, 1991). In addition, Bagnold (1941) assumed that $\langle v_z^e \rangle$ is proportional to $u_*$, based on the idea that the particle velocity at impact must scale with $u_*$ (please note that $u_*$ is the friction velocity outside the saltation layer and not the surface friction velocity, which is defined by $u_{*,s}$).

Numerical models, like the one proposed by Ungar and Haff (1987), generally suggest that $\langle \Delta v_{x,s} \rangle$ is invariant with respect to $u_*$. Ungar and Haff (1987) arrived to this result by assuming that in steady-state saltation each particle impacting the surface is replaced by a new one, equal in size, splashed from the surface upon impact. Indeed, during steady-state saltation,

zero net erosion and deposition of particles implies an equality between the mass flow rate of particles that fail to rebound and the mass flow rate of particles that successfully enter saltation via splash or aerodynamic entrainment (Kok et al., 2012). Contrary to Owen (1964), most numerical models assume that the surface processes of rebound and splash play an important role in steady-state saltation (e.g., Durán et al., 2011; Kok & Renno, 2009). These models compute the probability of rebound and the number and initial velocity of splashed grains as a function of the bed characteristics and the impacting particle mass and velocity. As a result, they predict that $\langle \Delta v_{x,s} \rangle$ does not vary with $u_*$. This assumption is present in the analytic model of Sørensen (2004), which is used in Meso-NH (Vionnet et al., 2014) and CRYOWRF (Sharma et al., 2023) to compute the transport rate. In addition, the snow saltation model of Niiya and Nishimura (2022) which represents the surface processes of aerodynamic entrainment, rebound and splash has also revealed ejection and impact velocities that are mainly invariant with respect to $u_*$.

Field and wind tunnel measurements conducted with sand show a negligible influence of $u_*$ on the near-surface particle velocity. For instance, Namikas (2003) found a better agreement between model results and field measurements of particle mass flux when assuming an averaged ejection velocity invariant with respect to $u_*$ for friction velocities ranging from 0.27 to 0.63 m s$^{-1}$. Moreover, wind tunnel experiments developed by Creyssels et al. (2009) and Ho et al. (2011) over an erodible sand surface show a negligible variation of the particle streamwise velocity close to the surface with respect to $u_*$, considering friction velocities ranging from 0.24 to 0.67 m s$^{-1}$ and from 0.42 to 1 m s$^{-1}$, respectively. During the experiments, the particles were illuminated by a laser sheet and recorded with a high-speed camera. The particle velocities were calculated with the Particle Tracking Velocimetry (PTV) technique and the particle streamwise velocity close to the surface was extrapolated from a linear regression of the average streamwise velocity profiles in the first 5 and 3 cm above the surface, respectively. The particle streamwise velocity close to the surface is named slip velocity and represents the average between the ejection and impact streamwise velocities.

The streamwise velocity of saltating snow was investigated by Aksamit and Pomeroy (2016) during field experiments in Alberta, Canada, using a similar experimental setup as the one used by Creyssels et al. (2009) and Ho et al. (2011). The streamwise velocity of ascending particles in the first 2.5 cm above the surface was reported for friction velocities ranging from 0.21 to 0.54 m s$^{-1}$ for three different snow conditions (old snow, fresh snow, and fine decomposing grains). The average particle ejection velocity in the streamwise direction, $\langle v_x^e \rangle$, was extrapolated from a linear regression of the average streamwise velocity of ascending particles along the first 1 cm above the surface. Even though steady-state conditions were not attained during the experiments, different trends were obtained for different snow surface characteristics. For the old and fresh snow covers, the streamwise ejection velocity was not found to vary monotonically with the friction velocity, while for the one composed of fine decomposing grains, a slight increase with $u_*$ was observed. Among the three snow surfaces, the latter was characterized by the highest hand hardness index. The increase of the streamwise ejection velocity with $u_*$, obtained over the surface of fine decomposing grains,

is in agreement with the increase of the particle slip velocity as $u_*$ increases, obtained by Ho et al. (2011) after performing wind tunnel measurements of saltating sand over a rigid (non-erodible) surface, considering friction velocities ranging from 0.3 to 0.45 m s$^{-1}$. Aksamit and Pomeroy (2016) obtained higher values of $\langle v_x^e \rangle$ over the fresh snow cover than over the fine decomposing grains and old snow covers. Differently, Ho et al. (2011) obtained higher values for the particle slip velocity over the rigid surface in comparison to the erodible surface. The effect of interparticle cohesion on the ejection velocity of saltating particles was also investigated by Comola, Gaume, et al. (2019) using the Discrete Element Method (DEM) and a simple description of the wind velocity field. In their model, an increase in cohesion is represented by an increase in the maximum shear and tensile forces that an interparticle bond can sustain before failure. In agreement with the findings of Ho et al. (2011), an increase in interparticle cohesion resulted in a slight increase in the particle rebound velocity and a significant increase of the ejection velocity of splashed particles.

In summary, most of the available literature suggests that the average ejection and impact velocities are invariant with respect to $u_*$. However, the few experiments and numerical simulations of snow saltation revealed different trends depending on the snow surface characteristics. In order to understand the particular case of snow saltation, more experimental measurements developed with snow are required, which must include a detailed characterization of the snow cover, the wind field and the kinematics of the particles in saltation.

### 2.2.3   The hop length

The particle hop length, $l_p$, is equal to the duration of the particle hop, $t_p$, times the hop-averaged particle streamwise velocity, $v_p$. If we approximate the variety of particle trajectories by a characteristic path, the average hop length, $\langle l_p \rangle$, can be estimated from the product $\langle v_p \rangle \langle t_p \rangle$. $\langle t_p \rangle$ is expected to deviate from the theoretical value of $2\langle v_z^e \rangle / g$ (obtained when neglecting the aerodynamic forces in the particle motion), but it is nonetheless expected to scale with $\langle v_z^e \rangle$ (Sørensen, 1991). In addition, as discussed in the previous section, the particle ejection velocity during steady-state saltation is generally regarded as invariant with respect to $u_*$. Under these conditions, the scaling of $\langle l_p \rangle$ with $u_*$ is mainly dependent on the scaling of $\langle v_p \rangle$ with $u_*$. Assuming that the particle ejection velocity does not vary with $u_*$, the average particle streamwise velocity, $\langle v_p \rangle$, depends solely on the aerodynamic forces applied on the particles during their trajectories and, therefore, on the wind velocity inside the saltation layer.

Ungar and Haff (1987) concluded that $\langle l_p \rangle$ is invariant with respect to $u_*$ and proportional to the particle diameter, $d$ [m]. This result is obtained by assuming that the ejection and impact velocities scale with $(dg)^{\frac{1}{2}}$ and that the wind velocity in the saltation layer is invariant with respect to $u_*$. Differently, the analytic model of Sørensen (2004), used in Meso-NH (Vionnet et al., 2014) and CRYOWRF (Sharma et al., 2023), arrived to an average particle hop length that increases with $u_*$. In the model, the particle ejection velocity is also assumed invariant with respect to $u_*$ and the logarithmic (particle free) wind profile is modified to take into account

the reduction in fluid shear stress induced by the particles in saltation. As a result, the wind velocity inside the saltation layer decreases in comparison to the logarithmic profile, but it increases nonetheless with $u_*$.

Wind tunnel measurements show that the wind velocity during saltation is expected to be invariant with respect to $u_*$ in the first 1 cm above the surface, where most saltating particles are (Bagnold, 1941; B. Li & McKenna Neuman, 2012). However, at higher elevations, the wind velocity is expected to scale with $u_*$ (e.g., Aksamit & Pomeroy, 2016; Nishimura et al., 2014). Therefore, if a significant number of particles travel above 1 cm height during a significant extent of their trajectories, $\langle v_p \rangle$ might increase as $u_*$ increases. This is in agreement with the field experiments of Namikas (2003) developed with sand, which revealed a slight increase of the average hop length with $u_*$.

The numerical model of Durán et al. (2011) suggests that the scaling of the hop length with the friction velocity differs according to the saltation regime. At a low-velocity regime (for, approximately, $u_*/u_{*,it} < 4$), most saltating particles are within this first centimeter above the surface where the wind velocity is invariant with respect to $u_*$. Therefore, the average particle velocity and hop length are expected to be invariant with respect to $u_*$. However, at a high-velocity regime ($u_*/u_{*,it} > 4$), a considerable number of saltating particles reach higher elevations above the surface, where the wind velocity increases with $u_*$. Under these conditions, both the average particle streamwise velocity and hop length are expected to increase linearly with $u_*$. Taking into account that $u_*/u_{*,it} > 4$ rarely occurs in nature for the case of saltating sand, Kok et al. (2012) argued that neglecting the effect of $u_*$ on the hop length can be regarded as a reasonable approximation. If both $\langle \Delta v_{x,s} \rangle$ and $\langle l_p \rangle$ are assumed invariant with respect to $u_*$, the transport rate scales with $u_*^2$ (note that $\tau = \rho u_*^2$) (Durán et al., 2011; Ungar & Haff, 1987). Conversely, if $\langle l_p \rangle$ increases linearly with $u_*$, one arrives to $Q \propto u_*^3$ (Sørensen, 1991, 2004).

Further studies are needed in order to fully understand the scaling of $\langle l_p \rangle$ with the friction velocity during snow saltation. In particular, it would be interesting to unveil if the two regimes proposed by Durán et al. (2011) are also representative of saltating snow. The full vertical profile of the particle streamwise velocity is discussed in section 2.3.2.

### 2.2.4   The average particle streamwise acceleration

The hop-averaged particle streamwise acceleration, $a_p$ [m s$^{-2}$], is given by the ratio $\Delta v_{x,s}/t_p$. When assuming a characteristic particle hop for all particles in saltation, the average particle streamwise acceleration, $\langle a_p \rangle$, is approximated by $\langle \Delta v_{x,s} \rangle / \langle t_p \rangle$. In this way, the transport rate in equation 2.1 can be expressed by

$$Q = (\tau - \tau_s) \frac{\langle v_p \rangle}{\langle a_p \rangle}. \tag{2.2}$$

According to the balance of linear momentum applied to the particles in saltation described in section 2.2, the ratio between the total aerodynamic force along the streamwise direction applied to all particles in saltation and their weight is given by $\langle a_p \rangle / g$. Bagnold (1973) argued that this ratio between the applied horizontal force and the weight of the mass in motion represents a mean friction coefficient. This friction coefficient is expect to be of a similar nature as the coefficient of static friction obtained between two solid surfaces in contact. Taking into account that the real (microscopic) contact between two surfaces is actually discontinuous, Bagnold (1973) claims that this analogy holds for the case of saltating particles, in which the contact between the particles and the surface is intermittent. Therefore, similar to a coefficient of static friction, the ratio $\langle a_p \rangle / g$ is expected to be a function of the particle-bed interaction only and, consequently, invariant with respect to $u_*$.

In the saltation model proposed by Pomeroy and Gray (1990), an expression for the transport rate of saltating snow is also obtained by estimating the ratio $\langle a_p \rangle / g$. However, differently from Bagnold (1973), $\langle a_p \rangle$ was found to increase linearly with $u_*$. In addition, it was found to be highly variable with the snow surface characteristics. In the model, $\langle a_p \rangle$ was not estimated from the direct measurements of $\langle \Delta v_{x,s} \rangle$ and $\langle t_p \rangle$, but it was deduced from fitting experimental measurements of the particle mass flux in saltation with equation 2.2. Therefore, the resultant scaling of $\langle a_p \rangle$ with $u_*$ is a function of the parameterizations considered for $\tau_s$ and $\langle v_p \rangle$, as well as of the accuracy of the mass flux measurements and the respective vertically integrated value, $Q$.

The mass flux measurements considered in the model were performed at Saskatoon, Canada, using an optoelectronic snow particle detector placed at approximately 2 cm height above the snow surface. This device counts the number of particles crossing an infrared laser beam. The mass flux is then estimated by assuming a particle size distribution given by a 2-parameter Gamma distribution, as suggested by R. Schmidt (1981), and a particle density equal to the density of ice ($\approx 917 \, \mathrm{kg \, m^{-3}}$). The mass flux in saltation is assumed to be uniform in height. Therefore, the transport rate is estimated from the product of the measured mass flux and the height of the saltation layer, $h_{salt}$ [m]. As addressed in section 2.3.3, the vertical profile of the particle mass flux exhibits strong gradients close to the surface. In this way, the saltation mass flux is hardly defined by a single point measurement and the assumption of a constant mass flux along the saltation layer might lead to errors in the assessment of the transport rate.

In summary, Pomeroy and Gray (1990) arrived to the conclusion that $\langle a_p \rangle$ scales with $u_*$ by assuming that the mass flux is uniform in height, that $h_{salt}$ scales with $u_*^2$ (Owen, 1964) and that $\langle v_p \rangle$ is invariant with respect to $u_*$. As a consequence, they concluded that $Q$ scales linearly with $u_*$, which is not in agreement with most saltation models (e.g., Bagnold, 1941; Durán et al., 2011; Sørensen, 1991, 2004). Notwithstanding, this model is still widely used, specifically in the blowing snow schemes of RACMO (van Wessem et al., 2018) and MAR (Amory et al., 2021).

If both $\langle \Delta v_{x,s} \rangle$ and $\langle t_p \rangle$ are invariant with respect to $u_*$, as suggested by several models and

measurements (see sections 2.2.2 and 2.2.3), $\langle a_p \rangle$ is mainly expected to be invariant with respect to $u_*$, as early hypothesized by Bagnold (1973). Taking into account the challenges of the direct calculation of $\langle a_p \rangle$ from velocity measurements for different values of $u_*$ (e.g., Araoka & Maeno, 1981, and Appendix A), the variation of $Q$ with $u_*$ and the snow surface characteristics might be better understood from the direct study of $\langle \Delta v_{x,s} \rangle$, $\langle t_p \rangle$ and $\langle v_p \rangle$.

## 2.3 The vertical profiles of particle concentration, streamwise velocity and mass flux

The particle mass flux in saltation, $q$ [kg m$^{-2}$ s$^{-1}$], corresponds to the flow rate of particles moving in saltation per unit cross-section area. The particle concentration, $c$ [kg m$^{-3}$], is the mass of particles in saltation per unit volume. By definition, these two quantities are related by $q = c\bar{v}_x$, where $\bar{v}_x$ [m s$^{-1}$] is the volume-averaged particle streamwise velocity (henceforth particle streamwise velocity) at which the respective mass of particles in saltation travels across a given cross-section area (note that the average of $\bar{v}_x$ along the saltation layer equals the average particle streamwise velocity, $\langle v_p \rangle$, defined in section 2.2). During steady-state saltation, $q$, $c$ and $\bar{v}_x$ are invariant along the horizontal directions, but they are expected to vary with the height above the surface. In the following sub-sections, we discuss the parameterizations used to model these quantities, as well as the experimental, theoretical and numerical results that contributed to their development.

### 2.3.1 The particle concentration

An analytic expression for the vertical profile of particle concentration was derived by Kawamura (1951). In the model, the saltation dynamics is simplified by neglecting the aerodynamic forces on the vertical motion of saltating particles, by assuming that the probability distribution of the vertical component of the particle ejection velocity follows a half-normal distribution and that the saltating particles are uniformly sized. In this way, from a mass balance between the surface and a given height $z$, the particle concentration at each height can be estimated as a function of the probability distribution of the vertical ejection velocity and the vertical mass flux of particles leaving the surface. In Gordon et al. (2009), it is shown that the analytic expression of Kawamura (1951) is well approximated by an exponential decay of the form:

$$c(z) = c_o \exp\left(-\frac{z}{\delta_c}\right) \tag{2.3}$$

where $c_o$ [kg m$^{-3}$] is the particle concentration at the surface (by extrapolating the exponential profile down to the surface) and $\delta_c$ [m] is the decay height of the particle concentration profile. The decay height, $\delta_c$, defines the height above the surface for which the particle concentration

is reduced to $c_o/\exp(1)$. The theoretical expression proposed by Kawamura (1951) tends to infinity at the surface. In contrast, equation 2.3 is expected to underestimate the particle concentration near the surface and to provide a good approximation only for $z > \langle h_p \rangle$, where $\langle h_p \rangle$ [m] is the average hop height of particles in saltation.

The direct measurement of the particle concentration is challenging because it requires the measurement of the number and size of saltating particles in a well defined volume (Creyssels et al., 2009). Gordon et al. (2009) measured the number density of snow particles in saltation in the first 9 cm above the surface over sea ice in Franklin Bay, Canada. Images of saltating snow were recorded with a camera, which captured the light reflected by snow particles traveling in front of a black background. The vertical profile of particle concentration was estimated by specifying the width over which the particles were detected (volume depth), by assuming that the particle size distribution is given by a 2-parameter Gamma distribution and that the saltating particles have the density of ice. The resultant particle concentration profiles, obtained for friction velocities ranging from 0.25 to 0.5 m s$^{-1}$ and different snow surface conditions, followed mainly an exponential decay as predicted by the theoretical model of Kawamura (1951). However, when the particle concentration was low, the data was more scattered and deviations from the exponential decay was seen above approximately 2 cm height above the surface.

From fitting the measured vertical profiles with equation 2.3, the respective decay height was estimated. According to Gordon et al. (2009), $\delta_c$ is expected to scale with the average hop height, $\langle h_p \rangle$. In the absence of aerodynamic forces, the hop height of a particle in saltation scales with $v_z^{e2}/g$. Therefore, $\delta_c$ is expected to scale with $\langle v_z^e \rangle^2/g$. Owen (1964) suggested that $\langle v_z^e \rangle$ scales with $u_*$ and, therefore, that $\langle h_p \rangle$ scales with $u_*^2$. However, the measurements of Gordon et al. (2009) revealed a weak correlation between $\delta_c$ and $u_*$. Indeed, for each set of measurements conducted on the same day (similar snow surface conditions), the decay height did not increase monotonically with the friction velocity.

Similar results were found by Creyssels et al. (2009), after performing wind tunnel experiments with uniformly-sized sand particles. As mentioned in section 2.2.2, the experiments were performed with a high-speed camera illuminated by a laser sheet. The particle concentration was computed in the first 5 cm above the surface for friction velocities ranging from 0.24 to 0.67 m s$^{-1}$. In the calculations, the volume depth was assumed equal to the width of the laser. The vertical profiles of particle concentration were found to follow an exponential decay of the form of equation 2.3 and the respective decay height was found to be invariant with respect to the friction velocity. The conclusions of Gordon et al. (2009) and Creyssels et al. (2009) regarding the scaling of $\delta_c$ with $u_*$ are in agreement with the assumption that the ejection velocity is invariant with respect to $u_*$, which is in line with most numerical models and experimental measurements developed over erodible surfaces (see section 2.2.2).

Ho et al. (2011) used a similar technique to measure the particle concentration in the first 6 cm above the surface in a wind tunnel. In their experiments, both a bed composed of loose

sand grains and a rigid (non-erodible) surface were used. In agreement with the experiments of Creyssels et al. (2009), the particle concentration over the erodible surface was found to decrease with increasing height following an exponential decay and the computed decay height was invariant with respect to $u_*$. Differently, when saltation was allowed to develop over the rigid surface, the decay height was found to be higher and to increase linearly with $u_*$. This result is related to the higher values of the particle slip velocity obtained over the rigid surface in comparison with the erodible one and to the increase of the particle slip velocity with the increase of $u_*$ obtained over the rigid surface, mentioned in section 2.2.2.

Taking into account the challenges and uncertainties of the particle concentration measurements, especially in the field, measurements of the particle mass flux are more frequent (e.g., Martin & Kok, 2017; Namikas, 2003; Nishimura & Nemoto, 2005). Therefore, the general approach in blowing snow schemes is to derive the particle concentration as a function of the particle streamwise velocity and mass flux (Amory et al., 2021; Sharma et al., 2023; van Wessem et al., 2018; Vionnet et al., 2014). These two quantities are discussed in the next sections.

### 2.3.2   The particle streamwise velocity

The particle streamwise velocity of saltating sand was measured by Creyssels et al. (2009) and Ho et al. (2011) in the first 5 and 3 cm above the surface, respectively (see details in section 2.2.2). In this region of the saltation layer, the particle streamwise velocity, $\bar{v}_x$, was found to increase linearly with height. Over a bed of loose sand grains, the effect of the friction velocity on the particle slip velocity was almost negligible, as discussed in section 2.2.2. Above the surface, $\bar{v}_x$ was found to increase slightly with the rise of $u_*$. Using also the PTV technique, Aksamit and Pomeroy (2016) measured the velocity of saltating snow in the first 2.5 cm above the surface in a snow-covered area. A linear increase of $\bar{v}_x$ with height was seen in the first 1 cm above the surface. In addition, $\bar{v}_x$ was found to increase slightly with the friction velocity.

The particle streamwise velocity can also be measured with a Snow Particle Counter (SPC) (Nishimura et al., 2014). The SPC is an optical device that detects the particles that cross a 25 mm long, 2 mm high and 0.5 mm wide laser beam. In general, this device is used to retrieve the number and average diameter of all particles crossing the laser beam during a defined time period. Therefore, it is mainly used to estimate the particle mass flux. The particle streamwise velocity can be computed by evaluating the time that each particle takes to cross the laser beam. Nishimura et al. (2014) measured the streamwise velocity of saltating snow along the first 10 cm above the surface in a wind tunnel for friction velocities ranging from 0.37 to 0.63 m s$^{-1}$ using this technique. In agreement with the previous studies, the particle streamwise velocity was found to increase as the height above the surface and the friction velocity increase. However, differently from the previous PTV measurements, most of the measurement points were located above 5 cm height. In this way, the increase of $\bar{v}_x$ with increasing height did not follow a linear trend, but rather a logarithmic one. Similar particle streamwise velocity profiles were found in the wind tunnel measurements performed

by Nishimura and Hunt (2000), who recorded saltating snow particles and ice spheres in the first 10 cm above the surface with a video system, and by Rasmussen and Sørensen (2008), who used Laser Doppler Velocimetry (LDV) to measure the streamwise velocity of saltating sand in the first 8 cm above the surface.

Numerical models that represent the surface processes of splash and rebound have also obtained an increase of the particle streamwise velocity with height (e.g., Durán et al., 2011; Kok & Renno, 2009). As expected, in the first 1 cm above the surface, the particle velocity is mainly invariant with respect to $u_*$ and, at higher elevations, the particle streamwise velocity increases with the increase of $u_*$.

In the model of Pomeroy and Gray (1990), the particle streamwise velocity is assumed constant in height and characterized by its average value $\langle v_p \rangle$. $\langle v_p \rangle$ is assumed invariant with respect to $u_*$ and proportional to the impact threshold friction velocity, $u_{*,it}$. This assumption can be found in the blowing snow schemes of RACMO, MAR, Meso-NH and CRYOWRF to compute the particle concentration at the top of the saltation layer as a function of the particle streamwise velocity and mass flux (Amory et al., 2021; Lenaerts et al., 2012; Sharma et al., 2023; Vionnet et al., 2014). The assumption that $\langle v_p \rangle$ scales with $u_{*,it}$ is justified by the observations of Bagnold (1941) regarding the existence of a focus point in the wind velocity profile. According to his observations, during steady-state saltation, the wind velocity inside the saltation layer obtained for different values of $u_*$ converge to the same value at a given height close to the surface - the focus point. The wind velocity at the focus point scales with the impact threshold friction velocity and is, therefore, solely dependent on the bed characteristics. In this way, the particle streamwise velocity in the vicinity of the focus point is also expected to scale with $u_{*,it}$, which according to Owen (1964) is the value of the surface friction velocity during saltation (see section 2.2.1). The existence of a focus point and the fact that the particle streamwise velocity close to the surface is invariant with respect to $u_*$ are known features of the saltation system, obtained by different models that represent the surface processes of rebound and splash (e.g., Durán et al., 2011; Kok & Renno, 2009). However, as previously discussed, experimental measurements performed with both sand and snow show that the particle streamwise velocity above approximately 3 cm height increases with the increase of $u_*$. In this way, the parameterization used for $\bar{v}_x$, in particular, its scaling with $u_{*,it}$ and $u_*$, must be defined according to the height at which the particle streamwise velocity (and, subsequently, the particle concentration) is being computed.

The snow surface characteristics are also expected to influence the particle streamwise velocity, as previously discussed in section 2.2.2. For instance, for the same range of friction velocities, Aksamit and Pomeroy (2016) found a higher particle streamwise velocity in the first 2.5 cm above the surface when saltation developed over a surface of fresh snow than over surfaces of old snow or fine decomposing grains. One can hypothesize that this is related to the smaller density and dendritic shape of the particles in saltation. The particles ejected from a fresh snow surface are not fully rounded and will continuously fragment and get denser as the particles collide with the bed (Comola et al., 2017).

### 2.3.3   The particle mass flux

The vertical profile of particle mass flux is expected to follow an exponential decay of the same form of equation 2.3 (e.g., Martin & Kok, 2017; Nalpanis et al., 1993; Namikas, 2003):

$$q(z) = q_o \exp\left(-\frac{z}{\delta_q}\right) \tag{2.4}$$

where $q_o$ [kg m$^{-2}$ s$^{-1}$] is the surface mass flux (by extrapolating the exponential profile down to the surface) and $\delta_q$ [m] is the decay height of the particle mass flux profile. By definition, the integral of $q$ along the height yields the transport rate, $Q$. Therefore, it follows that $q_o = Q/\delta_q$.

Experiments developed with sand show that the mass flux profile follows an exponential decay at moderate friction velocities, but does not at low values of $u_*$, close to the fluid threshold friction velocity (Nalpanis et al., 1993; Namikas, 2003). In addition, it was shown that the exponential decay tends to underestimate the mass flux in the first 2 cm above the surface (Bauer & Davidson-Arnott, 2014; Namikas, 2003). This might pose a problem when relating the fitted values of $q_o$ and $\delta_q$ with the transport rate, $Q$. Experiments developed with snow, both in wind tunnels (Sato et al., 2001; Sugiura et al., 1998) and in the field (Nishimura & Nemoto, 2005; Takeuchi, 1980), revealed an exponential decay of the mass flux profile in approximately the first 10 cm above the surface. Near the top of the saltation layer, deviations are seen due to the saltation-suspension transition (Gordon et al., 2009). The exponential decay of the particle mass flux with height contrasts with the uniform profile assumed in the model of Pomeroy and Gray (1990), as discussed in section 2.2.4.

Similarly to the decay height presented in equation 2.3, $\delta_q$ is also thought to scale with the average particle hop height in saltation and, therefore, with $\langle v_z^e \rangle^2/g$ (Nishimura & Hunt, 2000). Based on the assumption made by Owen (1964) regarding the scaling of $\langle v_z^e \rangle$ with $u_*$, Nishimura and Hunt (2000) assumed that $\delta_q$ must scale with $u_*^2/g$. This parameterization for $\delta_q$ is currently used in Meso-NH (Vionnet et al., 2014) and CRYOWRF (Sharma et al., 2023) to compute the particle mass flux in saltation.

The decay height is estimated from fitting equation 2.4 to the measured mass flux profiles. In Figure 2.2, the values of $\delta_q$ obtained from different experiments developed with sand and snow are presented as a function of the friction velocity, $u_*$ (Martin & Kok, 2017; Namikas, 2003; Nishimura & Nemoto, 2005; Sugiura et al., 1998). The expression proposed by Nishimura and Hunt (2000) is also presented for comparison. The measurements of Sugiura et al. (1998) were performed in a wind tunnel using preserved natural snow, which was disintegrated into individual particles prior to the experiments. The particle mass flux was measured between 1.6 and 6.1 cm above the surface using a SPC. By detecting the number and average diameter of saltating particles, the mass flux is computed by approximating the snow particles to spheres and by assuming a given particle density (generally, 917 kg m$^{-3}$). As seen in Figure 2.2, the
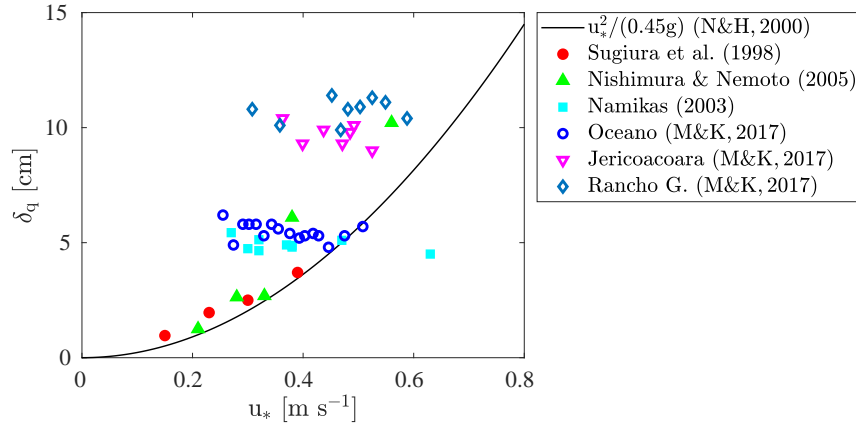
Figure 2.2: Decay height, $\delta_q$, as a function of the friction velocity, $u_*$. Results reported by Sugiura et al. (1998) after wind tunnel experiments conducted with snow and by Namikas (2003) and Martin and Kok (2017) (M&K, 2017) after field experiments conducted with sand. The values of $\delta_q$ referring to the field measurements of Nishimura and Nemoto (2005) conducted with snow were not reported in their work. We have estimated them by fitting the mass flux measurements between 2 and 12 cm height above the surface with equation 2.4. The expression proposed by Nishimura and Hunt (2000) (N&H, 2000) is also drawn for comparison.

values of $\delta_q$ obtained for friction velocities ranging from 0.15 to 0.39 m s$^{-1}$ were found to increase with $u_*^2$, as suggested by Nishimura and Hunt (2000).

The results of Sugiura et al. (1998) are in agreement with the wind tunnel experiments of Sato et al. (2001) performed with two different snow covers. Similarly to the experiments of Sugiura et al. (1998), snow particles were obtained by disintegrating a layer of preserved natural snow. Experiments were performed immediately after spreading the snow particles over the wind tunnel floor (loose snow cover) and after some time, which allowed sintering to take place (hard snow cover). The vertical profile of particle mass flux followed an exponential decay over both snow surfaces and the decay height was found to increase with the wind velocity. However, significantly different values of $\delta_q$ were obtained with each snow cover: for the same range of wind velocities, $\delta_q$ varied between, approximately, 0.9 and 3 cm over the loose snow cover and between, approximately, 3 and 8 cm, over the hard snow cover. Even though the hard snow cover cannot be considered an erodible surface (particle ejection from the surface was rare and the mass flux in saltation was highly dependent on the seeding rate of snow particles at the upwind end of the tunnel), the results of Sato et al. (2001) highlight the influence of the snow surface characteristics on the saltation dynamics and, in particular, on the decay height. The decay height obtained by Sato et al. (2001) is not presented in Figure 2.2 because the respective value of $u_*$ was not provided by the authors.

The mass flux measurements of Nishimura and Nemoto (2005) were performed in Mizuho, Antarctica, using SPCs. They reported mass flux profiles obtained for friction velocities ranging from 0.21 to 0.56 m s$^{-1}$. The respective $\delta_q$ values are not given in the article, but these can be estimated by fitting the mass flux measurements between 2 and 12 cm height to equation 2.4. From Figure 2.2, one can conclude that $\delta_q$ increases with $u_*$. In addition, considering

the three lowest friction velocities, a fair agreement is obtained between the computed values of $\delta_q$ and the expression of Nishimura and Hunt (2000). At higher friction velocities, higher values of $\delta_q$ are obtained in comparison with the quadratic expression. However, without a detailed characterization of the snow cover during the different events (which spanned a time period of 1.5 months), it is not possible to evaluate the effect of the friction velocity alone.

When performing field and wind tunnel experiments with sand, a different trend is obtained. For instance, Namikas (2003) measured the particle mass flux along the first 35 cm above the surface using wedge-shaped sediment collectors. The measurements were performed for friction velocities ranging from 0.27 to 0.63 m s$^{-1}$. From fitting the measured profiles with equation 2.4, similar values of $\delta_q$ were obtained. Therefore, it was concluded that $\delta_q$ is invariant with respect to $u_*$. The same conclusion was reached by Martin and Kok (2017) after performing field experiments in three different locations: Oceano, Rancho Guadalupe and Jericoacoara. The particle mass flux was measured with Big Spring Number Eight (BSNE) sand traps between approximately 15 to 60 cm height above the surface. Even though this height range is above the saltation layer in the case of snow saltation, the mass flux of saltating sand still follows an exponential decay in this region (Martin et al., 2018). Based on their results, Martin and Kok (2017) suggest that $\delta_q$ rather scales with the particle diameter. This would justify the agreement between the measurements of Martin and Kok (2017) at Oceano and those from Namikas (2003), which were performed at a similar location. Bigger sand grains were reported at Rancho Guadalupe and Jericoacoara in comparison to Oceano (Martin & Kok, 2017). Similarly, Nalpanis et al. (1993) could not verify the scaling of $\delta_q$ with $u_*^2$ after performing wind tunnel experiments with sand and numerical simulations.

By measuring the particle concentration and streamwise velocity, Creyssels et al. (2009) found that the mass flux evolution is mainly driven by the particle concentration profile. Therefore, even though the particle streamwise velocity was found to increase linearly with height in the first 5 cm above the surface, $\delta_c$ and $\delta_q$ were found to be approximately equal. In this way, the scaling of $\delta_c$ with $u_*$, reported in section 2.3.1, is expected to reflect the scaling of $\delta_q$ with $u_*$. In agreement with the mass flux measurements performed with sand, Creyssels et al. (2009) and Gordon et al. (2009) did not arrive to an increase of $\delta_c$ with the increase of $u_*$. In contrast, when saltation was allowed to develop over a rigid surface, Ho et al. (2011) obtained a linear increase of $\delta_c$ with $u_*$. Despite the findings of Creyssels et al. (2009) regarding the equality between $\delta_c$ and $\delta_q$, the values of $\delta_q$ presented in Figure 2.2 and the values of $\delta_c$ presented in the works of Creyssels et al. (2009), Ho et al. (2011) and Gordon et al. (2009) differ in approximately one order of magnitude. In this way, the comparison between these two quantities must be performed with care.

The scaling of $\delta_q$ with $u_*$ can also be evaluated from vertical profiles of particle number flux. Considering saltating particles of uniform size, the number flux is proportional to the mass flux and, therefore, expected to follow an exponential decay of the form of equation 2.4. Aksamit and Pomeroy (2016) computed the number flux of snow particles in saltation in the first 1 cm above the surface from the recordings of high-speed images of saltating

snow in a snow-covered area. Even though the observed particle size distribution was not uniform but characterized by a Gamma distribution, the decay height of the number flux profile is not expected to deviate significantly from $\delta_q$. Similarly to the results obtained by Gordon et al. (2009) over sea ice, a clear scaling of the decay height with $u_*$ was not found: it either increased or decreased with the rise of the friction velocity depending on the snow cover characteristics (please note that the values reported by Aksamit and Pomeroy (2016) in Figures 7d-f do not correspond to $l_\nu$ [mm], named decay length, but to $1000/l_\nu$ - N. O. Aksamit, personal communication, February 11, 2023). In addition, the values obtained are one order of magnitude lower than those reported by Sugiura et al. (1998) for the same range of friction velocities and of the same order of magnitude as those reported in Gordon et al. (2009).

The uncertainty regarding the scaling of $\delta_q$ with $u_*$ can, in part, be linked to the uncertainty regarding the scaling of $\langle v_z^e \rangle$ with $u_*$ when saltation develops over a snow surface (see section 2.2.2). The idea that $\delta_q$ is invariant with respect to $u_*$ is in agreement with the assumption that the ejection velocity is invariant with respect to $u_*$. The increase of $\delta_q$ with the rise of $u_*$ obtained by Sugiura et al. (1998) and Nishimura and Nemoto (2005) is not in agreement with this assumption and contrasts with the results of Gordon et al. (2009) and Aksamit and Pomeroy (2016) regarding the scaling of the decay height of the particle concentration and number flux profiles with respect to $u_*$. These contradictory results remain to be understood. In addition, more experimental studies are needed to understand and quantify the effect of the snow surface characteristics on $\delta_q$.

## 2.4 Conclusions

In this chapter, a review of the snow saltation parameterizations available in the literature, as well as of the theoretical, experimental and numerical arguments that support them is presented. Special attention is given to the effect of the wind velocity on the different quantities of interest. The saltation dynamics is also highly dependent on the granular bed characteristics, which is of particular importance in the study of snow saltation (Comola & Lehning, 2017). However, considerably less literature is available on this topic.

In general, the saltation models used in RACMO, MAR, Meso-NH and CRYOWRF have a poor representation of the effect of the snow surface characteristics on the different quantities of interest. The snow surface characteristics have a direct effect on the fluid threshold, which is used as an approximation for the surface shear stress. Therefore, in the currently used parameterizations, the snow morphology influences the transport rate and the average particle streamwise velocity. Nevertheless, improvements are needed to correctly take into account the effect of the snow surface characteristics on the snow saltation parameterizations. For instance, the coefficients in the expression of Sørensen (2004) used in Meso-NH and CRYOWRF to compute the transport rate are assumed constant. However, they are expected to vary with the snow surface characteristics.

By comparing the saltation models used in the blowing snow schemes of RACMO, MAR,

Meso-NH and CRYOWRF (Amory et al., 2021; Sharma et al., 2023; van Wessem et al., 2018; Vionnet et al., 2014) with the different studies on sand and snow saltation, we conclude that the parameterizations employed are not fully aligned with the current understanding of snow saltation dynamics. In the saltation model of RACMO and MAR, the particle mass flux in the saltation layer is assumed uniform in height (Pomeroy & Gray, 1990). This contrasts with the well documented exponential decay found in wind tunnel and field observations of sand and snow saltation, as well as numerical simulations. In addition, the calculation of the transport rate and of the particle concentration at the top of the saltation layer is based on the assumption that the saltation layer height is proportional to $u_*^2$ and that the average particle streamwise velocity in the saltation layer is invariant with respect to $u_*$. Even though both scaling laws can be obtained from theoretical, numerical or experimental studies, depending on the snow surface characteristics, these two assumptions are contradictory. While the first is based on the idea that the near-surface particle velocity scales with $u_*$, the latter is based on the notion that the near-surface particle velocity is invariant with respect to $u_*$. As a result, the transport rate is found to scale linearly with $u_*$, which contrasts with most saltation models available in the literature (e.g., Doorschot & Lehning, 2002; Durán et al., 2011; Sørensen, 2004). Differently, the saltation models used in Meso-NH and CRYOWRF assume that the particle mass flux profile follows an exponential decay. However, when computing the decay height of the mass flux profile and the particle concentration, which are a function of the height of the saltation layer and of the average particle streamwise velocity, they consider the same contradictory parameterizations regarding the near-surface particle velocity.

The available experimental and numerical studies show that the near-surface particle velocity is invariant with respect to $u_*$ when saltation develops over a sand covered surface. In this case, the average hop height of saltating particles, the height of the saltation layer and the decay height of the exponential mass flux and concentration profiles are found to be equally invariant with respect to $u_*$. However, when saltation develops over snow-covered surfaces, the scaling of these different quantities with $u_*$ is less clear. While early wind tunnel studies reveal that the decay height of the mass flux profile scales with $u_*^2$ (and, therefore, that the near-surface particle velocity scales with $u_*$) (Sugiura et al., 1998), recent experiments do not reveal a clear scaling of the decay height with the friction velocity and show that the scaling of the near-surface particle velocity with $u_*$ depends on the snow surface characteristics (Aksamit & Pomeroy, 2016; Gordon et al., 2009). Therefore, further investigation is needed to shed some light onto the evolution of the decay height with $u_*$ and the properties of the erodible bed.

In this chapter, we have mainly analyzed the parameterizations used to compute the transport rate and the vertical profiles of particle mas flux, concentration and streamwsise velocity. However, the description of snow saltation in a blowing snow model is also dependent on the parameterizations used for the fluid threshold, the particle size distribution, and the implementation of the lower boundary condition for the snow suspension scheme. Therefore, a complete assessment of a saltation model must take these parameterizations into account. In addition, the height at which the lower boundary condition is specified must be in agreement

with the assumed parameterizations. The actual value used (which is typically given by the height of the saltation layer) is rather irrelevant. However, one must guarantee that all parameterizations that constitute the saltation model, as well as the assumptions behind the equations used to describe snow suspension are valid at that height.

This chapter offers a comprehensive description of snow saltation parameterizations, useful for both modelers and experimentalists. By pinpointing where most of the uncertainty lies, this analysis has motivated most of the work presented in this thesis. Hopefully, it will also motivate further studies in the field.

# 3 The LES-LSM model

In this chapter, the numerical model used to investigate snow saltation dynamics is presented. It comprises a Large Eddy Simulation (LES) flow solver, a Lagrangian stochastic model (LSM) to compute the particle trajectories, and a set of parameterizations that represent the processes of aerodynamic entrainment, rebound and splash (Comola, 2017; Comola & Lehning, 2017). These three pillars of the model are presented in sections 3.1, 3.2 and 3.3, respectively. A detailed explanation of the model equations and their numerical solution is already available in previous works (e.g., Comola, Giometto, et al., 2019; Comola, 2017; Sharma et al., 2018). Therefore, in this chapter, more focus is given to the modeling options and to their ability to represent the process of snow saltation. The main conclusions are summarized in section 3.4.

## 3.1 Flow solver

The three-dimensional wind field is solved with the Large Eddy Simulation (LES) technique. Turbulence features larger than the grid size are resolved by the filtered continuity and Navier-Stokes equations, while the effect of smaller eddies is parameterized by a sub-grid scale (SGS) model. The LES model used along with the particles solver is named EPFL-LES. It was developed at the Ecole Polytechnique Fédérale de Lausanne and is based on the work of Albertson and Parlange (1999).

The LES code targets atmospheric boundary layer (ABL) flows, assumed incompressible and driven by a constant streamwise pressure gradient, $\partial p_\infty / \partial x$ [Pa m$^{-1}$]:

$$\frac{\partial p_\infty}{\partial x} = -\rho_a \frac{u_*^2}{L_z} \tag{3.1}$$

where $L_z$ [m] is the domain height. In the absence of saltating particles, this imposed pressure gradient guarantees a surface shear stress, $\tau_s$, equal to $\rho_a u_*^2$.

Horizontal gradients are computed with a Fourier-based pseudo-spectral approach and vertical gradients are calculated using second-order finite differences. The time derivatives are computed with the second-order Adams-Bashforth time advancement scheme (Canuto et al., 1988). In the present code version, the closure SGS model is given by the scale-dependent Lagrangian dynamic model (LASD) as proposed by Bou-Zeid et al. (2005). This model exhibits better dissipation characteristics than the classic Smagorinsky and the scale-invariant dynamic models.

Periodic boundary conditions are imposed in the vertical walls of the computational domain, as required when applying Fourier transforms, allowing for the development of a fully turbulent flow at both the inlet and outlet sections. At the top boundary, impermeability and zero vertical gradients are assumed. At the bottom boundary, the impermeability condition is imposed and the wall shear stress is given by the logarithmic law of the wall. The use of wall functions avoids highly discretized meshes near the surface as well as smaller time steps to ensure numerical stability. However, care must be taken to guarantee that the first vertical grid point is within the logarithmic sub-layer ($z_1^+ = u_* z_1 / \nu_a \approx 100$, where $z_1$ [m] is the height of the first grid point above the surface and $\nu_a$ [m$^2$ s$^{-1}$] is the air kinematic viscosity). Over smooth surfaces, the logarithmic law can be replaced by a more overarching wall function (Spalding-type). However, over rough surfaces, the viscous and buffer sub-layers are replaced by a roughness sub-layer (Jiménez, 2004). Unfortunately, measurements of the flow velocity in this region are difficult to obtain because of the proximity to the roughness elements (Schultz & Flack, 2007). This limits the accurate characterization of the wind field over a rough surface below the logarithmic region.

For a given combination of surface roughness and friction velocity, the air flow might not be fully rough. This occurs when $Re_{k_s} = k_s u_* / \nu_a < 70$, where $Re_{k_s}$ is the roughness Reynolds number and $k_s$ [m] is the characteristic roughness height. $k_s$ is related to the roughness length, $z_o$ [m], which is typically used to characterize the surface roughness in the logarithmic law. However, when the surface is neither fully rough neither aerodynamically smooth ($5 < Re_{k_s} < 70$), the value of $z_o$ is a function of $u_*$ (e.g., Durán et al., 2012; Kok et al., 2012). Therefore, the assumption that $z_o$ is constant and only dependent on the granular bed characteristics stops being valid. This imposes a constraint to the range of air flows/granular surfaces that can be correctly simulated by a simple logarithmic wall function.

The present LES code has been used in multiple ABL studies concerning land-atmosphere interaction over complex terrains, wind-farms and urban canopy (Albertson & Parlange, 1999; Bou-Zeid et al., 2005; Diebold et al., 2013; Giometto et al., 2017; Giometto et al., 2016; Sharma et al., 2017). A detailed description of the model can be found in these works.

## 3.2   Particle dynamics

Particle motion is computed in a Lagrangian framework. The coupling with the LES solver was developed by Comola (2017), following the work of Groot Zwaaftink et al. (2014). The model

has been further developed with the contributions of Comola and Lehning (2017), Sharma et al. (2018) and Comola, Giometto, et al. (2019).

Particle inertia, gravity and the drag force applied to the particles are related by Newton's second law. Aerodynamic drag, $D_i$ [N], is given by $D_i = -1/2 C_D \rho_a A_f |V_R| V_{R,i}$, where $i = 1, 2, 3$ denotes the $x$, $y$ and $z$ directions in the Cartesian coordinate system. $C_D$ is the drag coefficient, $A_f$ [m$^2$] is the particle frontal area, $V_{R,i}$ [m s$^{-1}$] the particle velocity relative to the local flow and $|V_R|$ [m s$^{-1}$] its absolute value (henceforth referred to as $V_R$). In the current model, saltating particles are assumed spherical, with a frontal area $A_f = \pi d^2/4$, and with approximately the density of ice. The drag coefficient is estimated using the expression proposed by Schiller and Nauman (1933). It is a function of the particle Reynolds number, $Re_d = V_R d / \nu_a$:

$$C_D = \frac{24}{Re_d} \left( 1 + 0.15 Re_d^{0.687} \right). \tag{3.2}$$

This expression was obtained from fitting experimental measurements developed with spherical particles of multiple sizes and is valid for $Re_d < 800$. Hence, it describes both the Stokes and transition flow regimes, which are characteristic of aeolian saltation.

The assumption of spherical particles is widely used in saltation models (e.g., Doorschot & Lehning, 2002; Nemoto & Nishimura, 2004; R. A. Schmidt, 1980) and in optical measurements of snow size distribution and mass flux (e.g., Crivelli et al., 2016; Guala et al., 2008). Even though snowfall particles can have multiple shapes according to the meteorological conditions upon formation, particles in saltation exhibit a different shape and size distribution than falling snow: they are generally smaller, denser and more rounded (Nishimura & Nemoto, 2005; Walden et al., 2003; Woods et al., 2008) due to particle fragmentation after multiple impacts with the bed (Comola et al., 2017). In fact, a layer of wind packed snow composed of small and closely-packed grains is commonly observed after snow transport events (Fierz et al., 2009). These observations support the assumption of spherical particles when modeling the wind-particle interaction in steady-state saltation. However, wind tunnel measurements performed with natural snow revealed that the drag coefficient of freshly fallen particles in saltation is higher than the value predicted by equation 3.2 (Appendix A). These results are in agreement with the findings of Dietrich (1982) when studying the settling velocity of naturally shaped sand particles. Indeed, the drag coefficient is expected to be slightly higher for non-spherical particles because geometrical deviations from a spherical shape can encompass high curvature regions that promote flow separation. Therefore, equation 3.2 might not be a good approximation to represent fresh snow at saltation onset or the occurrence of snow saltation with concurrent snowfall. Different drag laws can be employed, as for example those proposed by Tagliavini et al. (2021) for falling snow crystals. The findings of the wind tunnel experiments presented in Appendix A also indicate that the density of saltating particles might not be well approximated by the density of ice, especially when considering freshly fallen snow. This hypothesis is in agreement with the measurements of Leinonen et al. (2018) and Rees

et al. (2021).

The equation for particle trajectory yields:

$$d v_i = \left[ \frac{3}{4} \frac{\rho_a}{\rho_p} \frac{C_D}{d} V_R (u_i - v_i) - g\delta_{i3} \right] dt \tag{3.3}$$

where $v_i$ [m s$^{-1}$] is the particle velocity, $u_i$ [m s$^{-1}$] is the instantaneous flow velocity resolved by the LES solver, $\rho_p$ [kg m$^{-3}$] is the particle density, $t$ [s] is the time and $\delta$ is the Kronecker delta. Equation 3.3 is solved numerically with a first-order forward Euler method.

In addition to the electrostatic forces and those from mid-air collisions (discussed in section 2.2), the effect of aerodynamic lift is also neglected in the particles' momentum balance. The lift force induced by particle rotation (Magnus effect) and the sheared flow (Saffman, 1965) was investigated by several authors (e.g., Durán et al., 2011; Huang et al., 2010; White & Schulz, 1977). According to Kok et al. (2012), the effect of particle rotation can be significant depending on the particle angular velocity, but the Saffman forces are expected to be much smaller than gravity. Wind tunnel experiments of snow saltation performed with natural snow present some evidence that aerodynamic lift is indeed significantly smaller than aerodynamic drag (Appendix A). These results support the current assumption, but further investigation is needed to fully asseess the effect of lift on snow particles in saltation.

In previous works based on this model (Comola, Giometto, et al., 2019; Groot Zwaaftink et al., 2014; Sharma et al., 2018), the non-resolved SGS velocities were computed. Then, the instantaneous wind field was derived from the sum of the resolved wind velocity field, $u_i$, and the SGS velocities. The modeling of sub-grid scale velocities is important when using simple flow models, as COMSALT (Kok & Renno, 2009), or RANS solvers (Nemoto & Nishimura, 2004). In these models, turbulence is not resolved and a model for high-frequency velocity fluctuations is imperative. However, the importance of such a model is less clear for LES, as the large-scale instantaneous turbulent flow is provided as a solution of the flow solver. In fact, Dupont et al. (2013) concluded that the SGS velocities have a negligible effect on particle trajectories. Moreover, Z. Wang et al. (2019) did not consider the SGS velocities when modeling saltation with an LES solver. The impact of SGS velocities on particle trajectories may also depend on the SGS model employed, even though there are no works in the literature regarding this question. In the simulations performed, the effect of the SGS turbulence features on the resolved wind velocity field is modeled with one of the most advanced SGS closure schemes, the LASD (Bou-Zeid et al., 2005). Thus, the effect of the SGS velocities on particle motion is assumed to be negligible and not taken into account.

The effect of snow sublimation is also neglected in the studies here developed. This simplifies the analysis and avoids the computational cost of solving the thermodynamic interaction between the particles and the air. Recent studies have shown that snow sublimation can be

significant in the saltation layer, despite the high values of relative humidity (Sigmund et al., 2022; Z. Wang et al., 2019). Therefore, the modeling of particle sublimation is particularly important when assessing heat and water vapor transport in the atmosphere during snow transport events. However, this is outside the scope of this thesis. The effect of snow sublimation on particle dynamics itself is restricted to a reduction in particles size and to an increase in particles sphericity.

The feedback of particle motion on flow momentum is modelled through a source term, $S_i$ [N m$^{-3}$], in the filtered Navier-Stokes equations. $S_i$ is equal in magnitude and opposite to the total aerodynamic drag applied to the particles per unit volume. The contribution of each particle is linearly extrapolated to the nearest eight grid nodes where LES is resolved.

Periodic boundary conditions are applied to particles exiting the domain through its vertical walls. Particles that reach the top boundary are assumed to leave the domain and those impacting the bottom boundary (erodible bed) may rebound and eject other grains as described in section 3.3.

In order to reduce the computational cost of the simulations, particles are not modelled individually but grouped in parcels, constituted by particles of equal size that follow the same trajectory. Particles from the same parcel were aerodynamically entrained at the same surface location and time step, or were ejected from the same impact event. This assumption is considered reasonable for the analysis of steady-state saltation presented in the following chapters.

Different studies have been conducted with previous and current versions of this model concerning snow saltation variability (Groot Zwaaftink et al., 2014), blowing snow sublimation (Sharma et al., 2018; Sigmund et al., 2022) and preferential deposition over hills (Comola, Giometto, et al., 2019). A detailed description of the model algorithm and a comparison between simulation results and field/wind tunnel measurements can be found in these works.

## 3.3 Surface processes

The interaction between surface grains, the wind flow and particles impacting the bed is described by three main processes: aerodynamic entrainment, rebound and splash. These surface processes are modelled with statistical models based on physical principles and experimental correlations, as proposed by Groot Zwaaftink et al. (2014) and further developed by Comola and Lehning (2017).

This approach reduces the computational cost associated with the direct numerical simulation of particle interactions within the granular bed. Saltation models based on DEM simulate these complex interactions, but are not suitable for simulating particle transport over large computational domains (Comola, Gaume, et al., 2019; Durán et al., 2012; Pähtz et al., 2015).

### 3.3.1 Aerodynamic entrainment

When a fluid flows over a granular and erodible bed, surface particles can be moved and eventually lifted by the flow. This process is called aerodynamic entrainment and occurs when the fluid surface shear stress grows above a given threshold. This threshold, that defines the start of wind erosion, is estimated by considering the forces applied on a grain laying on the bed and by performing a balance of angular momentum. The quantity of interest is the minimum aerodynamic force that makes the grain rotate over its leeward point of contact with the underlying grains and, eventually, leads to an uplift of the grain (Bagnold, 1941).

In general, this threshold shear stress is modeled as a mean quantity, related to the instantaneous aerodynamic force by a parameterization. Bagnold (1941) named it the fluid threshold, $\tau_{ft}$. This quantity was previously introduced in section 2.2.1 when discussing parameterizations for the surface shear stress. Considering particle weight, buoyancy and drag, Bagnold (1941) proposed the following well-known expression:

$$\tau_{ft} = A^2 \left( \rho_p - \rho_a \right) g d \tag{3.4}$$

where $A$ is the fluid threshold coefficient, which depends on different flow and particle characteristics. Chepil (1959) deduced an expression for $A$, function of the turbulence intensity, particle geometry and drag coefficient, estimated by a series of experiments developed with sand and soil grains. Bagnold (1941) proposed $A = 0.1$ for sand beds, after a series of wind tunnel and field experiments. A higher value is expected for very small particles like dust. In this case, the granular surface is not aerodynamically rough and a thin viscous sub-layer is present close to the surface, which limits the transport of flow momentum to the bed. Different criteria have been proposed to define the onset of aerodynamic entrainment. A summary of the latest developments can be found in Pähtz et al. (2020).

Interparticle forces, as the van der Waals and electrostatic forces and those induced by interparticle bonds, also play a role in the aerodynamic entrainment of cohesive materials as snow or moist soils (R. A. Schmidt, 1980; Shao & Lu, 2000). However, the quantification of such forces is still a challenge. The contribution of interparticle ice bonds in the calculation of the fluid threshold is of special interest when studying the erosion of snow-covered surfaces and was firstly addressed by R. A. Schmidt (1980). However, for common interparticle bond radius, the values estimated for $\tau_{ft}$ were too large for pure aerodynamic entrainment of snow particles to occur. Other authors, as Lehning et al. (2000) and Clifton et al. (2006), used the same approach suggested by R. A. Schmidt (1980), but adjusted the bond properties and empirical constants to improve the agreement with wind tunnel tests performed with natural snow beds. The values for $\tau_{ft}$ obtained during wind tunnel and field experiments are lower than those deduced by R. A. Schmidt (1980), possibly because patches of loose snow grains are always present over dry snow surfaces. These grains can be easily lifted by the flow and

contribute to the development of saltation by further ejecting other particles. Moreover, bed microtopography can also induce local peaks in shear stress, leading to the preferential entrainment of grains more exposed to the airflow. The contribution of interparticle cohesion to the fluid threshold can also be taken into account by adjusting the value of the fluid threshold coefficient. For example, Clifton et al. (2006) proposed a value of $A = 0.18$ from fitting equation 3.4 to wind tunnel measurements developed with different snow surfaces.

In light of the challenges and uncertainties to correctly quantify the effect of interparticle forces on the fluid threshold, these forces are not taken into account in the calculation of $\tau_{ft}$. Hence, $\tau_{ft}$ is computed from equation 3.4, considering the grain mean diameter at the bed, $\bar{d}$ [m], and a constant value for $A$ equal to 0.1 as proposed by Bagnold (1941). This is a simpler approach suitable for the study of saltation events where the contribution of aerodynamic entrainment is expected to be negligible in comparison to rebound/splash entrainment (Kok et al., 2012). As previously discussed in section 2.2.1, for non-cohesive materials like sand, the surface shear stress stays below the fluid threshold during steady-state saltation, which strongly reduces the occurrence of aerodynamic entrainment (e.g., Bagnold, 1941; Owen, 1964). For cohesive material like snow, wind tunnel measurements performed by Paterna et al. (2017) have also shown the predominance of rebound/splash mechanisms over aerodynamic entrainment when the wind strength is sufficiently strong for steady-state saltation to develop. However, as previously discussed in section 2.2.1, some numerical models of snow saltation arrived to a surface shear stress lower than the fluid threshold (Doorschot & Lehning, 2002; Niiya & Nishimura, 2017). The assumption that aerodynamic entrainment can be neglected in comparison to rebound/splash during steady-state saltation revealed to be acceptable for the analysis presented in chapter 4. However, this assumption is challenged in chapter 5, when considering low friction velocities. This highlights the need for a more accurate description of the fluid threshold, especially when studying low friction velocities and intermittent saltation.

The number of grains entrained per unit area per unit time, defined as the aerodynamic entrainment rate, $N_{ae}$ [m$^{-2}$ s$^{-1}$], is computed using the expression proposed by Anderson and Haff (1991):

$$N_{ae} = \eta \left( \tau_s - \tau_{ft} \right) \tag{3.5}$$

where $\eta$ [N$^{-1}$ s$^{-1}$] is the entrainment coefficient, computed with the expression proposed by Doorschot and Lehning (2002):

$$\eta = \frac{C_{ae}}{8\pi \bar{d}^2} \tag{3.6}$$

where the coefficient $C_{ae}$ [m$^2$ N$^{-1}$ s$^{-1}$] is set to 1.5 m$^2$ N$^{-1}$ s$^{-1}$ (Groot Zwaaftink et al., 2014).

Table 3.1: Initial velocity of aerodynamically entrained, splashed and rebounding grains: distribution type, mean and standard deviation.

| | Distribution | Mean | Std. | References |
|---|---|---|---|---|
| **Aerodynamic entrainment** | | | | |
| Velocity magnitude | Lognormal | $3.5u_{*,s}$ | $2.5u_{*,s}$ | Clifton and Lehning (2008) |
| Vertical angle[1] | Lognormal | $75 - 55\left[1 - \exp\left(-\frac{d}{175\times 10^{-6}}\right)\right]$ | 15 | Clifton and Lehning (2008) |
| **Rebound** | | | | |
| Velocity magnitude | - | $\sqrt{\epsilon_r}\,|v_i|$ | - | Kok and Renno (2009) |
| Vertical angle[1] | Exponential | 45 | - | Kok and Renno (2009) |
| **Splash** | | | | |
| Velocity magnitude | Exponential | $0.25|v_i|^{0.3}$ | - | Sharma et al. (2018) |
| Vertical angle[1] | Exponential | 50 | - | Rice et al. (1995, 1996) |
| Horizontal angle[2] | Normal | 0 | 15 | Xing and He (2013) |

Velocities are in units of m s$^{-1}$, angles are in degrees and the grain size is in meters.

[1] Measured from a horizontal plane (downwind between 0° and 90°).

[2] Measured from the plane of particle impact.

Recently, different expressions for $N_{ae}$ have been proposed (e.g., G. Li et al., 2020). Further studies are needed to investigate the model sensitivity to this parameter.

As we are interested in modeling transport limited saltation - a saltation regime for which the amount of saltating particles is only limited by the availability of wind momentum (Kok et al., 2012) - the initial particle concentration at the surface is considered high enough so that there is never a shortage in the supply of erodible particles. This assumption is appropriate for the study of steady-state saltation. However, this is not always the case in snow-covered regions, where thin erodible snow layers can exist on top of hard and sintered snow.

In the model, entrained particles start their trajectory at a height of four times the mean grain diameter. The initial velocity and vertical angle of ejection are defined according to a lognormal distribution as proposed by Clifton and Lehning (2008). The mean and standard deviation of the distribution are computed with the expressions presented in Table 3.1. The horizontal angle of ejection is given by the horizontal flow direction.

### 3.3.2   Rebound

After impacting the surface, a grain may rebound and eject other particles laying on the bed. The probability of rebound, $P_r$, is described by the expression proposed by Anderson and Haff (1991):

$$P_r = P_m\left[1 - \exp\left(-\gamma|v_i|\right)\right] \tag{3.7}$$

where $P_m$ is the maximum probability of rebound, equal to 0.9 as proposed by Groot Zwaaftink et al. (2014) for snow particles, $\gamma$ [s m$^{-1}$] is a constant set to 2 s m$^{-1}$ (Anderson & Haff, 1991) and $|v_i|$ [m s$^{-1}$] is the modulus of the particle velocity at impact.

The velocity of rebound, $|v_r|$ [m s$^{-1}$], is given by $|v_r| = \sqrt{\epsilon_r}|v_i|$, where $\epsilon_r$ is the fraction of kinetic energy retained by the rebounding grain (restitution coefficient). Saltation models have shown to be highly sensitive to the value of $\epsilon_r$, which greatly depends on the particle elastic properties (Kok & Renno, 2009). Experiments developed with sand showed that $\epsilon_r$ varies according to a normal distribution (D. Wang et al., 2008). Although the restitution coefficient for snow particles is more uncertain, experiments have not suggested a significant deviation from the values obtained for sand grains (Nalpanis et al., 1993).

The horizontal angle of rebound is given by the horizontal flow direction and the vertical angle is computed from an exponential distribution. Further details are presented in Table 3.1.

### 3.3.3 Splash

When a grain impacts the bed, it can eject several grains initially at rest. This process, named splash, is generally expected to be the main driver of particle motion during steady-state saltation (Kok et al., 2012; Paterna et al., 2017). As flow momentum decreases near the surface due to particle drag, aerodynamic entrainment can become highly compromised after the start of saltation. In this case, particles impacting the ground become the main source of momentum as they travel from high momentum regions to the surface.

Numerous statistical splash functions have been proposed to estimate the number of ejected grains, $N$, and their initial velocity, $|v_e|$ [m s$^{-1}$], as a function of the impacting grain velocity, $|v_i|$, and mass, $m_i$ [kg] (e.g., Anderson & Haff, 1988; McEwan & Willetts, 1991). In the LES-LSM model, the number of ejected grains is computed from energy and momentum conservation laws, as proposed by Kok and Renno (2009) and adapted by Comola and Lehning (2017) to take into account the effect of mixed-sized grains and interparticle cohesion.

The impacting grain and the bed are regarded as an isolated system, for which energy and momentum conservation is applied. A fraction of the kinetic energy and momentum, $\epsilon_r$ and $\mu_r$, respectively, is kept by the impacting grain leading to its rebound. The remaining fraction is only partly transferred to the ejected grains, as a fraction of the impacting energy and momentum, $\epsilon_f$ and $\mu_f$, respectively, leads to the rearrangement of surface grains and, consequently, to friction related losses.

Both the energy and momentum conservation equations are solved for $N$ by statistically representing the kinetic energy and momentum of the ejected grains by their mean values. Only the horizontal direction of the momentum equation is taken into account as the vertical component of the impact velocity is relatively small (Bagnold, 1941). Comola and Lehning (2017) arrived to the following expressions:

$$N_E \quad = \quad \frac{\left(1 - P_r \epsilon_r - \epsilon_f\right) m_i v_i^2}{\langle m_e \rangle \langle v_e^2 \rangle + r_E \sigma_{m_e} \sigma_{v_e^2} + 2\phi} \tag{3.8a}$$

$$N_M \quad = \quad \frac{\left(1 - P_r \mu_r - \mu_f\right) m_i v_i \cos \alpha_i}{\langle m_e \rangle \langle v_e \rangle \langle \cos \alpha_e \rangle \langle \cos \beta_e \rangle + r_M \sigma_{m_e} \sigma_{v_e}} \tag{3.8b}$$

where $N_E$ and $N_M$ denote the number of ejected grains computed by the energy and momentum equations, respectively. In equation 3.8, the angle brackets represent averages over the $N$ ejected particles. $m_e$ [kg] is the mass of an ejected grain, $\alpha_e$ is the vertical angle of ejection and $\beta_e$ is the horizontal angle of ejection measured from the plane of impact (in the above equations, both $\alpha_e$ and $\beta_e$ are assumed statistically independent). $\sigma_{m_e}$ [kg], $\sigma_{v_e}$ [m s$^{-1}$] and $\sigma_{v_e^2}$ [m$^2$ s$^{-2}$] denote the standard deviation of $m_e$, $|v_e|$ and $|v_e|^2$, respectively. $\alpha_i$ is the vertical angle of impact, $r_E$ and $r_M$ are the correlation coefficients between $m_e$ and $|v_e|^2$ and between $m_e$ and $|v_e|$, respectively, and $\phi$ [J] is the energy required to break the cohesive bonds between each ejected grain and the surrounding ones. To simplify the notation, in equation 3.8, the variables $|v_e|$ and $|v_i|$ are represented by $v_e$ and $v_i$, respectively.

The number of ejected grains is then given by the minimum value between $N_E$ and $N_M$, which guarantees that neither energy nor momentum is created. The number of ejected grains is expected to be restricted by momentum conservation when the bed is constituted by loose grains (Kok & Renno, 2009). However, this is not always obtained when interparticle forces are present (Comola & Lehning, 2017; Shao et al., 1993).

The main difference between the splash dynamics of sand and snow particles lies indeed in the nature of the interparticle forces (Comola & Lehning, 2017). In snow, they arise from ice bonds among neighboring particles, while in sand they are caused by the occasional presence of water menisci. Several parameters in the splash functions are expected to depend on the material properties, such as the ejection velocity of splashed grains and the restitution coefficient, $\epsilon_r$. In the particular case of snow, metamorphic changes in the snow surface may induce variations in the parameters. Moreover, in the work of Doorschot et al. (2004), the authors question the occurrence of rebound and splash for fresh snow. Despite these differences, the studies of Nalpanis et al. (1993) and Nishimura and Hunt (2000) have shown some similarities between the main snow and sand splash parameters. The parameters' values considered in the simulations are therefore mainly based on sand experiments (e.g., Anderson & Haff, 1988, 1991; Kok & Renno, 2009; Rice et al., 1995, 1996; Xing & He, 2013). The velocity and angle of ejection are defined according to specific probability distributions (Table 3.1) and the parameters $\epsilon_r, \epsilon_f, \mu_r, \mu_f, r_E, r_M, \langle \cos \alpha_e \rangle$ and $\langle \cos \beta_e \rangle$ are assumed constant (Table 3.2). Sensitivity analysis carried out by Comola and Lehning (2017) revealed that the current splash model is robust to variations of up to ±20% in the model parameters. Additional studies on

Table 3.2: Parameters of the splash model.

| Parameter | Values used in the model | References |
|---|---|---|
| $\epsilon_r$ | 0.25 | Rice et al. (1995) and D. Wang et al. (2008) |
| $\epsilon_f$ | $0.96\,(1 - P_r\epsilon_r)$ | Ammi et al. (2009) |
| $\mu_r$ | $\sqrt{\epsilon_r}$ | - |
| $\mu_f$ | 0.4 | Rice et al. (1995) |
| $r_E$ | 0 | - |
| $r_M$ | 0 | - |
| $\langle\cos\alpha_e\rangle$ | 0.75 | Rice et al. (1995) |
| $\langle\cos\beta_e\rangle$ | 0.96 | Xing and He (2013) |
| $\phi$ [J] | $0, 10^{-10},\ 5\times10^{-10}, 5\times10^{-9}$ | Gauer (2001) |

the splash mechanics of natural snow (see e.g., Araoka & Maeno, 1981; Nishimura & Hunt, 2000) would ultimately help reducing the model uncertainties.

The correlation coefficients, $r_E$ and $r_M$, are set to zero, as in Comola and Lehning (2017). The mean and standard deviation of the mass of ejected grains are computed according to the assumed size distribution. Finally, the cohesion energy, $\phi$, is either set to different figures, according to the range proposed by Gauer (2001) and investigated by Comola and Lehning (2017) (chapter 4), or set to zero (chapter 5).

## 3.4 Conclusions

Snow saltation is a complex phenomenon characterized by detailed particle-wind-bed interactions. In order to correctly simulate the particle-wind interaction, the current model solves the turbulent flow with one of the most sophisticated methods: the LES technique. By making use of high performance computing, the coupling of the LES flow solver with the Lagrangian model allows the accurate calculation of the turbulent flow and its interaction with the particles aloft throughout a domain of $O(1-10)$ m size length.

The current LES-LSM coupling has nevertheless some limitations, for instance, related to the fact that the snow particles in saltation are not perfectly spherical. Further studies are needed to correctly quantify the drag force applied to the snow particles, as well as the errors introduced by neglecting other forces, such as aerodynamic lift or electrostatic forces. The density of the snow particles in saltation, which is seldom discussed, is also another uncertain parameter, especially when considering freshly fallen snow.

Taking into account the wall-time imposed by both the LES and the Lagrangian model, a detailed description of the particle-bed interaction is not possible (resolved, for instance, in DEM-based models) and statistical parameterizations must be considered. However, the currently used parameters are based on a limited number of experimental measurements. In order to reduce the uncertainty of the model inner parameters, further studies of the aerodynamic entrainment, rebound and splash processes over natural snow beds are required, as well as detailed field measurements characterizing both the wind speed, the snow bed, and

the particles in saltation.

In addition, further efforts must be made to fully model the effect of the bed characteristics on snow saltation. For instance, interparticle cohesion is also expected to influence the particle ejection velocity during splash and the fluid threshold for the onset of aerodynamic entrainment (Comola et al., 2022). Moreover, even though a layer of wet snow and a layer of hard-sintered snow are both characterized by a given level of interparticle cohesion, these two layers have different elastic properties. Therefore, they must be characterized by different restitution coefficients. In addition, the strength of interparticle bonds between grains that did not leave the surface and between those that failed to rebound might not be the same. These different aspects are not yet taken into account in the model. From the experimental work side, a correlation between interparticle cohesion and meteorological conditions or measurable snow properties, such as snow density or snow hardness, is still needed.

Despite the mentioned uncertainties, detailed models, as the one presented, are ideal to simulate both the flow and the snow surface particularities. By explicitly solving the turbulent flow, particle trajectories and the surface processes, the LES-LSM can be used to improve our understanding of the particle-wind-bed interactions and to evaluate some of the assumptions made in simple saltation models.

# 4 The effect of the granular bed proper- ties on snow saltation

In this chapter, the LES-LSM model is used to study the saltation system, in particular the effect of the granular bed characteristics on its dynamics. The capabilities of the model to simulate steady-state saltation are firstly assessed. The vertical profiles of wind velocity, particle mass flux, concentration and streamwise velocity are analyzed, as well as the variation of the transport rate with the friction velocity. Then, a detailed study on the effect of grain size and interparticle cohesion on the vertical profiles, transport rate and surface friction velocity is performed. To this end, the properties of the granular bed are varied in a systematic way in a suite of simulations, which cover a range of wind velocities. The results are compared to existing saltation models and to the conclusions drawn from the latest wind tunnel and field experiments. In section 4.1, the numerical setup used for the simulations and the data post-processing are presented. The results are shown and discussed in section 4.2 and the main conclusions are summarized in section 4.3.

## 4.1 Numerical setup

### 4.1.1 General settings

A cubic domain of 6.4 m side length is used to model the near-surface atmospheric flow over a flat erodible bed. The domain is relatively short in both horizontal directions, specially in the streamwise one. This is partially compensated by applying periodic boundary conditions. However, the use of a longer domain is necessary for the consistent development of large coherent structures observed in experimental and numerical boundary layer studies (Munters et al., 2016). Even though longer domains are imperative for a proper comparison with field measurements, the chosen domain was considered adequate for the study of steady-state saltation developed in this chapter. Moreover, it preserves the computational time within acceptable figures.

The domain is discretized in 64 cells of equal size in the streamwise and crosswise directions. The vertical direction is discretized in 128 cells using a hyperbolic function. The hyperbolic

function guarantees a more refined mesh close to the bottom boundary, with an approximately constant thickness of 1 cm in the first 15 cm. The first grid center point is placed in the logarithmic sub-layer, at approximately 0.5 cm height.

The simulations are performed over a total of 350 s to allow the development of steady-state saltation. The time step is set to $5 \times 10^{-5}$ s for both the flow and particle solvers. The flow is allowed to develop over 25 s prior to the start of surface erosion.

The initial streamwise component of the velocity field is given by a logarithmic profile, function of $u_*$ and of the roughness length, $z_o$, which is assumed constant along the surface and equal to $10^{-5}$ m. The initial crosswise and vertical velocity components are set to zero. White noise is added to all initial velocity components to accelerate the development of a fully developed turbulent flow.

The fluid density and kinematic viscosity are set to $\rho_a = 1.34$ kg m$^{-3}$ and $\nu_a = 1.24 \times 10^{-5}$ m$^2$ s$^{-1}$, respectively. Particles are modelled as ice spheres with density $\rho_p = 918.4$ kg m$^{-3}$. The top of the erodible surface is defined at a height $z = 0$ m and the particle size is assumed uniform or defined by a lognormal distribution, characterized by the grain mean diameter, $\bar{d}$, and the standard deviation of the distribution, $\sigma_d$ [m]. The minimum and maximum particle diameters are set to 0.05 and 2 mm, respectively.

### 4.1.2 Simulation details

In order to study the effect of friction velocity, mean grain size, size distribution and cohesion energy on saltation dynamics, four groups of simulations are performed - S1 to S4 - for which different values of $u_*$, $\bar{d}$, $\sigma_d$ and $\phi$ are considered. The parameters used in each simulation group are summarized in Table 4.1.

In simulations S1 and S2, a bed of equally-sized ($\sigma_d = 0$ $\mu$m) and loose grains ($\phi = 0$ J) is modeled. In S1, the effect of the friction velocity outside the saltation layer is studied while keeping the remaining parameters unchanged. In S2, different values for the grain diameter, $\bar{d}$, are tested. In simulations S3 and S4, a bed of mixed-sized grains is modeled by describing the grain size by a lognormal distribution. In S3, the effect of the standard deviation of the distribution, $\sigma_d$, on steady-state saltation is analyzed. Finally, in S4, interparticle forces are assumed between surface grains and different values for the cohesion energy, $\phi$, are tested. Different values for $u_*$ are also considered in simulations S2 to S4.

The fluid threshold coefficient is set to $A = 0.1$ and the splash model parameters are set to the values presented in Table 3.2. In all simulations, the number of particles per parcel can assume values between 5000 and 250000. As a consequence, the number of parcels aloft varies from 5000 to 20000 during steady-state conditions, for friction velocities ranging from 0.4 to 0.8 m s$^{-1}$.

Table 4.1: Simulation input parameters.

| | Description | $u_*$ [m s$^{-1}$] | $\bar{d}$ [μm] | $\sigma_d$ [μm] | $\phi$ [J] |
|---|---|---|---|---|---|
| S1 | Effect of friction velocity | 0.3 - 0.8 | 200 | 0 | 0 |
| S2 | Effect of mean grain diameter | 0.4 - 0.8 | 100, 300, 400 | 0 | 0 |
| S3 | Effect of size distribution | 0.4 - 0.8 | 200 | 100, 200 | 0 |
| S4 | Effect of cohesion | 0.4 - 0.8 | 200 | 100 | $10^{-10}, 5\times10^{-10}, 5\times10^{-9}$ |

### 4.1.3   Data post-processing

The vertical profiles of particle concentration, mean particle streamwise velocity and particle mass flux are computed by dividing the computational domain in horizontal layers of thickness $\Delta z_k$ [m].

The particle concentration, $c$, is given by

$$c(z_k) = \frac{\sum_{n=1}^{N_k} m_n}{L_x L_y \Delta z_k} \tag{4.1}$$

where $N_k$ is the number of particles in the horizontal layer with mean height $z_k$ [m], $m_n$ [kg] is the mass of the $n^{th}$ particle, $L_x$ [m] is the domain length and $L_y$ [m] is the domain width.

The particle streamwise velocity at each layer $k$, $\bar{v}_x(z_k)$, is given by the arithmetic mean of the streamwise velocity of the $N_k$ particles. The particle mass flux, $q$, is given by the product of the particle concentration and the mass-weighted average particle streamwise velocity, yielding

$$q(z_k) = \frac{\sum_{n=1}^{N_k} m_n v_{x_n}}{L_x L_y \Delta z_k} \tag{4.2}$$

where $v_{x_n}$ [m s$^{-1}$] is the instantaneous streamwise velocity of the $n^{th}$ particle in layer $k$.

The transport rate, $Q$, is computed by integrating the particle mass flux, $q$, along the height, from the surface to 15 cm. The last 100 s of each simulation are used to compute the time-averaged values of $c$, $\bar{v}_x$, $q$ and $Q$. During this time interval (250 s - 350 s), the changes in total mass of particles aloft are negligible and saltation is assumed to be in steady-state.

The surface friction velocity, $u_{*,s}$, at each time step is obtained by averaging over the surface. The respective time-averaged value obtained for the last 100 s of each simulation is defined as the equilibrium surface friction velocity, $u_{*,eq}$ [m s$^{-1}$].

## 4.2   Results and discussion

In this section, the results are presented and discussed. Results obtained with simulations S1 to S4 are analyzed in sections 4.2.1 to 4.2.4, respectively. Moreover, a comparison with existing saltation models and with the conclusions drawn from the latest wind tunnel and field experiments is presented.

### 4.2.1   The effect of friction velocity

In simulations S1, a bed of equally-sized and loose grains with a diameter of 200 $\mu$m is modelled. The streamwise wind speed profiles are presented in Figure 4.1. They are computed by averaging the streamwise wind velocity along horizontal planes. The profiles are time-averaged over the first 25 s and over the last 100 s of each simulation (before saltation onset and during steady-state saltation). As expected, the resulting wind speed is lower for the latter, as the saltation layer acts on the flow as an additional sink of momentum.

The velocity profiles obtained during steady-state saltation intercept in a point at approximately 7 mm above the surface - the focus point (inset in Figure 4.1). This characteristic feature of steady-state saltation was originally observed by Bagnold (1941) and discussed in section 2.3.2. Previous saltation models have characterized the wind velocity profile in the saltation layer using a logarithmic profile and have assumed the existence of a focus point (e.g., Pomeroy & Gray, 1990). This greatly simplifies the description of the velocity field in the saltation layer and, consequently, the theoretical modeling of saltation. The height of the focus point is expected to vary between 1 and 10 mm (Bagnold, 1941; Kok et al., 2012). In order to accurately assess its location, a more refined mesh near the surface would have to be employed.
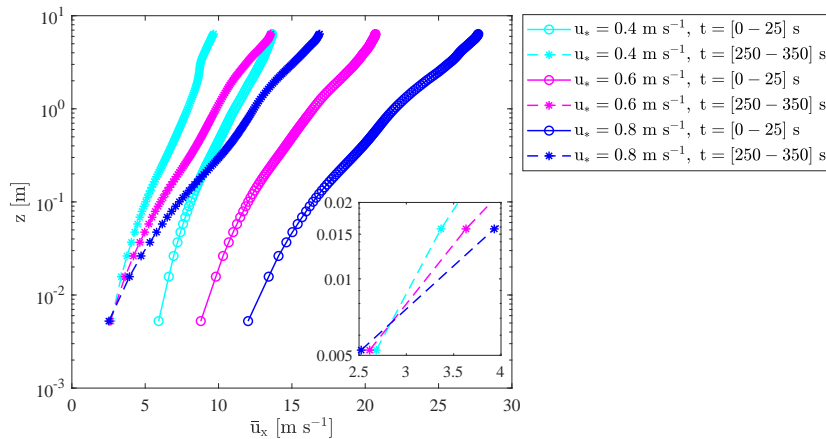


Figure 4.1: Vertical profiles of mean streamwise wind speed obtained before saltation onset and during steady-state saltation (simulations S1). The inset is a zoom-in to the near-surface region during saltation.

An equivalent surface roughness, characteristic of each saltation layer, can be estimated from the velocity profiles obtained during steady-state saltation (Dupont et al., 2013). By extending the velocity profiles down to the wall, zero velocity is attained at greater heights as $u_*$ increases. Hence, the equivalent surface roughness increases with $u_*$. This is related to an enhanced momentum exchange between the fluid flow and the particles aloft when $u_*$ increases. Therefore, it is ultimately related to the increase in particle mass flux.

The time-averaged vertical profiles of particle mass flux, concentration and mean streamwise velocity are presented in Figures 4.2a-c. The average is performed over the last 100 s of each simulation. Particle mass flux decreases with height and increases with $u_*$ (Figure 4.2a), as previously observed in field measurements (Nishimura et al., 2014). A similar trend is observed for particle concentration (Figure 4.2b). As discussed in section 2.3.3, several saltation models have assumed an exponential decay for the vertical profile of particle mass flux of the form of equation 2.4 (Clifton et al., 2006; Martin & Kok, 2017; Nishimura & Hunt, 2000; Vionnet et al., 2014). In Figure 4.3, the vertical profiles of particle mass flux are presented in a semi-logarithmic scale, together with the fitting of the simulation results to an exponential decay. The fit is performed up to a height of 3, 5 and 14 cm for $u_*$ equal to 0.4, 0.6 and 0.8 m s$^{-1}$, respectively. Moreover, the first mass flux value above the surface is neglected in the fit. The decay height, $\delta_q$, obtained from the fit and from the expression proposed by Nishimura and Hunt (2000) is also indicated at each exponential curve. It can be seen that the particle mass flux decreases exponentially with height in the first centimeters above the ground, which contrasts with the assumption of a constant particle mass flux in the saltation layer made by Pomeroy and Gray (1990) (see discussion in section 2.2.4). Moreover, a slight increase of $\delta_q$ with $u_*$ is obtained, which implies a weak variation of the saltation layer height with $u_*$. This trend is in agreement with the field measurements of Namikas (2003) and Martin and Kok (2017) developed with sand. However, it contrasts with the stronger increase proposed by Nishimura and Hunt (2000) and the wind tunnel measurements of Sugiura et al. (1998).

The particle streamwise velocity increases with height and $u_*$ (and, therefore, with wind speed), as shown in Figure 4.2c. For heights smaller than 1 cm (approximately), the variation of particle streamwise velocity with $u_*$ is negligible (inset in Figure 4.2c). This is predicted by existing saltation models (Kok & Renno, 2009) and wind tunnel measurements (Ho et al., 2011) as discussed in sections 2.2.2 and 2.3.2. This result is also obtained theoretically, based on the notion that steady-state saltation is characterized by a mean replacement capacity equal to one (Kok et al., 2012). This means that, on average, one grain enters the saltation layer each time an impacting grain fails to rebound. Assuming that saltation is mainly dominated by splash, this condition is met for a given impact velocity, which completely defines the number of ejected grains and the probability of rebound for a given bed type (see equations 3.7 and 3.8). Hence, it follows that the particle speed near the surface is independent of $u_*$ and rather varies with the bed characteristics. The near-surface particle speed is closely linked to the focus point (or Bagnold's focus) observed in the average streamwise wind speed profiles (Figure 4.1). Saltating particles are accelerated by the flow along their trajectories, therefore, the near-surface particle speed can only be approximately invariant with regards to $u_*$ if the
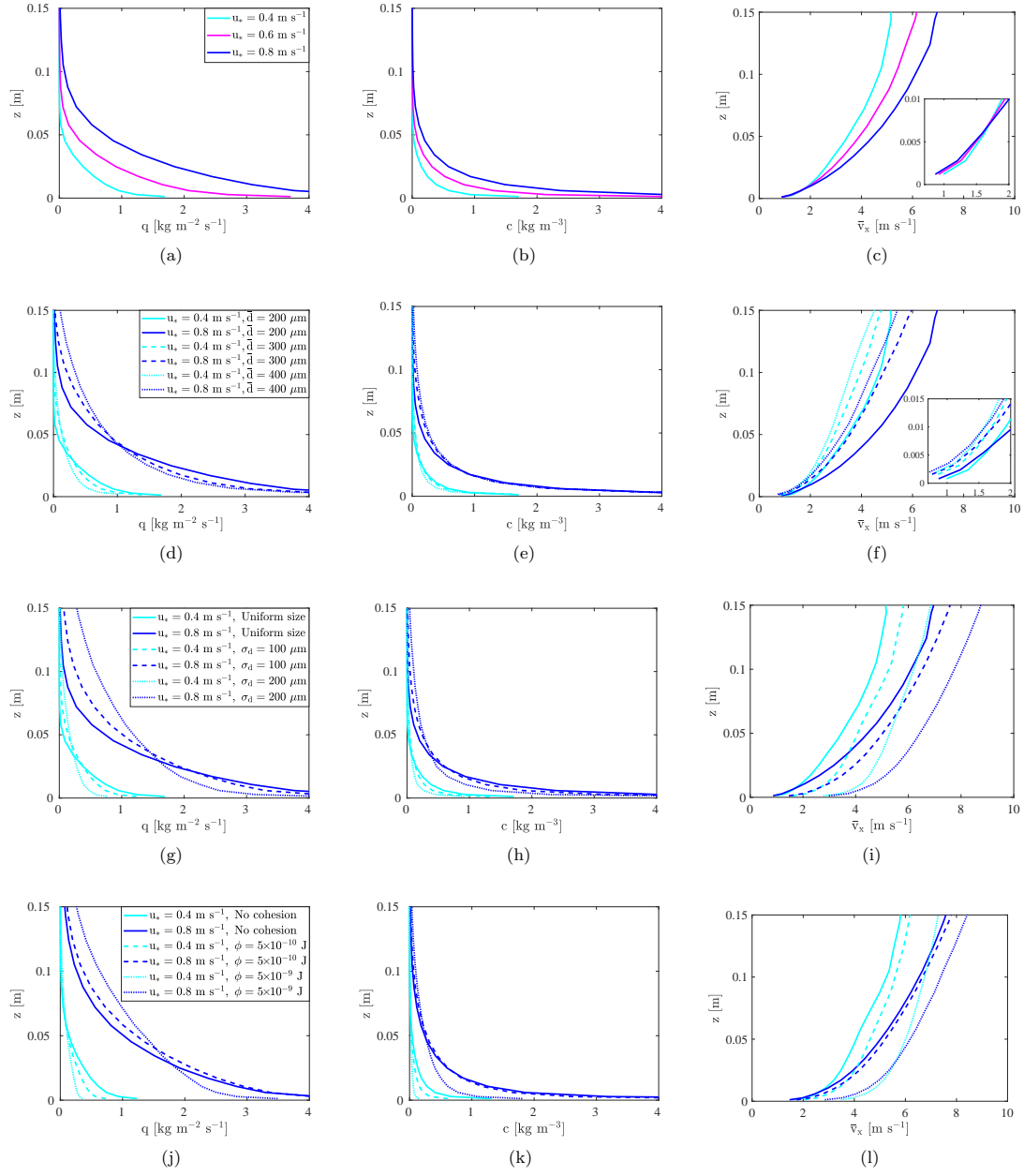
Figure 4.2: Vertical profiles of particle mass flux, concentration and streamwise velocity obtained with simulations S1 (a-c), S2 (d-f), S3 (g-i) and S4 (j-l). In (d-i) and (j-l) results from simulations S1 and S3 are presented for comparison, respectively. All values are obtained from surface averages and time averages over the last 100 s of each simulation. The insets in (c) and (f) are a zoom-in to the near-surface region.
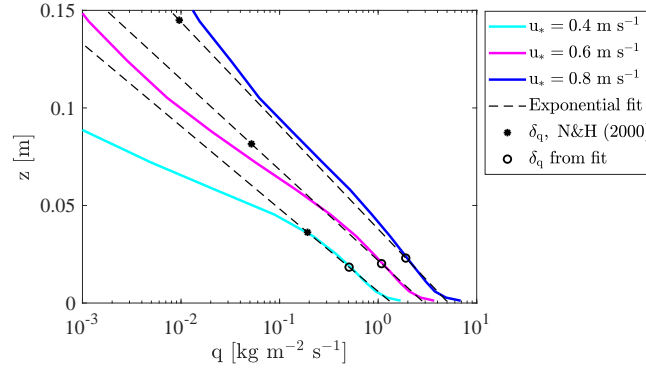
Figure 4.3: Vertical profile of particle mass flux obtained with simulations S1 and fit to exponential decay. The decay height, $\delta_q$, computed from the exponential fit and from the expression proposed by Nishimura and Hunt (2000) (N&H) is indicated at each exponential curve.

near-surface wind speed is also approximately invariant with regards to the same quantity. High above the surface, the wind speed increases as $u_*$ rises. Hence, a near-surface wind speed approximately invariant with $u_*$ is only obtained if a focus point is visible close to the surface, below which the wind speed decreases as $u_*$ increases.

Some of the snow saltation models implemented in atmospheric models (Pomeroy & Gray, 1990; Vionnet et al., 2014) assume that the mean particle streamwise velocity in the saltation layer is invariant with $u_*$. In addition, they assume that the saltation layer height varies from 1 to 5 cm (or from 2 to 6 cm) for $u_*$ varying from 0.4 to 0.8 m s$^{-1}$, respectively. Indeed, our results show that the mean particle speed does not vary with $u_*$ in the first centimeter above the ground (inset in Figure 4.2c). However, in agreement with the measurements of Nishimura et al. (2014), this is not considered representative of the whole saltation layer.

The surface friction velocity, $u_{*,s}$, as a function of time is presented in Figure 4.4. The fluid threshold friction velocity, $u_{*,ft}$, is also plotted as a reference. $u_{*,s}$ strongly decreases immediately after the start of surface erosion ($t = 25$ s). It tends to an equilibrium value, which we denote the equilibrium surface friction velocity, $u_{*,eq}$. A small reduction of $u_{*,eq}$ is obtained when the friction velocity outside the saltation layer, $u_*$, increases (inset in Figure 4.4). As discussed in section 2.2.1, these results are in agreement with the simulations of Niiya and Nishimura (2022). The numerical model COMSALT proposed by Kok and Renno (2009) also predicts this trend for a bed with uniform grain size (Kok et al., 2012). However, they predicted a stronger reduction than that presented in the inset in Figure 4.4. Therefore, the results presented do not deviate significantly from the assumption that the surface friction velocity during saltation is invariant with respect to $u_*$ (Owen, 1964).

In the work of Kok and Renno (2009), the impact threshold friction velocity, $u_{*,it}$ (i.e., the minimum friction velocity, $u_*$, at which saltation can be sustained after its onset (Bagnold, 1941)), is assumed equal to the minimum value of $u_*$ that satisfies the steady-state equation. In their model, the equilibrium surface friction velocity, $u_{*,eq}$, tends to the computed $u_{*,it}$
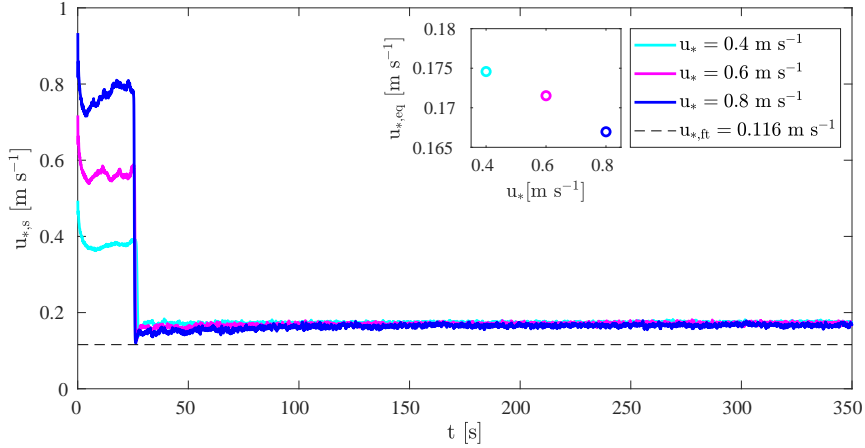
Figure 4.4: Surface friction velocity obtained with simulations S1. The fluid threshold friction velocity is also presented as a reference. In these simulations, saltation is allowed to develop after the first 25 seconds. The equilibrium surface friction velocity is presented in the inset.

as $u_*$ decreases (Kok et al., 2012). Taking into account these results, a simplified approach is followed in this work and $u_{*,it}$ is given by the value of $u_{*,eq}$ obtained when $u_*$ is set to $0.4$ m s$^{-1}$ (the minimum friction velocity common to all simulation groups). This approach is considered appropriate taking into account the small variation of $u_{*,eq}$ with $u_*$ obtained for most simulations. The impact threshold and the challenges associated to its calculation will be discussed in more detail in chapter 5.

The mass of particles aloft per unit surface area varies with time, as presented in Figure 4.5. The vertical mass flux of particles leaving the surface either through aerodynamic entrainment or splash and the vertical mass flux of particles deposited due to failure of rebound are also presented. The results were obtained for $u_* = 0.4$ m s$^{-1}$. A longer simulation time of 600 s was considered in this case to better illustrate the steady-state regime. The evolution shown in the first 350 s is representative of all the simulations performed. At $t = 25$ s, saltation starts due to aerodynamic entrainment. A sudden increase in the mass of particles aloft is observed, which is consistent with the strong decrease in surface friction velocity presented in Figure 4.4. The overshoot in particle mass is justified by the surge in the vertical mass flux of particles entering saltation via splash, that overcomes the vertical mass flux of particles leaving the saltation layer through deposition (Figure 4.5b). The imbalance between the vertical mass flux of splash and deposition drives the variation of mass of particles aloft. When saltation reaches steady-state, a dynamic equilibrium between the vertical mass flux of splash and deposition is obtained. Aerodynamic entrainment is much smaller than splash: the vertical mass flux reaches a maximum at saltation onset and then decreases to a steady-state value, which is one order of magnitude lower than the vertical mass flux of splash and deposition. In the simulations performed, aerodynamic entrainment occurs during steady-state saltation because the surface friction velocity is greater than the specified fluid threshold friction velocity (Figure 4.4). Taking into account the relatively small contribution of aerodynamic

(a) Complete time-evolution

(b) First seconds after saltation onset
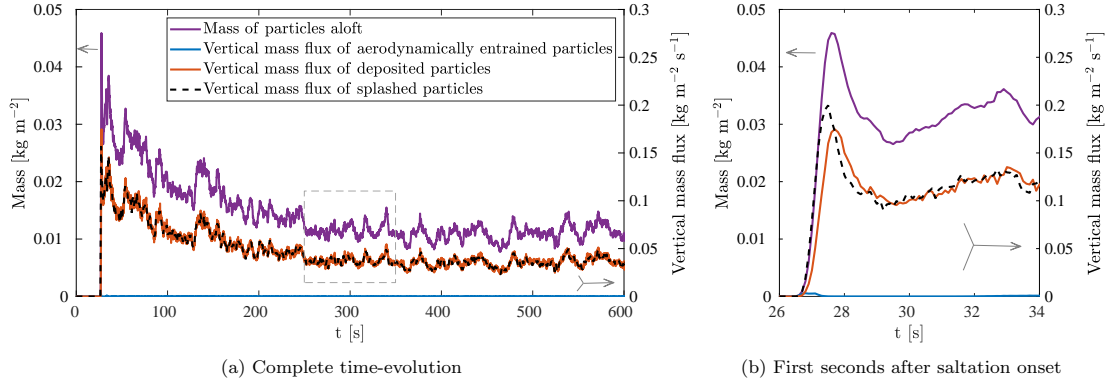
Figure 4.5: Time-evolution of the mass of particles aloft per unit area (purple line). The time-evolution of the vertical mass flux of particles leaving the surface either through aerodynamic entrainment or splash and the vertical mass flux of particles deposited are presented in blue, dashed black and orange, respectively. Results obtained from simulation S1 with $u_* = 0.4 \text{ m s}^{-1}$. The arrows indicate the y-axis corresponding to each curve. The rectangle encloses the time interval used to compute the time-averaged quantities.

entrainment to the mass of particles aloft, the correct assessment of the fluid threshold is expected to have a negligible effect on steady-state saltation for friction velocities significantly greater than the fluid threshold friction velocity. These results are in agreement with the notion that steady-state saltation is dominated by splash and that an equilibrium between splash and failure of rebound should be attained (Kok et al., 2012; Paterna et al., 2017). However, these conclusions are challenged in chapter 5, when discussing friction velocities smaller than $0.4 \text{ m s}^{-1}$.

The time-averaged transport rate and the corresponding standard deviation are presented in Figure 4.6. In Figure 4.6a, the fit between the mean values and a quadratic function is presented, as well as between the mean values and a cubic function. Moreover, the transport rate estimated from fitting the vertical profile of particle mass flux to an exponential function is also shown. In Figure 4.6b, the results are compared to saltation models proposed by several authors (Bagnold, 1941; Doorschot & Lehning, 2002; Durán et al., 2011; Pomeroy & Gray, 1990; Sørensen, 2004). The results from Doorschot and Lehning (2002) were obtained from the numerical algorithm proposed by the authors. The remaining curves are computed from the equations presented in Table 4.2.

As described in section 2.2, these equations are obtained from the balance of horizontal momentum applied to the saltating particles (equation 2.1) and considering different assumptions regarding the evolution of $\tau_s$, $\langle \Delta v_{x,s} \rangle$ and $\langle l_p \rangle$. Following Owen's hypothesis (Owen, 1964), the impact threshold friction velocity, $u_{*,it}$ is used as a proxy for the surface friction velocity, $u_{*,s}$. In large-scale atmospheric models, the fluid threshold friction velocity, $u_{*,ft}$, is used instead (Amory et al., 2021; Sharma et al., 2023; Vionnet et al., 2017). Even though there is no full consensus on the validity of either of these hypothesis and their implications on saltation dynamics (see section 2.2.1), the fact that equation 2.1 yields $Q = 0$ when $u_*$ equals $u_{*,s}$ favours the use of these simplifying assumptions. The quadratic growth of $Q$ with $u_*$ is

49
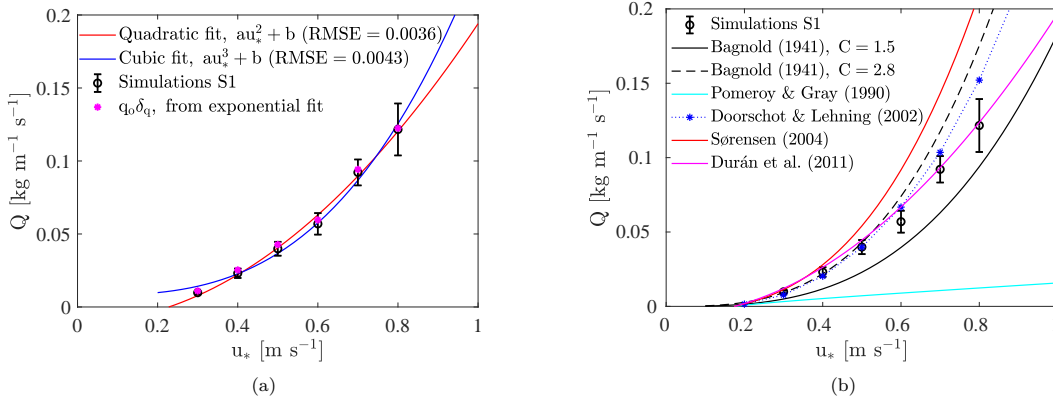
Figure 4.6: Transport rate obtained with simulations S1. The error bar is twice the standard deviation of the results. (a) Fit of simulation results to quadratic and cubic functions (RMSE is the root mean square error of the fit); comparison with the product $q_o\delta_q$ obtained from the exponential fit of the particle mass flux profile. (b) Comparison with saltation models.

predicted theoretically when both the particle velocity near the surface (and, consequently, $\Delta v_{x,s}$) and the average hop length are considered invariant with respect to $u_*$ (Durán et al., 2011; Ungar & Haff, 1987). The increase of $Q$ with $u_*^3$ was early proposed by Bagnold (1941) based on the assumption that the ratio $\langle l_p \rangle / \langle \Delta v_{x,s} \rangle$ is proportional to $u_*$. It was also obtained by Sørensen (1991, 2004) by assuming that the particle velocity near the surface is invariant with $u_*$ and that $\langle l_p \rangle$ increases linearly with $u_*$.

In Figure 4.6a, a good agreement is obtained for both polynomial functions, although the quadratic fit is slightly better (root mean square error, RMSE, equal to 0.0036 instead of 0.0043). In fact, for the range of studied friction velocities, small differences between the two functions are obtained. In addition, a good agreement is seen between the transport rate and the product $q_o\delta_q$ estimated from fitting the particle mass flux profile to an exponential function (Figure 4.3). This agreement underlines the importance of an accurate representation of the near-surface mass flux profile. Moreover, it reveals that the upper region of the saltation layer has a minor contribution to the vertically integrated mass flux.

In Figure 4.6b, the comparison between simulation results and saltation models is made by assuming an impact threshold friction velocity of $0.175\ \mathrm{m\ s^{-1}}$ (the value of $u_{*,eq}$ obtained for $u_* = 0.4\ \mathrm{m\ s^{-1}}$, as previously discussed). In the models proposed by Pomeroy and Gray (1990), Sørensen (2004) and Durán et al. (2011), the impact threshold friction velocity is a parameter in the transport rate equations which characterizes the erodible bed (Table 4.2). For friction velocities lower than $0.6\ \mathrm{m\ s^{-1}}$, a good agreement is seen between simulation results and the saltation model proposed by Doorschot and Lehning (2002). At higher friction velocities, the model proposed by Doorschot and Lehning (2002) predicts greater values for $Q$ and a better agreement is obtained with the expression proposed by Durán et al. (2011). $Q_{Dur}$ scales with $u_*^2$, which is supported by the current simulation results. However, this equation is highly sensitive to the value of the impact threshold friction velocity and the observed agreement

Table 4.2: Saltation models for the transport rate, $Q$.

| Transport rate [kg m$^{-1}$ s$^{-1}$] | Constant parameters | References |
|---|---|---|
| $Q_{Bag} = C\sqrt{\dfrac{\bar{d}}{d_R}}\dfrac{\rho_f}{g}u_*^3$ | $C = 1.5$ (uniform grains) $C = 2.8$ (highly non-uniform grains) | Bagnold (1941) |
| $Q_{P\&G} = C\dfrac{\rho_f}{g}u_{*,it}u_*\left(1 - \dfrac{u_{*,it}^2}{u_*^2}\right)$ | $C = 0.68$ | Pomeroy and Gray (1990) |
| $Q_{S04} = \dfrac{\rho_f}{g}u_*^3\left(1 - \dfrac{u_{*,it}^2}{u_*^2}\right)\left(\alpha + \beta\dfrac{u_{*,it}^2}{u_*^2} + \gamma\dfrac{u_{*,it}}{u_*}\right)$ | $\alpha = 2.6, \beta = 2.5, \gamma = 2.0$ [1] | Sørensen (2004) |
| $Q_{Dur} = C\dfrac{\rho_f}{g}u_{*,it}u_*^2\left(1 - \dfrac{u_{*,it}^2}{u_*^2}\right)$ | $C = 8.5$ [2] | Durán et al. (2011) |

$d_R$ is a reference diameter, $d_R = 250 \times 10^{-6}$ m.

[1] Constant parameters proposed by Vionnet et al. (2014) from fitting the equation to the experimental measurements of Nishimura and Hunt (2000).

[2] $C$ estimated from Figure 27 in Durán et al. (2011), assuming a packing fraction of the bed, $\phi_b$, equal to 0.95.

is greatly compromised for different values of $u_{*,it}$. Bagnold (1941) and Sørensen (2004) proposed expressions for $Q$ proportional to $u_*^3$. When using the coefficients proposed by Vionnet et al. (2014), a greater mass flux is obtained with Sørensen's expression in comparison with the simulation results. Vionnet et al. (2014) estimated those coefficients from fitting $Q_{S04}$ to the experimental measurements of Nishimura and Hunt (2000). Conversely, the expression proposed by Bagnold (1941) to describe saltation over uniform grains ($C = 1.5$) predicts lower values for $Q$. For friction velocities lower than 0.6 m s$^{-1}$, the simulation results agree well with the model proposed by Bagnold (1941) if the constant parameter $C$ is increased to 2.8. However, the curve obtained with $C = 2.8$ is only expected to describe saltation over a bed of mixed-sized grains. The expression proposed by Pomeroy and Gray (1990) underestimates the transport rate in comparison with the remaining models and the simulation results. This is partly justified by the authors assumption of a relatively shallow saltation layer (saltation layer height varying from 0.7 to 5 cm for $u_*$ varying from 0.3 to 0.8 m s$^{-1}$). However, even by adjusting the height of integration from 15 cm to the proposed values, the transport rate obtained with the current numerical model is significantly greater that the evolution proposed by Pomeroy and Gray (1990). Hence, the deviation between $Q_{P\&G}$ and the remaining models and simulation results is mainly related to the erroneous scaling of the transport rate with $u_*$.

### 4.2.2 The effect of mean grain diameter

In this section, we continue the analysis of saltation over a bed of equally-sized grains. The effect of grain size is studied by comparing the results presented in the previous section (S1, $\bar{d} = 200$ $\mu$m) with those from simulations S2, obtained for different grain sizes.

The vertical profiles of particle mass flux, concentration and mean streamwise velocity obtained for grain diameters ranging from 200 to 400 $\mu$m are presented in Figures 4.2d-f. It can

be observed that particle streamwise velocity decreases when the grain size increases (Figure 4.2f). This is due to the fact that aerodynamic drag applied to the saltating particles increases approximately with $d^2$, but particle mass increases with $d^3$. Hence, the ability of the flow to accelerate the saltating grains reduces with the increase in particle mass. The near-surface particle velocity also decreases with the grain diameter (inset in Figure 4.2f). Although the near-surface particle velocity does not vary significantly with $u_*$, it clearly varies with the grain size.

As the grain size increases, the particle mass flux decreases near the surface and increases at higher elevations of the saltation layer (Figure 4.2d). Near the surface, this trend is justified by the decrease in particle streamwise velocity as $\bar{d}$ increases (Figure 4.2f). Above approximately 4 cm, the increase in particle mass flux as the grain size increases is due to the rise in particle concentration (Figure 4.2e), which is related to both an increase in particle mass and the number of particles aloft. The vertical profiles of particle mass flux obtained for $u_* = 0.4$ m s$^{-1}$ are also presented in logarithmic scale in Figure 4.7a. The results obtained with $\bar{d} = 100$ $\mu$m are added for comparison. An exponential decay along the saltation layer is clear for the greater grain sizes ($\bar{d}$ between 200 and 400 $\mu$m), which is in agreement with field measurements (Martin & Kok, 2017) as previously discussed in section 4.2.1. The vertical profile obtained with the smallest grain size ($\bar{d} = 100$ $\mu$m) differs significantly from the others. A similar trend inside the saltation layer is visible up to 1 cm height. However, at greater heights, the profile assumes a different shape suggesting transition from saltation to suspension. In fact, for the smallest grain size, particles can be observed up to the top of the domain, while for greater grain sizes, aeolian transport seems to occur via saltation only as the mass flux ceases at approximately 14 cm height.

The transport rate is presented in Figure 4.8a along with the expression proposed by Bagnold (1941) and the numerical results from Doorschot and Lehning (2002) for varying mean grain diameters and friction velocities. Bagnold's expression establishes that $Q$ is proportional to
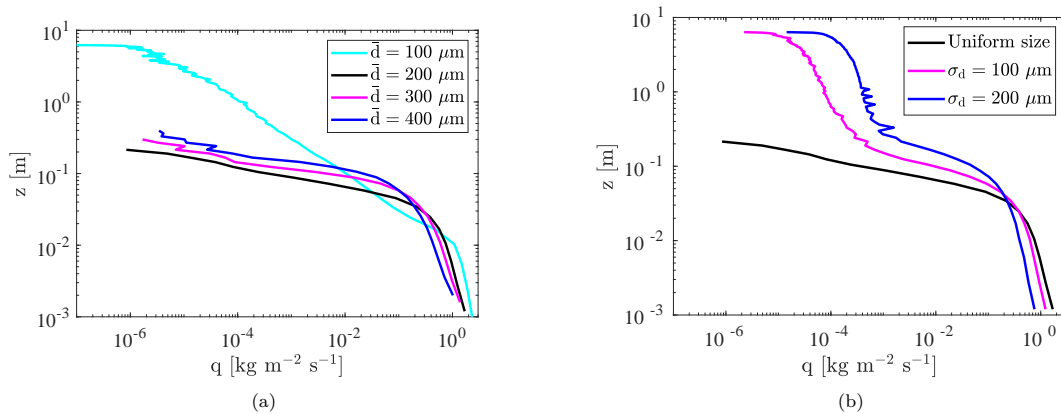


Figure 4.7: Vertical profiles of particle mass flux obtained with simulations S2 (a) and S3 (b) for $u_* = 0.4$ m s$^{-1}$. Results from simulations S1 are presented for comparison.
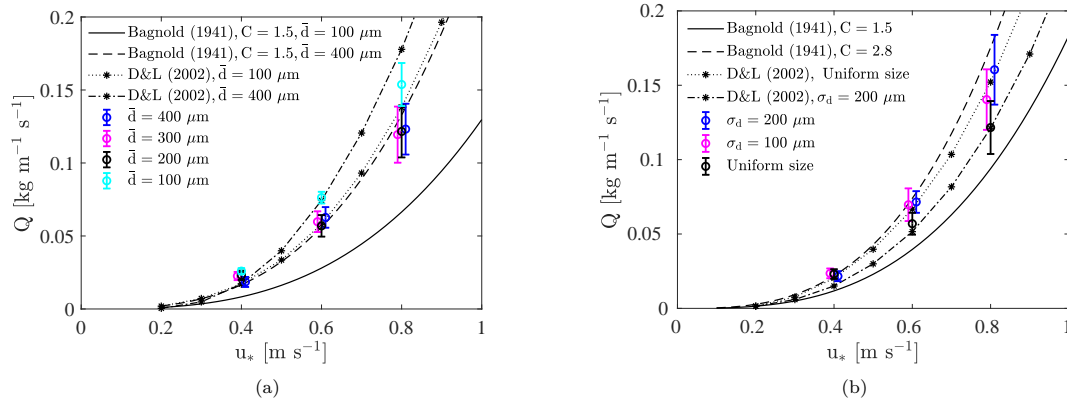
Figure 4.8: Transport rate obtained with simulations S2 (a) and S3 (b) for $u_*$ equal to 0.4, 0.6 and 0.8 m s$^{-1}$. Results from simulations S1 obtained with the same $u_*$ are also presented for comparison. To improve readability, some data points are slightly shifted in the $u_*$ axis. The error bar is twice the standard deviation of the results. The curves are obtained from Bagnold's model ($Q_{Bag}$ in Table 4.2) and from the numerical model proposed by Doorschot and Lehning (2002) (D&L). In (a), the curves are computed considering a uniform bed characterized by different grain diameters. In (b), both a uniform and a mixed-sized bed with a mean grain diameter of 200 $\mu$m are considered.

$\bar{d}^{\frac{1}{2}}$, following his wind tunnel experiments performed with uniform sand beds characterized by mean diameters ranging from 100 $\mu$m to 1 mm. The numerical model of Doorschot and Lehning (2002) also predicts an increase in the transport rate with the grain diameter. In contrast, a negligible variation is obtained with our model for grain diameters ranging from 200 to 400 $\mu$m: the reduction in mass flux near the surface and its increase at higher elevations for increasingly bigger grains (Figure 4.2d) counterbalance each other. In fact, other saltation models do not predict an explicit variation of $Q$ with the particle mean diameter (e.g., Durán et al., 2011; Sørensen, 2004). In opposition to Bagnold's experiments, the wind tunnel measurements carried out by Dong et al. (2003) revealed a reduction in the transport rate with the grain diameter. However, the comparison between sand beds is performed considering the same wind speed at a given reference height. Hence, it is observed that for the same wind speed at the chosen reference height, the transport rate decreases as the grain size increases. In the simulations performed, the imposed friction velocity is kept constant when varying the grain size, which implies different velocities at a given reference height, depending on the mass flux of saltating particles and the respective momentum transfer. The negligible variation of the transport rate with $\bar{d}$ obtained with our model goes along with an increase in the wind speed at all heights as the grain size increases. When analyzing the experiments of Dong et al. (2003) performed with different grain sizes but yielding similar transport rates, a greater wind speed is also obtained for greater grain sizes.

When considering a uniform bed with grains of 100 $\mu$m, a greater transport rate is obtained. However, as previously discussed, particles between 1 and 15 cm height might not be in saltation but rather in suspension. When modeling particles smaller than 200 $\mu$m, a rigorous definition of the saltation layer height is needed to fully assess the impact of the mean diameter on the transport rate in saltation. Different criteria have been proposed to define the height of
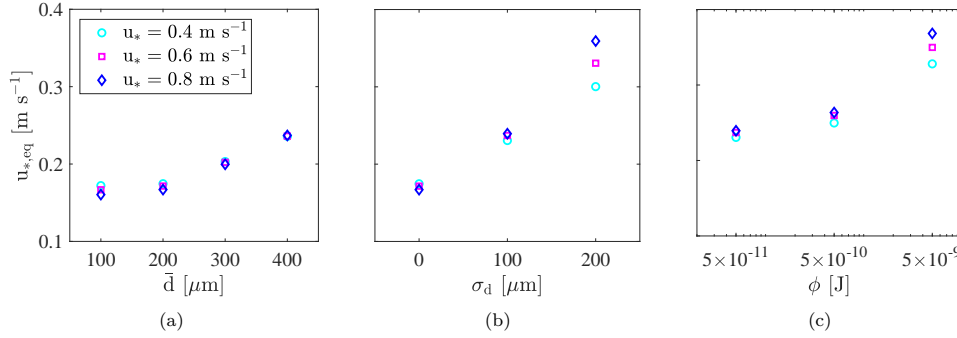
Figure 4.9: Equilibrium surface friction velocity obtained with simulations S2 (a), S3 (b) and S4 (c). In (a) and (b), results from simulations S1 are presented for comparison. In (c), results from simulations S3 are presented for comparison.

the saltation layer. They are either based on the mean height of particle trajectories (Owen, 1964), the amount of momentum transported from the fluid to the particles (Dupont et al., 2013), or the exponential fit of the mass flux profile (Martin & Kok, 2017). Due to the lack of consensus in this matter, a precise definition of the saltation layer height is avoided in this work.

The equilibrium surface friction velocity varies considerably with the mean grain size. In Figure 4.9a, an increase of $u_{*,eq}$ is observed when $\bar{d}$ increases for values greater than 200 $\mu m$, which is consistent with the results of Kok and Renno (2009). For a given $u_*$, the total momentum transfer from the fluid to the particles decreases for greater grain diameters. This is partly due to a smaller number of particles aloft, which overcomes the increase in drag applied on each grain. These results are aligned with the idea that the surface friction velocity is invariant with respect to the friction velocity outside the saltation layer, but a function of the bed characteristics (Owen, 1964).

### 4.2.3   The effect of mixed-sized grains

In order to model saltation over a bed of mixed-sized grains, the size distribution of surface grains is described by a lognormal distribution. In this section, the results from simulations S3, obtained with different standard deviations of the grain diameter, are presented and compared with those from simulations S1, obtained with a uniform grain size.

The vertical profiles of particle mass flux, concentration and mean streamwise velocity are presented in Figures 4.2g-i. Grain size heterogeneity leads to a greater mean particle streamwise velocity, both near the surface and at higher elevations (Figure 4.2i). This is due to an increase in the number of smaller particles aloft, which are easily accelerated by the fluid flow. Similarly to Figure 4.2f (simulations S2), the variation of particle speed close to the surface with $u_*$ is negligible; however, a clear variation with the bed characteristics is observed. The effect of the bed size distribution on the particle streamwise velocity profile is less significant

when a mass-weighted average is considered. This is due to the reduced contribution of the smaller grains to the average profile.

Figures 4.2g and 4.2h show that grain size heterogeneity decreases the particle mass flux and concentration close to the surface, but leads to greater values at higher elevations of the saltation layer. The vertical profiles of particle mass flux obtained for $u_* = 0.4$ m s$^{-1}$ are presented in logarithmic scale in Figure 4.7b. As expected, close to the surface, an exponential decay across the saltation layer is observed. At higher elevations, a cloud of suspended grains forms above the saltation layer of mixed-sized beds and a second distinct exponential decay of the mass flux along the height is observed. The particle concentration profile follows a similar trend as the mass flux profile. As suggested by Kawamura (1951), the particle concentration is well approximated by a power law between approximately 0.4 and 3 m height. Above 3 m height, the strong decrease in particle mass flux and concentration is due to the loss of particles through the top boundary. The transition from saltation to suspension occurs between 10 and 20 cm height, approximately, and is characterized by the change in gradient of the mass flux profiles. This trend was previously observed in field measurements (Gordon et al., 2009) and other numerical models (e.g., Nemoto & Nishimura, 2004).

The probability mass function (PMF) of particle size at different heights is presented in Figure 4.10 for $u_* = 0.4$ m s$^{-1}$ and both size distributions ($\sigma_d$ of 100 and 200 $\mu$m). The PMF of particle size at the bed is also presented for comparison (the left tail of the distribution is not obtained, as a minimum grain size of 50 $\mu$m is specified in the simulations). Below approximately 3 cm height, the size distribution of particles aloft is reasonably well approximated by a lognormal distribution. It is similar to the PMF at the bed, but skewed towards smaller grain sizes. From 5 to 10 cm height, a bi-lognormal distribution is visible in both simulations. In this region, for progressively greater heights, the probability of smaller grains increases and the probability of bigger grains decreases. Finally, above approximately 14 cm, a new lognormal distribution arises, characterized by grains smaller than 100 $\mu$m. The presented variation of particle size
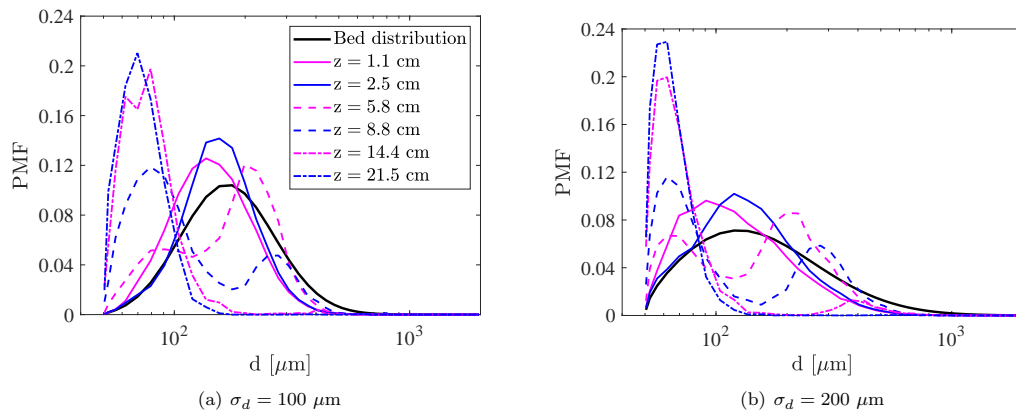


Figure 4.10: Probability mass function (PMF) of particle size at the bed and at different heights obtained from simulations S3 considering $u_* = 0.4$ m s$^{-1}$.

distribution with height agrees well with the results of Nemoto and Nishimura (2004) and is related to the saltation-suspension transition observed in Figure 4.7b. During snow transport events, particle sublimation can change the size distribution by reducing the size of particles aloft. This modifies the equilibrium saltation state and enhances the transport of particles in suspension.

Figure 4.10b shows that a wider lognormal bed size distribution leads to smaller grain sizes in the first centimeters above the surface. Smaller grains and less particles aloft justify the decrease in mass flux close to the surface observed in Figure 4.7b. Moreover, the fraction of grains within the range 200 to 500 $\mu$m present between 8 and 15 cm height is greater. Considering that these particles are transported in saltation, this is in agreement with the increase in saltation layer height observed in Figure 4.7b.

The transport rate is presented in Figure 4.8b. The simulation results are compared with Bagnold's model, considering different values for the parameter $C$ (Bagnold, 1941), and with the results of the numerical model proposed by Doorschot and Lehning (2002). In the latter, particle size is assumed uniform ($\bar{d} = 200$ $\mu$m) or defined by a lognormal distribution ($\bar{d} =$ 200 $\mu$m, $\sigma_d = 200$ $\mu$m). In general, the transport rate obtained with the current model increases with bed heterogeneity. This trend is also predicted by Bagnold (1941). However, it contrasts with the evolution obtained with the model of Doorschot and Lehning (2002), in which $Q$ decreases when the bed heterogeneity increases. The effect of bed size distribution on the transport rate underlines the importance of correctly describing particle size when estimating snow saltation mass flux. According to the simulation results, this is particularly relevant when $u_*$ is greater than 0.4 m s$^{-1}$. Even though a rigorous definition of the saltation layer height is not taken in this work, similar trends are obtained when the integration height is limited to the first 10 cm. Moreover, the effect of bed heterogeneity on the computed transport rate is even more significant if the suspension layer is taken into account. The transport rate obtained for a uniform bed of grains with 100 $\mu$m in diameter is closer to the values obtained for the studied mixed-sized beds, compared to the other uniform beds with larger grains (Figure 4.8a). However, over the uniform bed with grains of 100 $\mu$m, particles above 1 cm height seem to be transported in suspension (Figure 4.7a). Taking also into account that an increase in the mean particle diameter from 200 to 400 $\mu$m leads to a negligible variation of $Q$ (Figure 4.8a), it is in general not possible to correctly model saltation over a mixed-size bed considering a representative diameter and equally-sized grains.

An increase in bed heterogeneity also leads to an increase in the equilibrium surface friction velocity, $u_{*,eq}$ (Figure 4.9b). In contrast with the simulations performed over equally-sized grains, $u_{*,eq}$ slightly increases with $u_*$. This trend is specially visible for the results obtained with $\sigma_d = 200$ $\mu$m. For a given $u_*$, the total exchange of momentum from the fluid to the particles decreases for greater standard deviations of the size distribution. Taking into account that the drag applied on each grain is approximately proportional to $d^2$ and that the number of particles aloft does not vary in a monotonous way with $\sigma_d$, the decrease in the momentum exchange is explained by the presence of particles with diameters smaller than the mean value

($\bar{d} = 200 \; \mu$m).

### 4.2.4 The effect of interparticle cohesion

We complete the analysis of mixed-sized bed saltation by studying the effect of interparticle cohesion. In this section, the results obtained with simulations S4 are presented. A bed of mixed-sized grains characterized by a lognormal distribution with $\bar{d} = 200 \; \mu$m and $\sigma_d = 100 \; \mu$m is considered. The results are compared with those from simulation S3, that were performed with the same particle size distribution but neglecting interparticle cohesion.

The vertical profiles of particle mass flux, concentration and mean streamwise velocity are presented in Figures 4.2j-l. As cohesion energy increases, particle concentration decreases significantly close to the surface and increases slightly at higher regions of the saltation layer (Figure 4.2k). Particle mean streamwise velocity increases with cohesion energy at all heights (Figure 4.2l). As expected, close to the surface, a negligible variation of particle streamwise velocity is obtained for different $u_*$; however, a clear variation with interparticle cohesion is seen. As the ejection velocity increases, the maximum height attained by the saltating particles increases as well. This justifies the observed larger particle concentration at higher elevations. Particle mass flux is given by the product of particle concentration and streamwise velocity. It decreases close to the surface due to a strong reduction in the number of particles and increases at higher regions of the saltation layer due to the rise of both the number of particles aloft and the particle streamwise velocity (Figure 4.2j).

The equilibrium surface friction velocity, $u_{*,eq}$, is presented in Figure 4.9c. It is expected to vary with the bed type, and therefore, with the strength of the interparticle bonds. In fact, $u_{*,eq}$ increases with the cohesion energy, which was also obtained by Comola, Gaume, et al. (2019).

Cohesion energy has a direct effect on the number of ejected grains computed from energy conservation, $N_E$ (see equation 3.8a). If $N_E$ becomes smaller than $N_M$, the number of ejected grains is restricted by energy conservation and it decreases for increasing values of $\phi$. Hence, for the same impact velocity and impacting grain diameter, the number of splashed grains reduces with cohesion energy (Comola & Lehning, 2017). Our results suggest that this leads to a global decrease of particles aloft (Figure 4.2k). As a result, for greater values of cohesion energy, the total momentum transfer from the fluid to the particles is smaller (Figure 4.9c), as well as the consequent decrease in streamwise wind speed. This leads to a general increase in particle speed (Figure 4.2l). The initial velocity at which the splashed grains are ejected from the bed does not vary directly with interparticle cohesion (see distribution characteristics presented in Table 3.1). However, greater impact velocities lead to higher ejection velocities.

The transport rate is presented in Figure 4.11. The results obtained with the saltation models proposed by Pomeroy and Gray (1990), Doorschot and Lehning (2002) and Sørensen (2004) are also presented for comparison. These models are currently used in atmospheric and snow models, such as RACMO (Lenaerts et al., 2012), MAR (Amory et al., 2015, 2021), Alpine3D
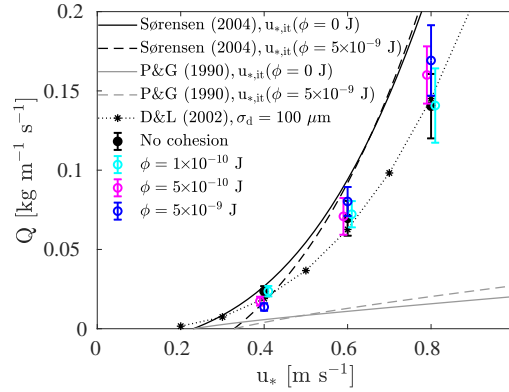
Figure 4.11: Transport rate obtained with simulations S4 for $u_*$ equal to 0.4, 0.6 and 0.8 m s$^{-1}$. Results from simulations S3 obtained with the same size distribution and $u_*$ are also presented for comparison. To improve readability, some data points are slightly shifted in the $u_*$ axis. The error bar is twice the standard deviation of the results. The expressions proposed by Sørensen (2004) and Pomeroy and Gray (1990) (P&G) are plotted for comparison considering different values of the impact threshold friction velocity. The results from Doorschot and Lehning (2002) (D&L) are obtained for a bed characterized by a lognormal distribution with $\bar{d} = 200 \, \mu$m and $\sigma_d = 100 \, \mu$m.

(Lehning et al., 2008), Meso-NH (Vionnet et al., 2014) and CRYOWRF (Sharma et al., 2023), to estimate snow saltation mass flux. The expressions proposed by Pomeroy and Gray (1990) and Sørensen (2004) are plotted for two limiting values of the impact threshold friction velocity: obtained with simulation S3, $\sigma_d = 100 \, \mu$m (non-cohesive bed) and with simulation S4, $\phi = 5 \times 10^{-9}$ J. As previously explained, in this work, the impact threshold friction velocity is assumed equal to the equilibrium surface friction velocity at the lowest value of $u_*$ that was studied ($u_* = 0.4$ m s$^{-1}$). The results obtained with the model of Doorschot and Lehning (2002) are derived considering a lognormal bed size distribution with $\bar{d} = 200 \, \mu$m and $\sigma_d = 100 \, \mu$m.

The simulation results indicate that $Q$ varies significantly with cohesion energy. In general, it decreases with $\phi$ for lower friction velocities and increases with $\phi$ for greater values of $u_*$. This is due to the reduction of particle mass flux close to the surface and to its increase at higher elevations as cohesion energy increases (Figure 4.2j). At low friction velocities ($u_* = 0.4$ m s$^{-1}$), the reduction of particle mass flux close to the surface (due to the decrease in particle concentration) prevails, while at greater $u_*$, the rise in mass flux at higher elevations (due to the increase in particle velocity) becomes more significant, leading to a global growth of the transport rate. Naturally, for very high values of cohesion energy, for which particle ejection is highly compromised, the reduction in particle concentration is expected to prevail at all friction velocities, leading to a reduction in the transport rate.

A better agreement between the expression proposed by Sørensen (2004), using the parameters proposed by Vionnet et al. (2014), and the simulation results is obtained when interparticle cohesion and a lognormal size distribution are considered. This is, when considering a more realistic snow bed. Nonetheless, greater values for $Q$ are predicted with $Q_{S04}$. An overestimation of the transport rate in saltation is consistent with the overestimation of

blowing snow particles obtained by Vionnet et al. (2014, 2017). The effect of the impact threshold friction velocity on $Q_{S04}$ is mainly visible at lower friction velocities. At $u_* = 0.4$ m s$^{-1}$, the adjustment of the impact threshold friction velocity improves the agreement between model and simulation results obtained with different values for cohesion energy. The results obtained with the numerical model of Doorschot and Lehning (2002) agree well with the simulation results obtained with mixed-sized and cohesionless grains or $\phi = 10^{-10}$ J, over the whole range of the studied friction velocities. Even though a good agreement is also obtained over a bed of uniform grains for $u_* < 0.6$ m s$^{-1}$ (Figure 4.6b), the effect of mean grain diameter and bed heterogeneity on the transport rate predicted by Doorschot and Lehning (2002) is not consistent with the evolution obtained by the present model (Figure 4.8). The expression proposed by Pomeroy and Gray (1990) considerably underestimates the transport rate in comparison with the simulation results and remaining models, independently of the assumed values for the impact threshold friction velocity. The underestimation of the saltation mass flux might be one of the causes for the underestimation of the blowing snow mass flux obtained by Amory et al. (2015).

In the blowing snow model proposed by Amory et al. (2021), the transport rate in saltation is also computed with the expression of Pomeroy and Gray (1990). However, more reasonable estimates of the blowing snow mass flux are obtained. This is mainly attributed to the improved calculation of the fluid threshold friction velocity and of snow densification induced by the occurrence of snow transport. Other aspects of the blowing snow model will also influence the particle mass flux in suspension near the surface. They are, for example, the type of lower boundary condition implemented, the turbulence diffusivity considered in the saltation-suspension transition region, and the assumed particle streamwise velocity above the saltation layer.

## 4.3 Conclusions

The modeling of snow saltation is particularly challenging due to the metamorphic nature of snow. Depending on the meteorological conditions, snow grains can have multiple shapes and sizes and form interparticle ice bonds between them. During snow transport, the interparticle bonds break and snow particles shape and size change due to fragmentation and sublimation. However, snow saltation models used in large-scale models generally neglect or oversimplify these particularities, leading to uncertainties in the estimated mass flux that are difficult to quantify. In this chapter, the LES-LSM model is used to simulate the complex particle-wind-bed interactions. This approach allows the modeling of steady-state saltation over a variety of bed types and the analysis of the effect of grain size and interparticle cohesion on saltation dynamics.

The numerical model is able to simulate the main saltation characteristics observed in previous models and experiments: the focus point in the average streamwise wind profiles, an average streamwise particle velocity close to the surface invariant with respect to the friction velocity,

the exponential decay of particle mass flux with increasing height, and the scaling of the transport rate with the square or cube of the friction velocity. Moreover, as expected, for friction velocities sufficiently greater than the fluid threshold friction velocity, the resulting steady-state is characterized by a dynamic equilibrium between splash and deposition. Over mixed-sized beds, different particle size distributions are obtained depending on the distance to the snow surface, as expected when transition from saltation to suspension occurs.

The relative importance of snow bed characteristics on saltation dynamics is analyzed by varying the particle size distribution and interparticle bond strength in a systematic way. Bed characteristics, such as grain size and interparticle cohesion, significantly influence saltation dynamics, in particular, particle velocity, surface friction velocity and transport rate. Particle velocity close to the surface is approximately invariant with respect to the friction velocity for all beds that were considered; however, it varies with the bed type. This is relevant for the development of simple saltation models, which are usually based on an assumption for the near-surface particle velocity. Nevertheless, the mean particle velocity in the saltation layer increases with the friction velocity. The average surface friction velocity during steady-state saltation, defined here as the equilibrium surface friction velocity, increases for greater values of the mean grain diameter, standard deviation of the size distribution and interparticle cohesion. The equilibrium surface friction velocity is tightly correlated with the impact threshold friction velocity, which is an important parameter to estimate saltation mass flux. Over uniform beds, a negligible variation of the transport rate with particle size is obtained for particles ranging between 200 and 400 $\mu$m. When considering a mixed-sized bed characterized by a lognormal distribution, an increase in the transport rate is seen due to an average increase in particle velocity and concentration. The results presented highlight that the transport rate over mixed-sized beds can be hardly reproduced by an equally-sized bed with a representative mean diameter - a tempting assumption in simple saltation models. The transport rate also varies with interparticle cohesion, but in a non-monotonic way: it decreases with the strength of interparticle bonds for lower friction velocities and it increases for higher friction velocities. Overall, greater values of cohesion lead to a reduction in the number of particles aloft which, at high wind speeds, is balanced by an increase in particle velocity. In general, the greater the friction velocity, the greater the effect of bed properties on saltation characteristics. High wind speed events might be rare in some regions. However, they are responsible for major modifications of the snow cover.

The agreement between simulation results and the saltation models typically used in large-scale atmospheric and snow models depends on the bed characteristics. For specific bed types, a relatively good agreement with the computed transport rate can be obtained with the models of Sørensen (2004), using the parameters proposed by Vionnet et al. (2014), and Doorschot and Lehning (2002). However, these models either consider fixed parameters, which are not adjusted according to the snow type, or predict a different variation of the transport rate with the mean grain size and bed heterogeneity. A systematic underestimation and overestimation of the transport rate is obtained with the expression proposed by Pomeroy and Gray (1990) and Sørensen (2004), respectively. This might partly justify the underestimation

and overestimation of blowing snow mass flux presented, respectively, by Amory et al. (2015) and Vionnet et al. (2014, 2017). Inaccuracies in the calculation of particle concentration at the top of the saltation layer can also be related to poor estimates of the vertical profile of particle mass flux, the averaged streamwise particle velocity and the saltation layer height. Grain size and interparticle cohesion influence all variables of interest. Therefore, improvements on snow transport models can only be reached if all referred quantities are correctly parameterized.

The work presented shows the capabilities of an LES-based model to simulate snow saltation, presents the effect of bed properties on saltation dynamics and motivates further studies in this field. It highlights some of the limitations of the snow saltation models currently employed in atmospheric and snow models and the importance of taking the snow surface characteristics into account. Without accurate estimations for the mass flux in saltation, atmospheric models will hardly deliver reasonable estimates of blowing snow mass flux and sublimation. Hence, without further developments, the effect of snow transport and sublimation on large-scale mass and energy balances is highly compromised.

# 5 The saltation dynamics and its link to snow saltation parameterizations

In this chapter, the LES-LSM model is used to investigate some scaling laws of the saltation system. The simulations are tailored to reproduce the wind tunnel measurements of Sugiura et al. (1998). The transport rate and the vertical profiles of particle mass flux and velocity are investigated, as well as the particle hop height and length during saltation. Special focus is given to the decay height and to its relation to the relative importance of aerodynamic entrainment and splash. These results are compared to the currently used parameterizations and new insights are given regarding the dynamics of snow saltation. In section 5.1, the numerical settings of the simulations are presented, the results are presented and discussed in section 5.2, and the main conclusions are summarized in section 5.3.

## 5.1  Numerical setup

The numerical setup considered in this analysis is equal to the one described in section 4.1.1 when it comes to domain size, spatial discretization, LES time step and simulation time. The remaining settings were modified in order to better reproduce the conditions reported in Sugiura et al. (1998). For instance, the particle size distribution of the granular bed is assumed normal, with a mean diameter of 360 $\mu$m and a standard deviation of 140 $\mu$m. A minimum and maximum particle diameter is imposed, equal to 30 $\mu$m and 2 mm, respectively. In the experiments of Sugiura et al. (1998), the wind tunnel was maintained at -15°C. Therefore, in the simulations, the air density and kinematic viscosity are set to the respective values at that temperature ($\rho_a$ = 1.37 kg m$^{-3}$, $\nu_a$ = 1.2×10$^{-5}$ m$^2$ s$^{-1}$). Moreover, snow sublimation is neglected. Taking into account that the snow layer was composed of preserved natural snow that was disintegrated into individual particles prior to the experiments, the effect of interparticle cohesion is neglected in the simulations. Similarly to the analysis presented in chapter 4, the remaining splash parameters are set to the values specified in Table 3.2 and the fluid threshold coefficient, $A$, is set to 0.1. In addition, the particle density is assumed equal to 917 kg m$^{-3}$, as suggested by Sugiura et al. (1998). The roughness length, $z_o$, is not reported in Sugiura et al. (1998) and a value of 10$^{-4}$ m is assumed (Clifton et al., 2006).

A set of seven simulations is performed for which the friction velocity is varied between 0.15 and 0.7 m s$^{-1}$. In order to decrease the computational time, the time step of the LSM solver is set to 10$^{-4}$ s (twice the LES time step) for the friction velocities ranging between 0.15 and 0.5 m s$^{-1}$ and to 2×10$^{-4}$ s (four times the LES time step) for the higher friction velocities. In addition, a smaller number of particles per parcel is considered in these simulations in comparison to the values used in chapter 4. This is due to the fact that the saltation dynamics is particularly sensitive to this parameter when considering friction velocities lower than 0.4 m s$^{-1}$. This parameter is less important for $u_* > 0.4$ m s$^{-1}$, but an effect can nevertheless be seen in the resultant value of $u_{*,eq}$. In this way, the number of particles per parcel is set to 2, 20 and 50 for the friction velocities equal to 0.15, 0.23 and 0.3 m s$^{-1}$, respectively, and to 200 for the higher friction velocities.

## 5.2    Results and discussion

The average vertical profiles of particle mass flux, $q$, and streamwise velocity, $\bar{v}_x$, as well as the equilibrium surface friction velocity, $u_{*,eq}$, and transport rate, $Q$, are computed as described in section 4.1.3. Similarly, the time average is performed over the last 100 s of the simulations. During this time period, negligible changes in the total mass of particles aloft was obtained and saltation was assumed to be in steady-state.

The obtained vertical profiles of particle mass flux are presented in Figure 5.1, together with the SPC measurements performed by Sugiura et al. (1998). The results obtained for friction velocities ranging from 0.15 to 0.5 m s$^{-1}$ are presented in a linear plot (Figure 5.1a) and those obtained for all simulated friction velocities are presented in a semi-logarithmic plot (Figure 5.1b). Curves fitting the mass flux profiles with equation 2.4 are also presented. It can be seen that most of the mass flux profiles follow an exponential decay in approximately the
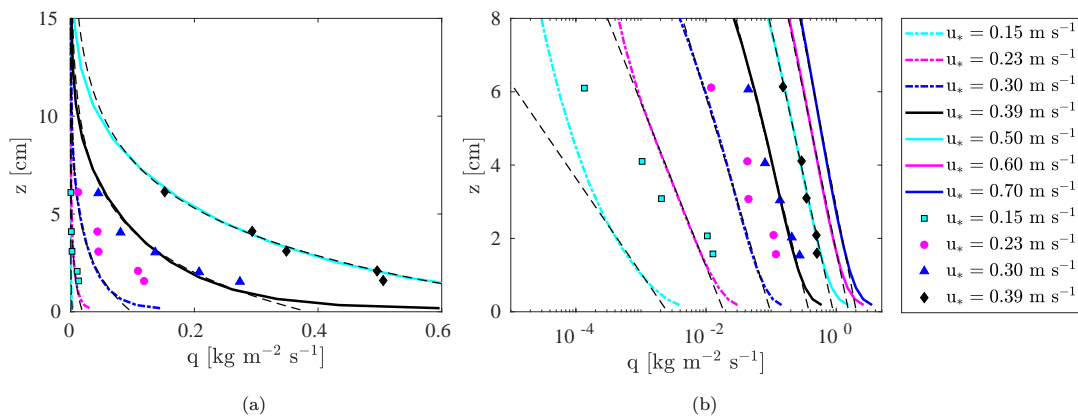


Figure 5.1: Vertical profile of particle mass flux obtained for different friction velocities. The black dashed lines are fits between the computed profiles and equation 2.4. The symbols denote the mass flux measurements performed by Sugiura et al. (1998). a) Linear plot (the mass flux profiles obtained for $u_*$ equal to 0.6 and 0.7 m s$^{-1}$ are not represented in the figure), b) Semi-logarithmic plot.

first 8 cm above the surface. The only exception is the mass flux profile obtained with the lowest friction velocity of 0.15 m s$^{-1}$. In this case, the friction velocity outside the saltation layer is slightly lower than the assumed fluid threshold friction velocity (from equation 3.4, $u_{*,ft}$ = 0.154 m s$^{-1}$). Therefore, saltation is highly intermittent. Sugiura et al. (1998) have also reported a fluid threshold friction velocity close to 0.15 m s$^{-1}$. During the experiments, saltation was only sustained at this low friction velocity with the addition of seeding particles at the upwind end of the wind tunnel. For the remaining friction velocities, deviations are seen between the modeled mass flux profiles and the exponential decay in approximately the first 1 cm above the surface and above 6-12 cm height, depending on the friction velocity. The deviations from an exponential decay above 6 cm height are due to the prevalence of particles in suspension. As discussed in section 2.3.3, these trends were also observed in field measurements of snow and sand saltation (Bauer & Davidson-Arnott, 2014; Namikas, 2003; Nishimura & Nemoto, 2005).

When comparing the modeled mass flux profiles with the SPC measurements of Sugiura et al. (1998) obtained at the same friction velocities, it is clear that the numerical model is significantly underestimating the mass flux in saltation. This discrepancy could not be solved by decreasing the roughness length from 10$^{-4}$ to 10$^{-5}$ m, which is more in agreement with previous wind tunnel experiments developed with snow (Nishimura et al., 2014). Negligible improvements were also obtained by decreasing the domain height to half the height of the wind tunnel (note that the top boundary of the domain is a symmetry plane). Despite the qualitative agreement, a quantitative agreement between simulation results and wind tunnel measurements certainly requires an adjustment in the parameters that control the surface processes of aerodynamic entrainment, rebound and splash. Even though a fitting exercise could be done to achieve a better agreement, we believe that detailed measurements of the near-surface particle-bed interaction and of the snow particle characteristics in saltation are needed for a further understanding of the near-surface processes and the development of improved parameterizations.
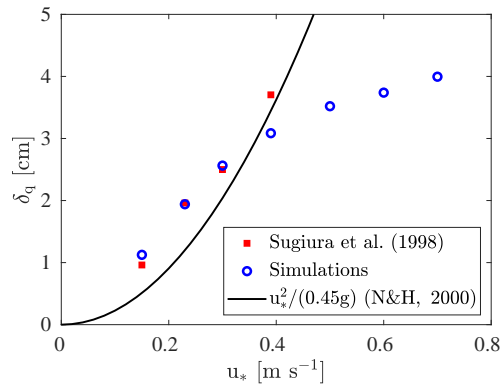


Figure 5.2: Decay height obtained by fitting the mass flux profiles presented in Figure 5.1 with equation 2.4. The values reported by Sugiura et al. (1998) and the expression proposed by Nishimura and Hunt (2000) (N&H, 2000) are also presented for comparison.

From fitting the computed mass flux profiles to equation 2.4, the decay height can be obtained. It is presented in Figure 5.2 as a function of the friction velocity. The values obtained by Sugiura et al. (1998) after fitting the measured mass flux profiles to equation 2.4 and the expression proposed by Nishimura and Hunt (2000) are also presented for comparison. For friction velocities ranging from 0.15 to 0.3 m s$^{-1}$, there is a fair agreement between the decay height obtained from measured and modeled mass flux profiles. The decay height increases with the increase of the friction velocity and follows approximately the trend proposed by Nishimura and Hunt (2000). However, for friction velocities greater than 0.3 m s$^{-1}$, the values of decay height obtained from the modeled mass flux profiles increase with the increase of the friction velocity at a much lower rate. In particular, the value obtained for $u_* = 0.39$ m s$^{-1}$ is lower than the value obtained by Sugiura et al. (1998) and a significant deviation between the modeled values and the expression proposed by Nishimura and Hunt (2000) is seen.

The agreement at low friction velocities between the modeled decay height and the expression proposed by Nishimura and Hunt (2000) suggests that the computed vertical ejection velocity scales with $u_*$, as proposed by Owen (1964) and discussed in section 2.3.1 and 2.3.3. In Figure 5.3, we present the computed vertical profiles of the particle streamwise velocity (Figure 5.3a) and of the vertical velocity of upward moving particles (Figure 5.3b). In the insets, the respective near-surface values are presented as a function of the friction velocity: $\bar{v}_x^{e,i}$ [m s$^{-1}$] and $\bar{v}_z^e$ [m s$^{-1}$] can be regarded as the particle slip velocity and the average vertical ejection velocity, respectively. For friction velocities ranging from 0.15 to 0.3 m s$^{-1}$, the particle streamwise velocity increases with height and with the friction velocity. The same trend is found for the vertical velocity of upward moving particles in the first 2 cm above the surface. At these low values of $u_*$, the average vertical ejection velocity and particle slip velocity also increase with the rise of the friction velocity. Therefore, the obtained increase in decay height as the friction velocity rises from 0.15 to 0.3 m s$^{-1}$ is indeed accompanied by an increase of the vertical ejection velocity.
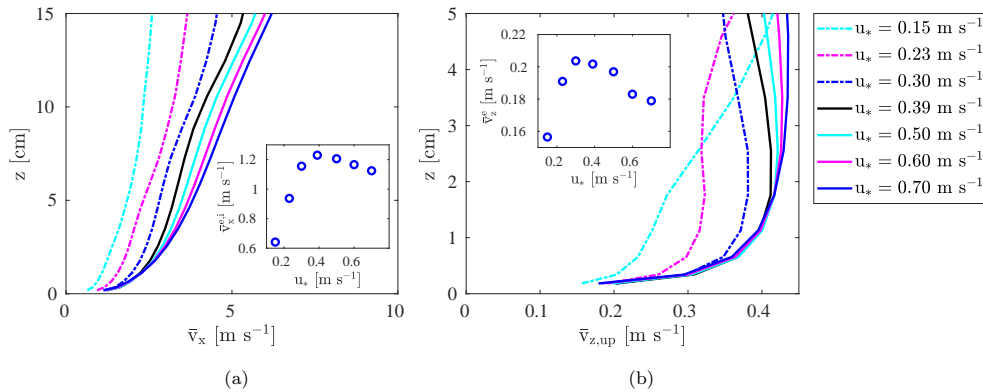


Figure 5.3: a) Vertical profiles of the particle streamwise velocity. b) Vertical profiles of the vertical velocity of upward moving particles. Results obtained for different friction velocities. The respective near-surface values are presented in the inset as a function of the friction velocity.

Conversely, a different trend is found for $u_*$ ranging between 0.39 and 0.7 m s$^{-1}$. For instance, an increase of the streamwise and vertical velocities with the increase of the friction velocity is only seen above approximately 1.5 cm height above the surface. Below this height, the particle velocity is mainly invariant with respect to $u_*$, which is in agreement with several saltation models (e.g., Kok & Renno, 2009; Niiya & Nishimura, 2022), measurements carried out over sand (Creyssels et al., 2009; Ho et al., 2011) (see discussion in sections 2.2.2 and 2.3.2), and the simulation results presented in chapter 4 for a variety of bed types. From the insets of Figure 5.3, it can be seen that the near-surface velocity actually decreases with the increase of the friction velocity.

In the model, while the average ejection velocity of splashed particles scales with the particle impact velocity, the average ejection velocity of aerodynamically entrained particles scales with the surface friction velocity, $u_{*,s}$ (Table 3.1). The average vertical mass flux of aerodynamically entrained and splashed particles are presented in Figure 5.4a and the equilibrium surface friction velocity is presented in Figure 5.4b, as a function of the friction velocity. Both quantities are computed by performing a surface average over the erodible bed and a time average over the last 100 s of the simulations. In Figure 5.4a, it is seen that the vertical mass flux of aerodynamically entrained particles is greater than the vertical mass flux of particles ejected via splash for $u_*$ equal to 0.15 and 0.23 m s$^{-1}$. For $u_* = 0.3$ m s$^{-1}$, splash entrainment is greater than aerodynamic entrainment, but they are both of the same order of magnitude. For these three simulations, in which aerodynamic entrainment plays an important role in steady-state saltation, the equilibrium surface friction velocity does not deviate significantly from the friction velocity outside the saltation layer (Figure 5.4b). Therefore, for $u_*$ ranging from 0.15 to 0.3 m s$^{-1}$, the increase of the vertical ejection velocity with the rise of $u_*$ is justified by the respective increase of the surface friction velocity.

For friction velocities greater than 0.3 m s$^{-1}$, the vertical mass flux of splashed particles
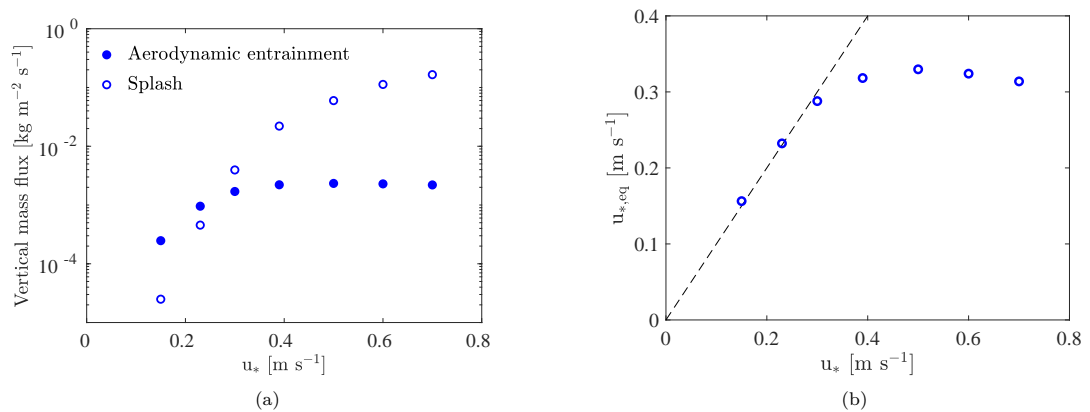


Figure 5.4: a) Vertical mass flux of aerodynamically entrained and splashed particles. b) Equilibrium surface friction velocity (the dashed line is the 1:1 slope). The results presented are averages over the surface and over the last 100 s of the simulations. They are presented as a function of the friction velocity.

is at least one order of magnitude greater than the vertical mass flux of aerodynamically entrained particles (Figure 5.4a). In addition, the equilibrium surface friction velocity deviates considerably from the friction velocity outside the saltation layer (Figure 5.4b). It reaches a value smaller than $u_*$, which decreases slightly with the rise of the friction velocity. Even though the ejection velocity of splashed particles scales with the velocity of the impacting particle and not directly with $u_{*,s}$, the computed particle impact velocity is highly correlated with the near-surface wind velocity (and, therefore, with the surface friction velocity) because of the exchange of momentum between the fluid and the particles close to the surface. At these high friction velocities, the wind velocity profiles exhibit a focus point at approximately 1 cm above the surface (see, for instance, Figure 4.1). Therefore, even though the near-surface wind velocity is approximately invariant with respect to $u_*$, the wind velocity below the focus point decreases slightly as $u_*$ increases. This justifies the observed decrease of $u_{*,eq}$ (Figure 5.4b) and of the near-surface particle velocity (insets in Figure 5.3) as the friction velocities rises above 0.39 m s$^{-1}$. For friction velocities greater than 0.3 m s$^{-1}$, the current numerical model does not confirm neither the scaling of the ejection velocity with the friction velocity outside the saltation layer, nor the scaling of the decay height with the vertical ejection velocity. In fact, even though the vertical ejection velocity decreases with the rise of the friction velocity for $u_* > 0.3$ m s$^{-1}$ (inset in Figure 5.3b), the decay height increases monotonically with $u_*$ (Figure 5.2). Therefore, the model proposed by Nishimura and Hunt (2000) might not be appropriate to parameterize the decay height during splash dominated saltation.

The obtained evolution of $u_{*,eq}$ at low friction velocities presented in Figure 5.4b contrasts with the results of sand saltation models. For instance, Kok and Renno (2009) neglected the surface process of aerodynamic entrainment and found $u_{*,eq}$ to decrease monotonically with the increase of the friction velocity. Sand particles have a higher density than snow particles, which implies a higher fluid threshold. In addition, as discussed in section 2.2.1, the surface shear stress is expected to be lower than the fluid threshold, which restricts the occurrence of aerodynamic entrainment during steady-state saltation, even at low friction velocities.

In contrast, similar features are seen in some snow saltation models in which aerodynamic entrainment is represented. For example, Nemoto and Nishimura (2004) found the equilibrium surface friction velocity to increase monotonically with the rise of the friction velocity from 0.23 to 0.39 m s$^{-1}$. The same increase in equilibrium surface friction velocity is seen in Figure 5.4b for this range of friction velocities. The values of $u_{*,eq}$ found by Nemoto and Nishimura (2004) are greater than the specified fluid threshold friction velocity, which suggests that aerodynamic entrainment also plays a role in their steady-state conditions. The process of aerodynamic entrainment is also taken into account in the numerical model of Doorschot and Lehning (2002). In their model, the parameterizations for aerodynamic entrainment and rebound are similar to those described in section 3.3, but the saltation system is - for simplicity - assumed to be either entirely composed of aerodynamically entrained particles or of particles that continuously rebound from the surface (in their model, no distinction is made between rebound and splash). Similarly to the results presented in Figure 5.4, Doorschot and Lehning (2002) found saltation to be dominated by aerodynamic entrainment at low friction

velocities and to be dominated by rebounding/splashed particles at high friction velocities. In addition, at low friction velocities, the equilibrium surface friction velocity increases with the rise of $u_*$ and a negligible deviation is seen between the values of $u_{*,eq}$ and $u_*$ due to the low number of particles aloft. At high friction velocities, $u_{*,eq}$ decreases slightly with the rise of $u_*$. In their model, the friction velocity at which the transition from aerodynamic entrainment to rebound/splash occurs depends primarily on the assumed restitution coefficient. This coefficient is expected to be highly dependent on the snow surface characteristics, which highlights the importance of the snow cover properties to the correct description of snow saltation and its scaling laws.

In the snow saltation model of Niiya and Nishimura (2022), $u_{*,eq}$ is found to decrease slightly with the increase of the friction velocity from 0.24 to 0.3 m s$^{-1}$. This differs from the increase of $u_{*,eq}$ found in Figure 5.4b for the same range of friction velocities. In their work, the fluid threshold friction velocity is assumed equal to 0.24 m s$^{-1}$ and the equilibrium surface friction velocity is found to be approximately equal to 0.2 m s$^{-1}$. In comparison with the current simulations, Niiya and Nishimura (2022) assumed a higher value for the fluid threshold friction velocity (0.24 versus 0.154 m s$^{-1}$) and a lower value for the roughness length ($10^{-5}$ versus $10^{-4}$ m). When decreasing $z_o$ from $10^{-4}$ to $10^{-5}$ m in the LES-LSM, we obtain a significant decrease in the equilibrium surface friction velocity during splash dominated saltation (compare, for instance, Figure 5.4b with the results presented in Figure 4.9 for $\sigma_d = 100$ $\mu$m). In this way, a decrease in $z_o$ and an increase in $\tau_{ft}$ reduce the range of friction velocities for which saltation is controlled by aerodynamic entrainment, which might justify the seemingly different results obtained with both models. In addition to the roughness length and the fluid threshold, other parameters that characterize the snow surface and highly influence the surface processes of aerodynamic entrainment, rebound and splash are expected to influence the importance of aerodynamic entrainment during steady-state saltation. The narrower the range of friction velocities for which aerodynamic entrainment plays an important role, the narrower is the range of friction velocities for which the decay height is well approximated by the expression of Nishimura and Hunt (2000).

The modeled saltation system is further investigated by the analysis of the particle hop height and length. The average hop height and length of saltating particles are computed from the analysis of all particle hops during the last 1 s of simulations. During this time period, the location of all particles aloft was outputted by the model at a very high frequency. In this analysis, we exclude the particles moving without regular contact with the bed (particles in suspension), as well as saltating particles with a highly perturbed or incomplete trajectory. As a result, we have analyzed the trajectories of approximately 70% of all particles moving along the first 8 cm above the surface during the studied time period. An example of a particle trajectory included in the analysis is presented in Figure 5.5a. The particles seldom reach the surface because the surface processes of rebound and splash are assumed to take place as soon as the particles reach a height lower than $z = 4\bar{d}$ (0.14 cm in this case).

The resultant average hop height and length are presented in Figure 5.5b as a function of the
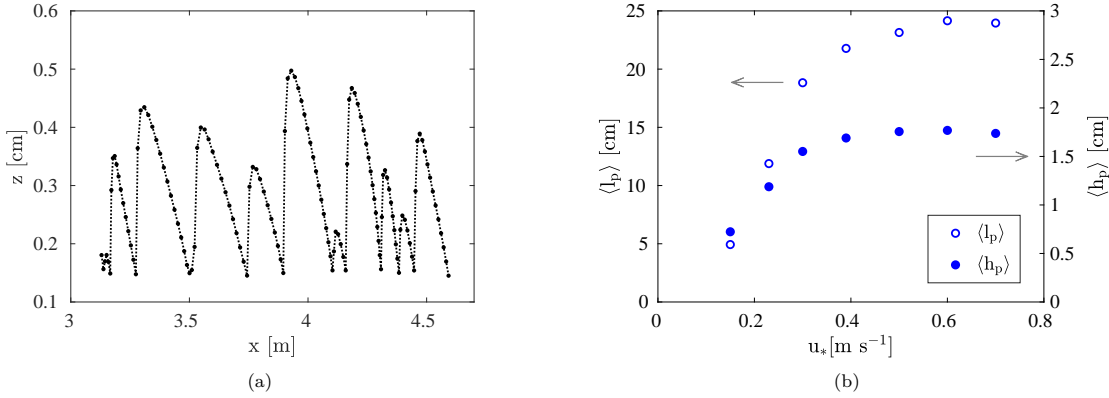
Figure 5.5: a) Example of a particle trajectory obtained for $u_* = 0.39$ m s$^{-1}$ (2D projection). b) Average hop height and length as a function of the friction velocity (the arrows indicate the respective y-axis of each set of values).

friction velocity. For the range of friction velocities studied, the average hop height mainly increases with the rise of the friction velocity (a slight decrease in the mean value is only seen when $u_*$ rises from 0.6 to 0.7 m s$^{-1}$). It increases with a higher rate for $u_*$ ranging from 0.15 to 0.3 m s$^{-1}$, which is in agreement with the evolution found for the vertical ejection velocity and the decay height (Figures 5.2 and 5.3b). As $u_*$ increases above 0.3 m s$^{-1}$ and saltation becomes splash dominated, the average hop height increases only slightly with the rise of the friction velocity, reaching a maximum value of approximately 1.8 cm. At these high friction velocities, even though the vertical ejection velocity decreases with the rise of the friction velocity (Figure 5.3b), $\langle h_p \rangle$ is approximately invariant with respect to $u_*$. This apparent discrepancy might be related to the fact that the hop height does not depend solely on the vertical ejection velocity, but also on the vertical component of the aerodynamic force applied to a particle along its trajectory.

As discussed in section 2.3.1 and 2.3.3, the decay height is expected to scale with the average hop height of particles in saltation (Gordon et al., 2009; Martin & Kok, 2017; Nishimura & Hunt, 2000). However, in the model, a linear relationship between $\langle h_p \rangle$ and $\delta_q$ is not found for $u_* > 0.3$ m s$^{-1}$. The modeled saltation system is not only comprised of particles undergoing a ballistic motion, but it also includes particles with highly disturbed trajectories. In this context, it is reasonable to assume that $\delta_q$ does not only depend on the hop height of ballistic hops, but also on the particle motion induced by turbulent eddies.

The average particle hop length, $\langle l_p \rangle$, follows the same trend as the average hop height: it mainly increases with the rise of the friction velocity (a slight decrease in the mean value is only found when $u_*$ rises from 0.6 to 0.7 m s$^{-1}$) and the rate at which $\langle l_p \rangle$ increases as the friction velocity rises is higher when $u_*$ varies between 0.15 and 0.3 m s$^{-1}$ than when $u_*$ is greater than 0.3 m s$^{-1}$ (Figure 5.5b). In this way, when saltation is dominated by splash, the particle hop length can be approximated as invariant with respect to $u_*$, which is in agreement with the saltation models of Ungar and Haff (1987) and Durán et al. (2011), discussed in section 2.2.3.
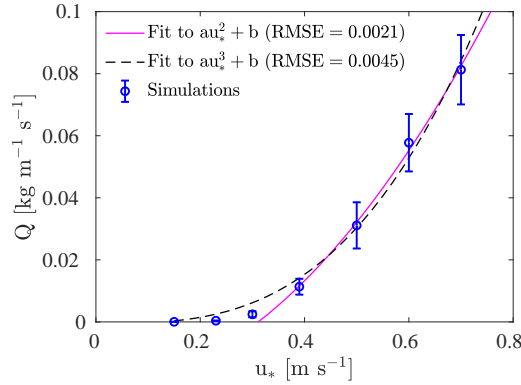
Figure 5.6: Transport rate as a function of the friction velocity. The curves represent fits between the results obtained for $u_* > 0.3 \text{ m s}^{-1}$ and quadratic and cubic functions. RSME denotes the root mean square error of the fit. The error bars are two times the standard deviation of the results.

If $\langle l_p \rangle$ is mainly invariant with respect to $u_*$, the transport rate is expected to scale with $u_*^2$. The transport rate is presented in Figure 5.6 as a function of the friction velocity. It is computed by integrating the particle mass flux along the height, from the surface to 15 cm height. The fits between the computed values obtained for $u_* > 0.3 \text{ m s}^{-1}$ and a quadratic function as well as a cubic function are also presented. Indeed, the transport rate obtained during splash dominated saltation is in good agreement with a quadratic curve, but the RMSE of the cubic function is only slightly higher. When considering the full range of friction velocities, a better agreement is actually found with the cubic function. These results highlight the need to acquire mass flux measurements for a wide range of friction velocities and snow surface characteristics to fully evaluate the scaling of the transport rate with the friction velocity.

The two saltation regimes obtained with the LES-LSM (dominated by aerodynamic entrainment or splash) are illustrated in Figure 5.7. In summary, as the friction velocity increases, the saltation system evolves from an aerodynamic entrainment dominated system to one dominated by splashed particles. In the first regime, the particle streamwise velocity increases with the rise of the friction velocity at all heights and the average hop height of saltating particles (represented by the line enclosing the ballistic trajectories) increases as well. As the friction velocity reaches higher values, the average hop height stops increasing significantly with the rise of the friction velocity. In fact, once saltation is dominated by splash, the average hop height is approximately invariant with respect to $u_*$. In addition, the particle streamwise velocity is also mainly invariant with respect to $u_*$ in the near-surface region where most saltating particles are. If we define the impact threshold friction velocity as the minimum friction velocity outside the saltation layer for which saltation is dominated by splash (in this case, $u_{*,it} \approx 0.3 \text{ m s}^{-1}$), these two saltation regimes are typical of saltation systems characterized by an impact threshold friction velocity greater than the fluid threshold friction velocity, $u_{*,ft}$. As previously discussed, this is not characteristic of sand saltation, but is probably representative of snow saltation for some snow surface characteristics. This more restrictive definition of the impact threshold friction velocity (recall the definition of $\tau_{it}$ presented in
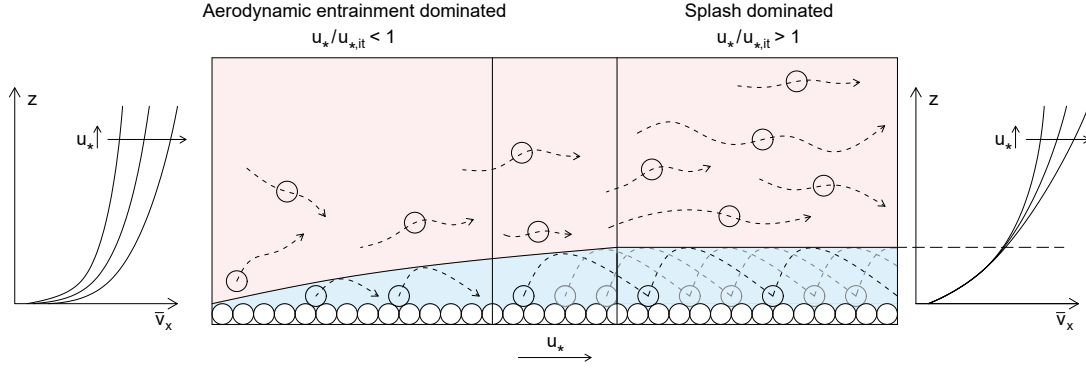
Figure 5.7: Illustration of the saltation system for increasing values of $u_*$: representation of the aerodynamic entrainment dominated and splash dominated regimes. The line enclosing the ballistic trajectories indicates the average hop height of the saltating particles. The particle streamwise velocity profiles characteristic of each regime are presented on the left and right-hand sides of the figure for increasing values of $u_*$. The dashed line on the plot on the right indicates the average hop height during splash dominated saltation.

section 2.2.1) is considered in some saltation models (e.g., Comola et al., 2022). In Figure 5.7, the line indicating the average hop height of saltating particles separates the regions where particle motion is controlled by wind-particle interaction only (above) and where it is highly dependent on the particle-bed interaction (below).

## 5.3    Conclusions

In this chapter, the wind tunnel experiments of Sugiura et al. (1998) are reproduced with LES-LSM simulations. The measured and modeled mass fluxes obtained for varying friction velocities are compared, and conclusions are drawn regarding the scaling of the vertical ejection velocity, hop height and length, and decay height with the friction velocity.

It is shown that the model is able to successfully reproduce the exponential decay of the mass flux with height seen in the measurements. However, significantly lower values of particle mass flux are obtained with the model. These observations underline the need to adjust the parameters used in the aerodynamic entrainement, rebound, and splash parameterizations. To this end, detailed wind tunnel and field experiments featuring these surface processes are required.

From the analysis for the particle velocity, vertical mass flux of aerodynamically entrained and splashed particles, and surface friction velocity, we show that the saltation system is characterized by two distinct regimes: while at low friction velocities, saltation is dominated by aerodynamic entrainment, at higher friction velocities it is dominated by splash. The scaling of the near-surface particle velocity, average hop height and decay height were shown to be a function of the saltation regime: when saltation is dominated by aerodynamic entrainment, the near-surface particle velocity and the average hop height increase with the friction velocity; when saltation is dominated by splash, these two quantities are mainly invariant with respect

to $u_*$. For both saltation regimes, the decay height of the mass flux profile is expected to increase with the friction velocity. However, when saltation is dominated by splash, it increases at a much lower rate than what is obtained when saltation is dominated by aerodynamic entrainment.

The effect of the saltation regime on the saltation dynamics and its scaling laws might partly justify the different scaling of $\delta_q$ with $u_*$ obtained by Sugiura et al. (1998) in a wind tunnel in comparison to the results obtained by Gordon et al. (2009) and Aksamit and Pomeroy (2016) in the field, discussed in section 2.3.3. Indeed, the limited size of a wind tunnel might restrict the development of a fully developed saltation system dominated by splash. This increases the relative importance of aerodynamic entrainment and might justify the observed increase of the decay height with $u_*^2$ obtained by Sugiura et al. (1998). Other aspects, such as the snow surface characteristics, are also expected to significantly influence the decay height and its scaling with $u_*$. Further investigation is needed to fully understand their impact on the decay height.

Overall, the results reveal that the scaling of the vertical ejection velocity, average hop height, and decay height with the friction velocity assumed in the model of Nishimura and Hunt (2000) is in agreement with a saltation system dominated by aerodynamic entrainment. However, these scaling laws are not consistent with a saltation system dominated by splash. As previously mentioned, this second saltation regime is characterized by a near-surface particle velocity invariant with respect to the friction velocity, as assumed by Pomeroy and Gray (1990). Taking into account that these two parameterizations are used in the blowing snow schemes of Meso-NH (Vionnet et al., 2014) and CRYOWRF (Sharma et al., 2023), these results support the conclusions drawn on chapter 2 regarding the inconsistency of some of the saltation parameterizations used in atmospheric models. Additionally, the results show that the average particle hop length is mainly invariant with respect to $u_*$ when saltation is dominated by splash, which is in agreement with the model of Durán et al. (2011). However, when fitting the transport rate to a quadratic and cubic functions, similar results are obtained.

Regarding the surface shear stress during saltation, the numerical simulations suggest that this quantity increases significantly with the rise of the friction velocity when saltation is dominated by aerodynamic entrainment. Therefore, the parameterizations that assume a constant value for $\tau_s$ are not able to simulate this low friction velocity regime. Moreover, the bed characteristics (and, therefore, the extent of each saltation regime), seem to have a strong influence on the relation between the surface shear stress and the fluid and impact thresholds. For instance, differently from what is commonly assumed for sand saltation, snow saltation models frequently predict an average surface shear stress greater than the fluid threshold. Only when saltation is dominated by splash, the surface friction velocity is approximately invariant with respect to the friction velocity.

By means of LES-LSM simulations, the work presented in this chapter offers a new insight into the saltation system. It reveals that snow saltation is not necessarily characterized by the same

scaling laws as sand saltation and showcases how detailed numerical simulations can be used to evaluate existing parameterizations.

# 6 The modeling of drifting and blowing snow using CRYOWRF

The detailed understanding of snow saltation dynamics presented in previous chapters is used to assess and improve the regional climate model CRYOWRF. This chapter directly addresses the main objective of this thesis: to improve large-scale estimates of drifting and blowing snow transport. The region around coastal Adélie Land in East Antarctica is simulated with CRYOWRF for one year. The simulation results are compared with field measurements collected at the automatic weather station D17, where continuous data of the snow mass flux in the first 2 m above the surface are available. In section 6.1, the CRYOWRF model is presented and discussed. The numerical settings of the simulations are presented in section 6.2, and the data post-processing of both the simulations and the field measurements are presented in section 6.3. The simulation results are presented and discussed in section 6.4 and the main conclusions are summarized in section 6.5.

## 6.1 The CRYOWRF model

CRYOWRF is a fully coupled atmosphere-snowpack solver (Sharma et al., 2023). It results from the coupling of the Weather Research and Forecasting model (WRF), a non-hydrostatic atmospheric model (Skamarock et al., 2019), with SNOWPACK, a high-complexity multilayer snow model (Lehning et al., 1999). In addition, CRYOWRF includes a blowing snow routine that models the aeolian transport of snow particles, their sublimation, and re-deposition. A short introduction to WRF and SNOWPACK is presented in section 6.1.1. The blowing snow model is described and discussed in section 6.1.2.

### 6.1.1 WRF and SNOWPACK

The Advanced Research WRF model (ARW-WRF v4.2.1) is used as the atmospheric core of CRYOWRF. The model solves the fully compressible, non-hydrostatic Euler equations that describe conservation of mass, momentum, and energy in the atmosphere (Skamarock et al., 2019). Cartesian coordinates are considered along the horizontal directions and a terrain-following

hybrid sigma-pressure coordinate is used in the vertical direction. The spatial derivatives of the different quantities of interest are numerically resolved in an Arakawa C grid. Several physical processes, such as cloud formation, radiative forcing, and turbulence mixing can be represented with different physical schemes. As in Sharma et al. (2023) and Gerber et al. (2023), the following physical schemes are considered in the simulations: the modified 2-moment Morison microphysics scheme, which includes an improved representation of secondary ice production (Sotiropoulou et al., 2021; Vignon et al., 2021), the Mellor-Yamada-Nakanishi-Niino 2.5 level turbulent kinetic energy (MYNN2.5) planetary boundary layer scheme, the Rapid Radiative Transfer Model (RRTMG) for shortwave and longwave radiation, and the Kain-Fritsch convection scheme.

In CRYOWRF, SNOWPACK is used as the land-surface model. Similarly to all land-surface models in WRF, SNOWPACK makes use of several meteorological quantities computed by WRF and its modules (e.g., air temperature, horizontal wind velocity, radiative forcing, snowfall) and provides heat and moisture fluxes over land-surface grid points. On sea-ice grid points, the NoahMP land-surface model is used instead.

SNOWPACK is a one-dimensional model, which represents the snow cover at each land-surface grid point by a multilayer column. Snow is characterized in each layer as a mixture of ice, air, and water, and the snow grains are characterized by their size, sphericity, dendricity, as well as the size and number of ice bonds between them (Lehning et al., 1999). From the snow microstructure, several snow properties, such as density, thermal conductivity, and albedo, are derived. In particular, the snow albedo is computed with the model developed by Kuipers Munneke et al. (2011) and implemented in SNOWPACK by Steger et al. (2017). Using a dynamic finite element mesh, the heat equation is solved along the snowpack, together with snow compaction and water percolation. The latter is described by the bucket model. At the snow-atmosphere interface, the Hotslag stability correction is taken into account in the calculation of the heat fluxes (Schlögl et al., 2017).

A detailed description of both WRF and SNOWPACK can be found in the mentioned references, particularly in the works of Skamarock et al. (2019) and Lehning et al. (1999). In Sharma et al. (2023), a detailed description of the coupling procedure and the model capabilities is provided.

### 6.1.2   The blowing snow model

The blowing snow model implemented in CRYOWRF follows closely the one developed by Vionnet et al. (2014) and implemented in Meso-NH. A detailed description of the model equations and its numerical implementation is presented in Sharma et al. (2023). Therefore, in this section, only a summary of the model framework is presented and more focus is given to the modeling choices and their validity. The modeling of snow saltation, snow suspension, and the saltation-suspension interface are presented and discussed in the next subsections. Finally, in the last subsection, improvements are suggested.

**Snow saltation**

The onset of snow erosion and the transport rate in saltation (vertically integrated mass flux) are directly computed by SNOWPACK. Snow saltation starts once the surface shear stress exceeds the fluid threshold, $\tau_{ft}$. In SNOWPACK, $\tau_{ft}$ is parameterized with the expression proposed by Lehning et al. (2000), which is based on the model of R. A. Schmidt (1980):

$$\tau_{ft} = A\rho_i g r_g (SP + 1) + B N_3 \sigma_r \left(\frac{r_b}{r_g}\right)^2 \tag{6.1}$$

where $A$ and $B$ are empirical constants set to 0.02 and 0.0015, respectively, $\rho_i$ [kg m$^{-3}$] is the density of ice, $r_g$ [m] and $r_b$ [m] are the grain and bond radius, respectively, $SP$ is the grain sphericity, which varies between 0 and 1, $N_3$ is the coordination number, which is a measure of the average number of ice bonds between each snow grain and the neighboring ones, and $\sigma_r$ [Pa] is a reference shear strength equal to 300 Pa. In equation 6.1, the values of $r_g$, $r_b$, $SP$ and $N_3$ from the uppermost snow layer are used. Taking into account that these quantities are directly computed by SNOWPACK, the value of $\tau_{ft}$ varies in time and space according to the metamorphic processes taking place in the snowpack.

The transport rate in saltation, $Q_{salt}$ [kg m$^{-1}$ s$^{-1}$], is parameterized with the expression proposed by Sørensen (2004):

$$Q_{salt} = \frac{\rho_a u_*^3}{g}\left(1 - \frac{u_{*,s}^2}{u_*^2}\right)\left(\alpha + \beta\frac{u_{*,s}^2}{u_*^2} + \gamma\frac{u_{*,s}}{u_*}\right) \tag{6.2}$$

where $\alpha$, $\beta$, and $\gamma$ are empirical parameters, which are expected to vary with the snow surface characteristics. However, following Vionnet et al. (2014), they are currently set to constant values obtained by fitting equation 6.2 to the wind tunnel measurements of Nishimura and Hunt (2000): $\alpha = 2.6$, $\beta = 2.5$, $\gamma = 2$. According to the analysis presented in chapter 4, a relatively good agreement between small-scale numerical simulations and equation 6.2 is obtained (see, for instance, Figure 4.11). Nevertheless, additional studies are needed to fully quantify the effect of the snow surface characteristics on the transport rate and further adjust the empirical parameters $\alpha$, $\beta$, and $\gamma$.

In the absence of snow transport, the near-surface boundary layer is typically characterized by a constant fluid shear stress profile (Prandtl, 1935). In this case, $u_*$ and $u_{*,s}$ are identical. However, during snow transport events, the momentum exchange between the air flow and the snow particles aloft leads to a decrease in the near-surface shear stress, $u_{*,s}$ (see section 2.1). This local decrease in shear stress is not represented in CRYOWRF. Nevertheless, when computing equation 6.2, $u_{*,s}$ is assumed to be different from $u_*$ and equal to the fluid thresh-

old friction velocity, $u_{*,ft}$. Therefore, the value assumed for $u_{*,s}$ varies with the snow surface characteristics. The value of $u_*$ is retrieved from the surface layer scheme of WRF.

In contrast to the assumption used in CRYOWRF, Sørensen (2004) follows the hypothesis proposed by Owen (1964) for sand saltation and assumes that $u_{*,s}$ is equal to the impact threshold friction velocity, $u_{*,it}$. This hypothesis was discussed in detail in section 2.2.1. According to Owen (1964), $u_{*,it}$ is lower than $u_{*,ft}$, but both are expected to be invariant with respect to $u_*$ and solely a function of the bed characteristics. Accurate quantification of $u_{*,s}$ during snow saltation remains a challenge (e.g., B. Li & McKenna Neuman, 2012; Walter et al., 2014), and further investigation is needed to improve the parameterizations used in blowing snow schemes. For example, even the base assumption that $u_{*,s}$ is invariant with respect to $u_*$ is challenged by some numerical models of snow saltation (Doorschot & Lehning, 2002; Nemoto & Nishimura, 2004), as well as by the results presented in chapter 5. However, considering the current understanding of the topic, the assumption $u_{*,s} = u_{*,ft}$ is deemed acceptable for large-scale simulations.

**Snow suspension**

The transport of snow particles to higher regions of the boundary layer and across greater distances is modeled with advection-diffusion-type equations that resolve the mass and number mixing ratios of blowing snow particles, $m_{bs}$ [kg kg$^{-1}$] and $N_{bs}$ [kg$^{-1}$], respectively (Déry & Yau, 1999; Vionnet et al., 2014):

$$\frac{\partial m_{bs}}{\partial t} + U_j \frac{\partial m_{bs}}{\partial x_j} = K_{bs} \frac{\partial^2 m_{bs}}{\partial x_j^2} \delta_{j3} + \frac{\partial}{\partial x_j} \left( m_{bs} V_m \delta_{j3} \right) + S_m \tag{6.3a}$$

$$\frac{\partial N_{bs}}{\partial t} + U_j \frac{\partial N_{bs}}{\partial x_j} = K_{bs} \frac{\partial^2 N_{bs}}{\partial x_j^2} \delta_{j3} + \frac{\partial}{\partial x_j} \left( N_{bs} V_N \delta_{j3} \right) + S_N \tag{6.3b}$$

where $x_j$ [m], $j = 1, 2, 3$, denotes the zonal, meridional, and vertical coordinates in the terrain-following reference frame of WRF, and $U_j$ [m s$^{-1}$] is the air velocity along the mentioned directions. $K_{bs}$ [m$^2$ s$^{-1}$] is the turbulence diffusion coefficient, $V_m$ [m s$^{-1}$] and $V_N$ [m s$^{-1}$] are the mass- and number-weighted terminal fall velocities of blowing snow particles, and $S_m$ [kg kg$^{-1}$ s$^{-1}$] and $S_N$ [kg$^{-1}$ s$^{-1}$] are the source/sink terms due to phase change, i.e., sublimation of blowing snow particles ($S_m$, $S_N < 0$) or deposition of water vapor on the blowing snow particles ($S_m$, $S_N > 0$). Using the continuum approximation, equations 6.3a-b are derived from the mass conservation equation of blowing snow particles.

In order to resolve the mass and number mixing ratios near the surface, a fine vertical mesh is specified between a point close to the surface and the first WRF vertical grid point. In this way, equations 6.3a-b are solved numerically for all WRF and fine mesh grid points. In previous

studies (Gerber et al., 2023; Sharma et al., 2023), the lower end of the fine mesh was specified at 0.5 m height. In this work, it is set to 0.2 m in order to better capture the strong gradients of particle mass and number mixing ratios close to the surface. This value is also closer to that used in Meso-NH by Vionnet et al. (2014), equal to 0.15 m.

The particle size distribution at all vertical levels is given by a 2-parameter Gamma distribution, as proposed by Vionnet et al. (2014). This assumption is in agreement with several field observations of blowing snow (e.g., Nishimura & Nemoto, 2005; R. A. Schmidt, 1982). According to these field observations, the shape parameter is expected to increase with height. However, for simplicity, it is set to a fixed value ($\alpha = 3$). By definition, the scale parameter is proportional to the average particle diameter. Taking into account that $m_{bs}$ and $N_{bs}$ are related through the particle size distribution, the average particle diameter is computed from the solution of equations 6.3a-b.

While Vionnet et al. (2014) assumed $K_{bs}$ to be four times smaller than the turbulence diffusivity coefficient used for scalars, $K_{sc}$ [m$^2$ s$^{-1}$], in CRYOWRF, $K_{bs}$ is assumed equal to $K_{sc}$ (please note that the variable $\zeta$ defined in equation 4 in Vionnet et al. (2014) is not set to 0.25, as mentioned in their text, but to 4 - V. Vionnet, personal communication, July 4, 2023). The value of $K_{sc}$ is directly retrieved from the surface layer scheme of WRF. In the fine mesh, a linear interpolation is considered between the surface (where $K_{bs}$ is assumed to be zero) and the value at the first WRF staggered grid point. $V_m$ and $V_N$ are computed with the best number approach (Khvorostyanov & Curry, 2002; Mitchell, 1996; Sulia & Harrington, 2011) as a function of the average particle diameter, the particle and air densities, and the air dynamic viscosity. The equations used to compute $V_m$ and $V_N$ are further detailed in Sharma et al. (2023). The processes of phase change that take place on a single blowing snow particle (assumed spherical and with the density of ice) are computed with the model of Thorpe and Mason (1966). $S_m$ can then be obtained by performing an integration over the number distribution. Following Morrison and Grabowski (2008), $S_N$ is assumed equal to $S_m N_{bs}/m_{bs}$, which is accurate for a uniform particle size distribution.

**The saltation-suspension interface**

The lower boundary condition for equations 6.3a-b is defined at height $z_{LB}$ [m], computed with the expression of Pomeroy and Male (1992):

$$z_{LB} = 0.08436 u_*^{1.27}. \tag{6.4}$$

$z_{LB}$ is generally regarded as the height of the saltation layer. However, equation 6.4 is not a rigorous estimate of the saltation layer height, but rather an approximation, suitable for the blowing snow model used by Pomeroy and Male (1992). As discussed in section 2.4, all parameterizations specified at the lower boundary as well as equations 6.3a-b, used to

describe the mass and number mixing ratios of particles in suspension, must be valid at $z_{LB}$. For friction velocities ranging between 0.4 and 1 m s$^{-1}$, equation 6.4 yields $z_{LB}$ equal to 0.03 to 0.08 m. As discussed in chapter 4, a significant number of particles is expected to be in saltation at those heights (see, for instance, the particle size distribution presented in Figure 4.10). Therefore, the particle motion at those heights and, consequently, the temporal and spatial evolution of the mass and number mixing ratios are not expected to be controlled by the same processes represented in equations 6.3a-b. In principle, boundary conditions should not be specified outside the region of validity of the equations. Hence, the use of equation 6.4 is expected to lead to inaccuracies in the resultant mass and number mixing ratios. A more consistent setup would be obtained if $z_{LB}$ was specified in a region where the particle motion is mainly dominated by particle advection and turbulence diffusion. According to the results presented in chapter 4, this is obtained above approximately 0.12 m height (Figure 4.7 and 4.10).

Let us denote by $m_{bs_o}$ [kg kg$^{-1}$] and $N_{bs_o}$ [kg$^{-1}$] the mass and number mixing ratios, respectively, at the lower boundary $z_{LB}$. In order to estimate $m_{bs_o}$, we assume that the vertical profile of particle mass flux in saltation, $q$, follows an exponential decay of the form of equation 2.4:

$$q(z) = \frac{Q_{salt}}{\delta_q} \exp\left(-\frac{z}{\delta_q}\right). \tag{6.5}$$

As discussed in section 2.3.3, the exponential decay of the mass flux profile is a well-known feature of the saltation system, observed in both wind tunnel and field experiments (e.g., Nishimura & Nemoto, 2005; Sugiura et al., 1998). As previously stated, the integral of $q$ along the height yields the vertically integrated mass flux in saltation, $Q_{salt}$. Therefore, it follows that the mass flux at the surface, $q_o$, is given by $Q_{salt}/\delta_q$. The decay height is assumed to scale with $u_*^2$ as proposed by Nishimura and Hunt (2000):

$$\delta_q = \frac{u_*^2}{0.45g}. \tag{6.6}$$

This parameterization for $\delta_q$ was previously introduced in section 2.3.3. It is based on the idea that $\delta_q$ scales with the average hop height of saltating particles and that the latter scales with the square of the vertical ejection velocity of the particles in saltation. Nishimura and Hunt (2000) followed the arguments proposed by Owen (1964) and assumed that the vertical ejection velocity of saltating particles scales with $u_*$ and, consequently, that both the average hop height and the decay height scale with $u_*^2$. However, this assumption is not fully supported by both field and wind tunnel experiments conducted with sand and snow (e.g., Creyssels et al., 2009; Gordon et al., 2009; Martin & Kok, 2017), as well as numerical simulations (e.g., Durán et al., 2011). In addition, numerical simulations performed with the LES-LSM have

shown that the premises behind equation 6.6 might only be valid at very low values of friction velocity (see discussion in section 5.2).

Although the expression proposed by Nishimura and Hunt (2000) is not in agreement with the latest measurements and snow saltation simulations, more research is needed to improve the calculation of $\delta_q$ in large-scale models. In addition, the value of $\delta_q$ influences not only the decay of mass flux with height but also the value of the mass flux at the surface (recall that $q_o = Q_{salt}/\delta_q$). Therefore, extensive measurements of the vertical profile of snow mass flux in saltation are needed to better adjust the parameterizations used for both $Q_{salt}$ and $\delta_q$.

Following Pomeroy and Gray (1990), the particle velocity in the saltation layer along the horizontal wind direction, $\bar{v}_h$ [m s$^{-1}$], is given by:

$$\bar{v}_h = 2.8 u_{*,s} \tag{6.7}$$

where $u_{*,s}$ is approximated by the fluid threshold friction velocity, $u_{*,ft}$, as previously discussed. Please note that $\bar{v}_h$ is equivalent to $\bar{v}_x$ discussed in section 2.3.2, because both the indices $h$ and $x$ denote the main direction of the particles in saltation (streamwise direction). As discussed in section 2.3.2, the horizontal velocity of saltating particles is expected to be approximately invariant with respect to $u_*$ in the first 0.01-0.02 m above the surface. However, the particle velocity of saltating particles is expected to increase linearly with height in the first centimeters above the surface and to increase significantly with $u_*$ above approximately 0.03 m height (Aksamit & Pomeroy, 2016; Creyssels et al., 2009; Ho et al., 2011; Nishimura et al., 2014). Therefore, the use of equation 6.7 at different levels above the surface, $z_{LB}$, according to the value of $u_*$, might not always lead to acceptable figures. For fluid threshold friction velocities ranging between 0.2 to 0.4 m s$^{-1}$, equation 6.7 yields $\bar{v}_h$ equal to 0.56 to 1.12 m s$^{-1}$, which is in agreement with the range of near-surface particle velocities measured by Aksamit and Pomeroy (2016) during blowing snow events (0.4 to 0.8 m s$^{-1}$ at the surface, and 1 to 2 m s$^{-1}$ at approximately 0.015 m height). However, between 0.015 and 0.04 m above the surface, Nishimura et al. (2014) measured significantly higher values, ranging between 3 and 4 m s$^{-1}$. These values are also consistent with the wind tunnel measurements reported in Appendix A (Figure A.4a). Thus, during moderate to high blowing snow events (for example, $u_*$ ranging between 0.5 to 1 m s$^{-1}$, which implies $z_{LB}$ equal to 0.035 to 0.08 m), the use of equation 6.7 is expected to underestimate the saltating particles velocity.

Given $q$ and $\bar{v}_h$, the mass mixing ratio at the top of the saltation layer can finally be computed:

$$m_{bs_o} = \frac{q(z_{LB})}{\rho_a \bar{v}_h}. \tag{6.8}$$

From equation 6.8, it is clear that an underestimation of $\bar{v}_h$ leads to an overestimation of the mass mixing ratio, $m_{bs_o}$.

Similarly to the particles in suspension, the particle size distribution at the lower boundary is assumed to follow a 2-parameter Gamma distribution. $N_{bs_o}$ is then computed from the particle size distribution and the value of $m_{bs_o}$. The shape parameter is set to 3, which is in good agreement with the values reported by Nishimura and Nemoto (2005) below the height of 0.1 m. The average particle diameter at $z_{LB}$, $\bar{d}_o$ [m], is assumed constant and equal to 200 $\mu$m. Therefore, it is assumed that $\bar{d}_o$ is invariant with height, friction velocity, and snow surface characteristics. On the contrary, Nishimura and Nemoto (2005) observed a significant variation in the mean particle diameter with height and friction velocity in the first 0.1 m above the surface. For instance, for friction velocities ranging between 0.21 and 0.56 m s$^{-1}$, the average particle diameter was found to vary between 100 and 220 $\mu$m. Conversely, between 0.1 and 0.2 m height, the average particle diameter varied along a shorter range (90-120 $\mu$m). According to the results presented in chapter 4, in the first 0.1 m above the surface, the particle size distribution varies both with height and with the snow surface characteristics (Figure 4.10). In contrast, between 0.1 and 0.2 m height, similar particle size distributions are obtained, mainly composed of particles smaller than 100 $\mu$m. Thus, the value of $\bar{d}_o$ is necessarily characterized by a higher uncertainty when $z_{LB}$ is defined according to equation 6.4 than if $z_{LB}$ is defined between 0.1 and 0.2 m.

**Proposed improvements**

As discussed previously, the modeling of the saltation-suspension interface in CRYOWRF is not fully consistent with the current understanding of snow saltation dynamics, nor with the numerical simulations presented in chapter 4. The main issues are related to the use of a variable height for the lower boundary and a constant horizontal particle velocity.

Taking into account that the advection-diffusion equations used to compute the mass and number mixing ratios of blowing snow (equations 6.3a-b) are tailored to represent the process of snow suspension, these equations are not able to correctly represent the transport of snow in saltation. In contrast, the exponential decay presented in equation 6.5 is mainly representative of the particle mass flux in the first centimeters above the surface, where a significant number of particles are expected to be in saltation. If we consider that the assumed exponential decay correctly describes the mass flux close to the surface, it is clear that this mass flux corresponds to the motion of large particles, which are generally too heavy to be in suspension and whose motion is highly influenced by the proximity to the snow surface. Therefore, even though the exponential decay might be a less accurate approximation above 0.1 m height, it might be a better approximation of the mass flux available to be transported in suspension. Based on this reasoning, a more consistent setup would be obtained if $z_{LB}$ was specified at a height greater than 0.1 m. For instance, at 0.15 m height.

In addition, specifying $z_{LB}$ above 0.1 m height might reduce the uncertainty of the selected

average particle diameter. In fact, the particle size distribution is expected to exhibit lower variability above 0.1 m height (Nishimura & Nemoto, 2005). For example, a value between 90 and 120 $\mu$m can be chosen.

Regarding the particle horizontal velocity, $\bar{v}_h$, field and wind tunnel measurements revealed that the particle velocity increases with the height above the surface, as well as with the friction velocity above 0.01-0.02 m height (e.g., Nishimura et al., 2014). Therefore, the assumption of a constant particle velocity throughout the saltation layer cannot be considered a good approximation. To ensure that the particle velocity is of the order of magnitude of the values reported in the literature, the following can be assumed regarding the evolution of $\bar{v}_h$: on the surface, $\bar{v}_h$ is given by equation 6.7; from the surface to the height of 0.02 m, it is assumed to increase linearly with height (e.g., Aksamit & Pomeroy, 2016; Ho et al., 2011); above 0.02 m, $\bar{v}_h$ is assumed to be a fraction of the horizontal wind velocity. Therefore:

$$
\bar{v}_h(z) = \begin{cases} \left(\bar{v}_h(0.02) - 2.8 u_{*,s}\right) \frac{z}{0.02} + 2.8 u_{*,s} & \text{,if } z < 0.02 \\[2ex] 0.75 \frac{u_*}{\kappa} \ln\left(\frac{z}{z_o}\right) & \text{,if } z \geq 0.02 \end{cases} \tag{6.9}
$$

where $\kappa = 0.4$ is the von Kármán constant and $u_{*,s}$ is approximated by the fluid threshold friction velocity, as previously discussed. Above 0.02 m, the particle velocity is assumed to be 75% of the horizontal wind velocity. This ratio is estimated from measurements performed by Nishimura et al. (2014) at approximately 0.12 m height for friction velocities ranging between 0.37 and 0.63 m s$^{-1}$. The chosen value is also in agreement with the wind tunnel measurements presented in Appendix A at 0.04 m height (62%). More measurements of particle velocity in saltation are needed to better assess the variation of $\bar{v}_h$ with height and $u_*$. Nevertheless, equation 6.9 is considered a reasonable first estimate, which yields values of particle velocity of the order of magnitude of those reported in the literature along the first 0.15 m above the surface.

## 6.2  Numerical settings

The numerical setup of the simulations closely follows the one suggested by Sharma et al. (2023) (case study Ib, input data files at Sharma et al. (2021)). The simulation area encompasses the region around the Dumont d'Urville (DDU) station and the Automatic Weather Stations (AWS) D17 and D47 in coastal Adélie Land, East Antarctica. Two domains are considered: a parent domain (d1) with a horizontal resolution of 9 km and a side length of approximately 1500 km (164×165 grid cells), and an inner nest (d2) with a horizontal resolution of 3 km and a side length of approximately 750 km (250×253 grid cells). One-way nesting is considered in the simulations. Topography and land use are obtained from the Reference Elevation Model of Antarctica (REMA; Howat et al., 2019) and the AntarcticaLC2000 land use data (Hui et al.,

2017). The atmosphere in both domains is discretized in 69 vertical levels. The pressure at the top of the domain is set to 5 kPa, which is located at approximately 18 km a.s.l. (above sea level). The fine mesh specified between the surface and the lowest point on the WRF grid (approximately 8 m a.g.l. - above ground level) is composed of 8 vertical levels, logarithmically spaced, extending from 0.2 to 5 m a.g.l.

A 1-year simulation is performed with both domains between 1 September 2014 and 1 September 2015. For the parent domain, a spin-off of approximately 2 months is considered (starting time: 30 June 2014 00:00 UTC). The initial snow cover is derived from the results of Gerber et al. (2023) developed over the entire Antarctic continent with a horizontal resolution of 27 km. In order to adjust the snow cover to the current spatial resolution, the post-processing algorithms available at Sharma et al. (2021) are used. The simulation time step is 45 s and 15 s for the parent domain and the inner nest, respectively. The blowing snow routine is called at all WRF time steps and is active in both domains. For SNOWPACK, a time step of 900 s is specified for both domains.

The model is initialized and forced at its lateral boundaries by the ERA5 reanalysis data (Hersbach et al., 2020). In addition, the simulations are nudged against ERA5 in the upper atmosphere (top 20 vertical levels) for the zonal and meridional wind velocities. All domains consider the same set of physical parameterizations presented in section 6.1.1. The snow surface roughness, $z_o$, is assumed to be equal to 0.002 m. In SNOWPACK, a minimum snow layer thickness of 1 mm is specified and the density of fresh snow is set to 300 kg m$^{-3}$.

To study the sensitivity of the model to a number of snow saltation parameterizations, four 1-month simulations are performed between 1 July 2015 and 1 August 2015. This sensitivity study is motivated by the discussions presented in section 6.1.2. For example, one concerning the inconsistencies that arise from setting $z_{LB}$ very close to the surface, and another concerning the variation of the particle horizontal velocity with height and $u_*$, which is currently neglected in the model. In order to correct these issues, the value of $z_{LB}$ is set to a constant value equal to 0.15 m, the average particle diameter at $z_{LB}$ is reduced from 200 to 100 $\mu$m, and $\bar{v}_h$ is assumed to vary with height and $u_*$ according to equation 6.9.

The parameterizations used in the sensitivity study are summarized in Table 6.1. At first, only one modification is made per simulation to understand the individual effect of each

|          | $\bar{d}_o$ [$\mu$m] | $\bar{v}_h$ [m s$^{-1}$] | $z_{LB}$ [m] |
|----------|------|----------|----------|
| Standard | 200  | Eq. 6.7  | Eq. 6.4  |
| S1       | 100  | -        | -        |
| S2       | -    | Eq. 6.9  | -        |
| S3       | -    | -        | 0.15     |
| S4       | 100  | Eq. 6.9  | 0.15     |

Table 6.1: Parameterizations used in the sensitivity analysis. When nothing is specified, the standard values and expressions are used.

parameterization (simulations S1-S3). Finally, the parameters used in simulations S1 to S3 are combined (simulation S4). Fifteen days of spin-off are considered for both domains (starting time: 15 June 2015 00:00 UTC) and the outputs of the 1-year simulation are used to initialize the simulations.

## 6.3 Experimental data and post-processing

The post-processing of the simulation results is tailored to facilitate the comparison between the simulations and the measurements performed at D17 (-66.7°S, 139.9°E), located at 450 m a.s.l. and 10 km further inland relative to DDU. As described in Amory (2020), the AWS installed at D17 is composed of six anemometers, six thermohydrometers (both logarithmically spaced between 0.8 and 5.5 m a.g.l.), one wind vane at 5.5 m a.g.l., one barometric pressure sensor, one ultrasonic depth gauge and two 1-m long second-generation FlowCapt sensors (Trouvilliez et al., 2015).

FlowCapt is an acoustic sensor that measures the horizontal mass flux of blowing snow (Chritin et al., 1999). It consists of a tube with an electroacoustic transducer, in which the acoustic pressure induced by the particles impacting the tube is converted into a snow mass flux. Each 1-m long FlowCapt yields a mass flux value, $q_{FC}$ [kg m$^{-2}$ s$^{-1}$], which is representative of the average mass flux over the cross-section area of the FlowCapt. According to Amory (2020), the two FlowCapt sensors (FC1 and FC2) were vertically superimposed, separated by a 0.1-m long connecting piece. At the time of deployment, the lower end of FC1 was placed 0.1 m above the snow surface. Therefore, the setup allowed for the assessment of the average mass flux of blowing snow particles between 0.1 and 2.2 m above the snow surface. FC1 would then gradually sink into the snowpack, mainly due to the occurrence of snowfall. The station was visited and maintained almost every year during the austral summer. Therefore, mainly once a year, the sensors were lifted to recover their original distance from the snow surface.

The different quantities measured at the AWS were sampled at 15-s intervals and recorded on a data logger at a resolution of 30 minutes (Amory, 2020). With the exception of surface pressure and wind direction, the 30-minute averages of the data collected at D17 between 2010 and 2018 are available at Amory et al. (2020). In order to compare the simulation results with the field measurements, the model outputs from the closest grid cell from D17 are used and 30-minute averages of the different quantities of interest are computed. As described in Amory (2020), the measured relative humidity (RH) with respect to liquid water is converted to RH w.r.i. (with respect to ice) using the expression for the saturated vapor pressure of Goff and Gratch (1945). The same expression is used to calculate the simulated RH w.r.i. as a function of the simulated 2-m water vapor mixing ratio and surface pressure. As described in Amory (2020), the 2-m wind velocity reported in the data set is not exactly measured at 2 m height. As the snow cover accumulates or depletes at the site, the height of the anemometers above the snow surface varies over time. Therefore, the 2-m wind velocity corresponds to the horizontal wind velocity measured by the 2-m height closest anemometer. Taking into account that the

actual height at which the wind velocity is measured at each time step is known, this same varying height is used to compute the simulated 2-m wind velocity. It is deduced from the simulated 10-m horizontal wind velocity, assuming a logarithmic profile and the roughness length used in the simulations. The modeled wind direction is computed from the 10-m zonal and meridional wind velocity components. Moreover, the potential temperature is computed from the measured/simulated 2-m air temperature and surface pressure. In the analysis, a modified version of the post-processing scripts available at Sharma et al. (2021) and Gerber et al. (2022) is used.

The mass flux measured by each FlowCapt needs to be corrected for the actual exposed length of the sensor: $q'_{FC} = q_{FC} H / h$, where $H$ [m] is the FlowCapt length (equal to 1 m), $h$ [m] is the exposed length of the sensor, and $q'_{FC}$ [kg m$^{-2}$ s$^{-1}$] is the corrected FlowCapt mass flux. The vertically integrated mass flux along the exposed length of each FlowCapt, $Q_{FC}$ [kg m$^{-1}$ s$^{-1}$] (hereafter denoted FlowCapt transport rate), is computed by multiplying $q'_{FC}$ by the exposed length of the sensor:

$$Q_{FC} = q'_{FC} h = q_{FC} \frac{H}{h} h = q_{FC} H. \tag{6.10}$$

In order to compare the simulated blowing snow mass flux with the FlowCapt measurements, the 30-minute averaged mass flux computed by the model is vertically integrated along the exposed length of each FlowCapt using a simple rectangular integration. As mentioned in section 6.1.2, the horizontal velocity of the particles in suspension is assumed equal to the wind velocity. In this way, the blowing snow mass flux, $q_{bs}$ [kg m$^{-2}$ s$^{-1}$], at each grid point is computed by:

$$q_{bs} = \rho_a m_{bs} U_h \tag{6.11}$$

where $U_h$ [m s$^{-1}$] is the horizontal wind velocity. In the near-surface region (fine mesh), $U_h$ is assumed to follow a logarithmic profile, function of the friction velocity and roughness length. Following Gerber et al. (2023), the mass flux is assumed to be constant below the lowest fine mesh grid point (0.2 m) and equal to the value computed by the model at that height. An alternative option consists of integrating equation 6.5 from the lower end of FC1 up to a height of 0.2 m. Similar results are obtained with these two options.

## 6.4   Results and discussion

In this section, the simulation results are presented and compared to the field measurements performed at D17. The analysis of the meteorological variables and the blowing snow mass

flux obtained with the 1-year standard simulation is presented in sections 6.4.1 and 6.4.2, respectively. In section 6.4.3, the results of the sensitivity study (simulations S1-S4) are presented and discussed.

## 6.4.1  Meteorological variables

The time series of the 30-minute averaged surface pressure, potential temperature, 2-m horizontal wind velocity, wind direction and 2-m relative humidity w.r.i. obtained from the measurements and the 9-km and 3-km resolution simulations, d1 and d2, respectively, at D17 are presented in Figure 6.1. Only the results for the month of July 2015 are presented to ease the comparison. The mean absolute error (*mae*) between the simulation results and the measurements is computed for all variables (except wind direction) considering the full 1-year time series. The values of *mae* obtained for each simulation domain are shown in the upper left corner. On the right-hand side of the figure, the probability density functions (PDFs) obtained from the 1-year time series of the measurements and simulations at D17 are presented for each variable.

From comparing the simulation results with the measurements, it can be seen that the model correctly captures the meteorological conditions recorded at the station and that the increase in horizontal resolution from 9 to 3 km leads to an improved agreement. For example, the time evolution of the surface pressure is well captured by the model (Figures 6.1a-b). Regarding this particular variable, the horizontal resolution has a negligible effect on the time series and PDFs, but a slight decrease in the *mae* can nevertheless be seen from d1 to d2. Regarding the potential temperature (Figures 6.1c-d), a good agreement between simulations and measurements is also observed. The agreement improves with an increase in horizontal resolution, leading to a reduction in the cold bias seen mainly in the coarser domain (d1). As expected, during austral summer, diurnal patterns can be distinguished in both the potential temperature and the wind velocity time series (see Figure B.1 in Appendix B).

The near-surface wind velocity field is highly influenced by the underlying topography and, therefore, by the model spatial resolution. The 2-m horizontal wind velocity (Figures 6.1e-f) obtained with both domains does not fully capture the variability seen in the measurements, in particular the local maximums and minimums. Nevertheless, an improvement is seen with the increase in horizontal resolution from 9 to 3 km, mainly in capturing the local maximums of wind velocity. As a result, for the highest wind velocities, the PDFs from d2 and the measurements are highly correlated, while the PDF from d1 is significantly narrower than the one from the measurements. To improve the comparison, a higher spatial resolution might be needed. Furthermore, the wind velocity is a function of the roughness length, $z_o$, which is set to a constant value in the simulations. However, due to the formation of surface features, the snow surface roughness is highly dynamic. In this way, an improved representation of the roughness length is also required to improve the agreement between model and measurements (Amory et al., 2017).
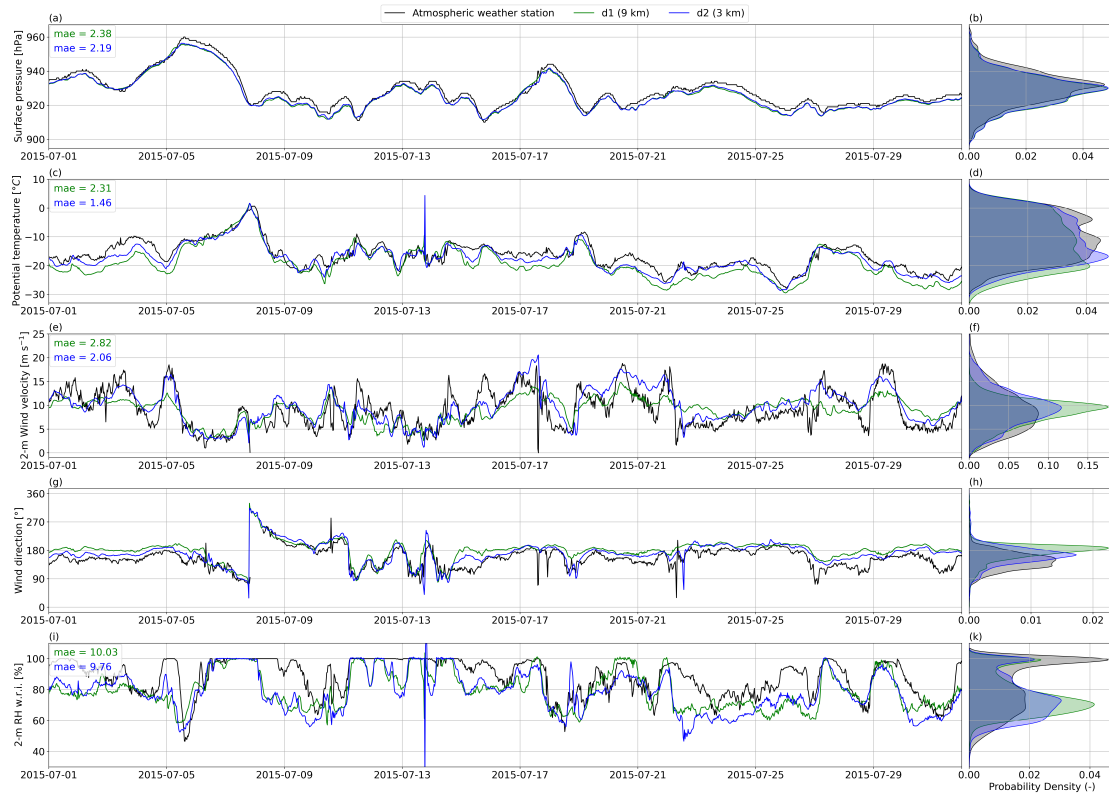
Figure 6.1: Time series of 30-mnt averaged surface pressure (a), 2-m potential temperature (c), 2-m horizontal wind velocity (e), wind direction (g), and 2-m relative humidity w.r.i. (i) obtained from the atmospheric weather station at D17 and the 9-km and 3-km resolution simulations at D17, d1 and d2, respectively (July 2015). Results obtained with the standard settings. On the upper left corner of each time series, *mae* indicates the mean absolute error regarding the full simulation time period (1 September 2014 - 1 September 2015) obtained for each variable and for each domain. The probability density functions obtained from the 1-year time series of the measurements at D17 and the simulations are presented for each variable on the right-hand side of each time series (b, d, f, h, k).

Regarding the wind direction (Figures 6.1g-h), a slight bias towards South can be seen in the simulations compared to the measurements. This shift is less pronounced when considering a higher horizontal resolution (d2). In addition, in the results from d2, a higher wind direction variability can be seen, which is more in agreement with the measurements. The agreement between the simulated and measured RH w.r.i. is especially challenging, particularly during austral winter (Figure 6.1i). A better agreement can be seen during the summer season (Figure B.1) and, overall, a reasonable agreement is seen in the year-round PDF (Figure 6.1k). The increased horizontal resolution leads to both an improvement in the PDF and in the *mae*.

In Figure 6.2, the comparison between measurements and simulation results at D17 during the entire simulation time period is presented in a scatter plot. Except for the wind direction, all remaining variables presented in Figure 6.1 are depicted. The results of both the parent domain and the nest are presented for comparison. The correlation coefficient, $r$, is computed for each simulation domain and presented in the upper left corner.

As previously seen in Figure 6.1, a good agreement between the model and the measurements
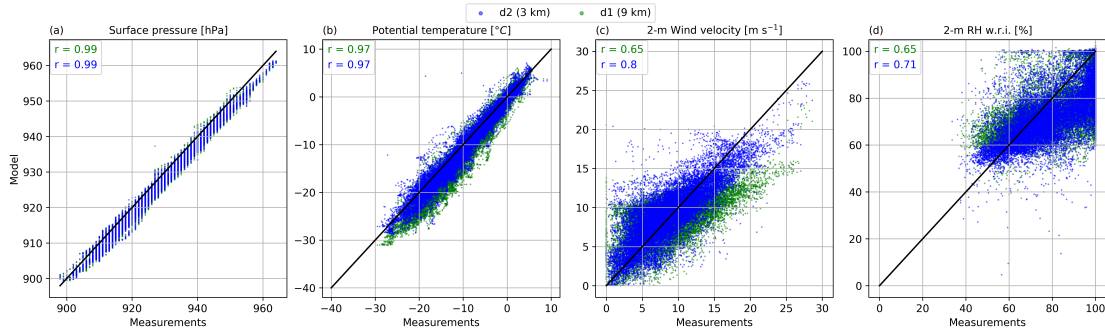
Figure 6.2: Modeled vs measured correlation scatter plots for surface pressure (a), 2-m potential temperature (b), 2-m horizontal wind velocity (c) and 2-m relative humidity w.r.i. (d) at D17. The data points correspond to the 30-minute averaged simulated/measured values at D17 obtained between 1 September 2014 and 1 September 2015 from both the parent (d1) and the nest (d2). Results obtained with the standard settings. In the upper left corner, $r$ denotes the correlation coefficient computed for each simulation domain.

is observed for the surface pressure and the potential temperature (d2: $r = 0.99$ and $r = 0.97$, respectively). On the contrary, the correlation between the modeled and measured 2-m wind velocity and RH w.r.i. is not as high. Moreover, the influence of domain resolution is more significant for these two quantities. For example, regarding the 2-m wind velocity, the increase in horizontal resolution leads to an increase in $r$ from 0.65 to 0.8. In general, the results obtained are in agreement with what was found by Sharma et al. (2023) and Gerber et al. (2023) for coarser resolutions.

### 6.4.2   Blowing snow events

The time series of the 30-minute averaged 2-m horizontal wind velocity and lower and upper FlowCapt transport rates, $Q_{FC1}$ and $Q_{FC2}$, respectively, obtained from the measurements and the high-resolution simulation (d2) at D17 are presented in Figure 6.3. The results from November 2014 and July 2015 are presented to illustrate the time evolution during the summer and winter seasons. The occurrence of snowfall with a minimum intensity of 0.025 mm of water equivalent (w.e.) is indicated by the vertical bars.

From the time series presented in Figure 6.3, it is clear that the wind velocity as well as the frequency and intensity of blowing snow events are greater in July 2015 compared to November 2014. Indeed, during the winter months, D17 (as well as most of the East Antarctic coast) is subjected to strong katabatic winds that develop from the plateau towards the coast. Moreover, during summer, additional heat fluxes reaching the snow cover enhance the formation of ice bonds between the snow grains, which leads to an increase of the fluid threshold and prevents the occurrence of snow transport.

During November 2014, the lower FlowCapt was significantly buried in the snow (exposed height of approximately 0.4 m). It can be seen that the model fails to predict the occurrence of blowing snow during the second half of the month (Figure 6.3b-c). This is partly related to the
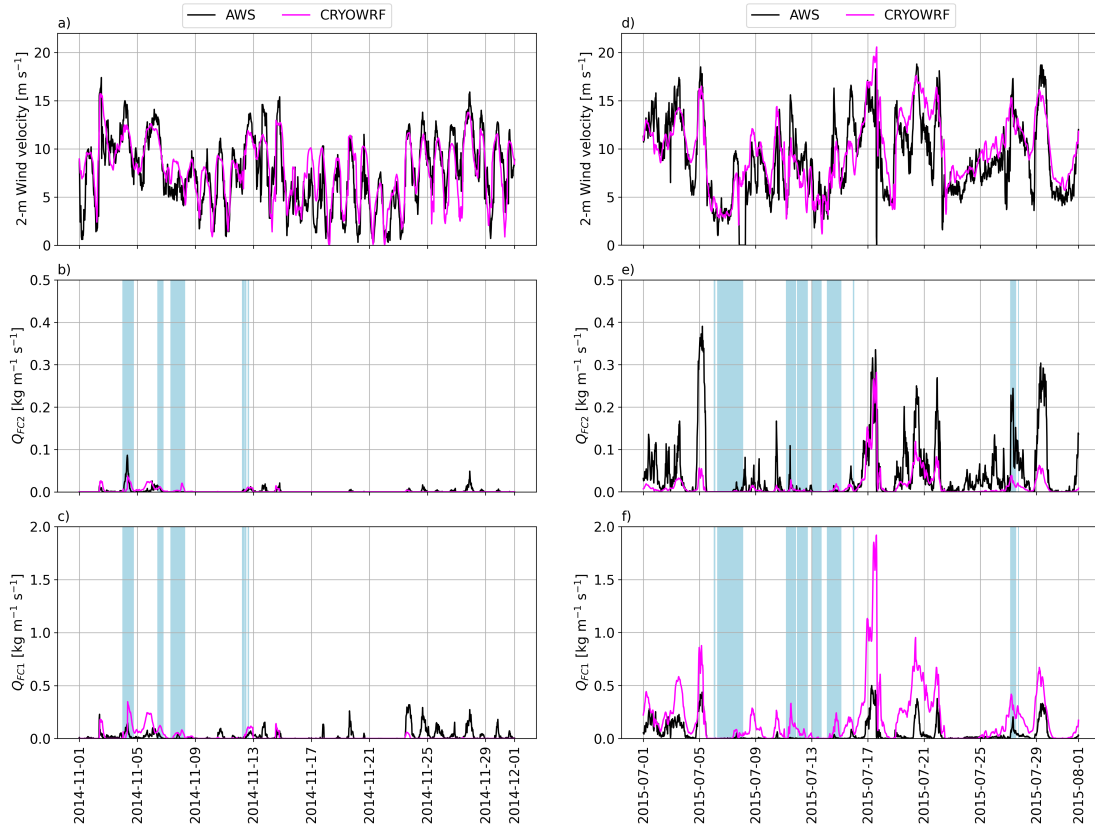
Figure 6.3: Time series of 30-minute averaged 2-m horizontal wind velocity (a and d), upper FlowCapt transport rate (b and e) and lower FlowCapt transport rate (c and f) obtained from the automatic weather station and the 3-km resolution simulation at D17. Results obtained with the standard settings. The panels on the left correspond to the month of November 2014, while the panels on the right correspond to the month of July 2015. The vertical bars on the middle and lower panels indicate the occurrence of snowfall events with a minimum intensity of 0.025 mm w.e.

inability of the model to capture the maximum wind velocities during this time period (Figure 6.3a), but it is probably also related to an overestimation of the fluid threshold. Nevertheless, the model is able to correctly predict the order of magnitude of $Q_{FC1}$ and $Q_{FC2}$ for the events it simulates in the first half of the month (Figure 6.3b-c). This is related to the occurrence of snowfall and therefore to a decrease in the fluid threshold. Similar conclusions can be drawn from the analysis of other summer months (December 2014, January, and February 2015). However, from January 2015 onward, an underestimation of $Q_{FC2}$ starts to be visible. This feature remains clear until the end of the simulation time period and can be observed for most of July 2015 (Figure 6.3e).

The main difference between 2014 and 2015 is the height of the FlowCapt sensors. At the end of December 2014, the two FlowCapt sensors were manually lifted so that the lower ends of FC1 and FC2 were located at 0.1 and 1.2 m above the snow surface, respectively. Therefore, while during September to December 2014, the lower end of FC2 was located at an average height

of 0.5 m, between February and August 2015 the lower end of FC2 was located at an average height of 0.94 m (FC1 became progressively buried in the snow after mid-February 2015). The agreement between model and measurements of $Q_{FC2}$ within 0.5 and 1.5 m height and the underestimation of the same quantity between approximately 1 and 2 m height suggest an overestimation of the modeled decay of the mass mixing ratio with height. This can be related to an overestimation of the particle diameter in suspension or to an underestimation of the turbulence diffusivity coefficient.

Unlike for November 2014, for July 2015, the model consistently overestimates the transport rate over the lower FlowCapt (Figure 6.3f). Part of the overestimation can be linked to an overestimation of the wind velocity (e.g., 17 and 19-22 July 2015), but it is also visible during times of underestimation of the wind velocity (e.g., 1-5 and 29-30 July 2015) (Figure 6.3d). Similar results can be found in most winter months (March-August 2015). During September and October 2014, episodes of mass flux overestimation are less frequent, and a reasonable agreement is obtained between modeled and measured values of $Q_{FC1}$ (see Figure B.2 in Appendix B). As discussed in the next paragraph, the improved results seen during these months might be related to the overestimation of the fluid threshold, which reduces the estimated mass flux in saltation (note the factor $u_*^2 - u_{*,s}^2$ in equation 6.2 and recall that $u_{*,s}$ is approximated by $u_{*,ft}$).

As discussed previously, the onset of snow transport (or, more precisely, snow saltation) occurs when the surface shear stress is greater than the fluid threshold, $\tau_{ft}$. In the model, $\tau_{ft}$ is computed with equation 6.1, as a function of the snow surface characteristics. This quantity is, however, difficult to measure experimentally. Moreover, the criteria that must be met for a granular bed to be considered in saltation are still debatable (see, for instance Pähtz et al., 2020). When assessing the onset of snow transport, Amory (2020) has neglected the FlowCapt measurements lower than $10^{-3}$ kg m$^{-2}$ s$^{-1}$. This was done in order to remove possible perturbations in the signal and to ensure that actual snow drift was being detected. The selected threshold value is based on visual observations made in Adélie Land (Amory et al., 2017). To compare the modeled and measured 2-m wind velocity for saltation onset, the same approach is followed in this work and both the modeled and measured values of $Q_{FC1}$ lower than $10^{-3}$ kg m$^{-1}$ s$^{-1}$ are set to zero. In this way, the modeled/measured 2-m wind velocity that leads the transport rate to increase above $10^{-3}$ kg m$^{-1}$ s$^{-1}$ is used as a measure of snow transport initiation. Let us denote it as the 2-m threshold wind velocity.

In Figure 6.4, the measured and modeled monthly averaged 2-m threshold wind velocity is presented for the entire simulation time period. The vertical bars correspond to two times the standard deviation. Additionally, the measured and modeled monthly averaged 2-m wind velocity is presented for comparison. It can be seen that the measured 2-m average and threshold wind velocities have a clear seasonal trend. While during January and February 2015 the measured 2-m threshold wind velocity reaches an average value of 9 m s$^{-1}$, during the rest of the year it is lower and approximately equal to 6 m s$^{-1}$. On the contrary, the measured 2-m average wind velocity is higher during the winter months than during the summer months, as
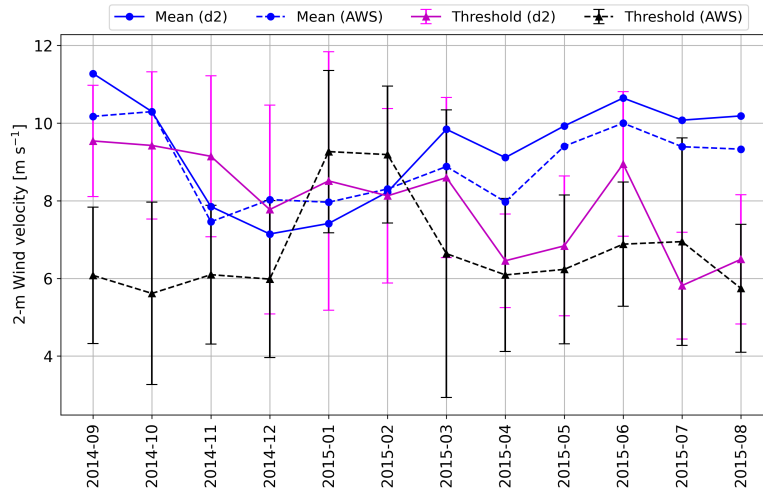
Figure 6.4: Monthly averaged 2-m wind velocity and 2-m threshold wind velocity obtained from the automatic weather station and the 3-km resolution simulation at D17. Results obtained with the standard settings. The vertical bars represent two times the standard deviation. The 2-m threshold wind velocity is computed taking into account a transport rate threshold of $10^{-3} \, \mathrm{kg \, m^{-1} \, s^{-1}}$.

previously discussed. From the comparison between these two quantities, the seasonality of blowing snow is clear: during winter, the low threshold and the high wind velocities lead to the frequent occurrence of high intensity events; during summer, the occurrence of blowing snow becomes scarce and of low intensity due to the low wind velocities and the high threshold for saltation onset.

On average, the model seems to overestimate wind velocity during the winter season and to underestimate it during the summer season. During winter, this is mainly due to an overestimation of the minimum wind velocities (Figure 6.3d), while in summer, the underestimation of the wind speed is mainly linked to an underestimation of the maximum wind velocities (Figure 6.3a). Regarding the 2-m threshold wind velocity, a reasonable agreement between model and measurements is obtained between January and August 2015. During this time period, some underestimation/overestimation of the model can be seen, but the deviation between the mean values is not considered significant taking into account the large standard deviation of the measurements. Differently, during the months of September to December 2014, a significant overestimation of the 2-m threshold wind velocity is observed. In September and October 2014, this disagreement does not lead to an underestimation of the frequency of occurrence of blowing snow because the average 2-m wind velocity is sufficiently high for snow transport to occur nonetheless. However, in November and December 2014, a significant underestimation of the number of blowing snow events is observed as previously discussed (Figure 6.3c).

### 6.4.3 Sensitivity analysis

In this section, the results of the sensitivity simulations listed in Table 6.1 are presented and compared to the results obtained with the standard parameterizations. In order to understand the effect of each parameterization on the final results, the average vertical profiles of mass mixing ratio and mass flux along the fine mesh (0.2-5 m a.g.l.) obtained with the standard simulation and simulations S1 to S4 at D17 on 17 July 2015 00:00 UTC are presented in Figure 6.5. The mass mixing ratio and mass flux specified at the lower boundary ($z_{LB}$) are also presented in all plots. The vertical profiles of mass mixing ratio are fitted to a power law of the type $az^{-b}$, where $z$ is the height above the surface and $a$ [kg kg$^{-1}$] and $b$ are the fit coefficients (Figures 6.5a, c, e, g). The particle mass flux in saltation (equation 6.5) is added to the figures that depict the vertical mass flux of blowing snow particles (Figures 6.5b, d, f, h). At the time stamp considered, the following values of friction velocity, fluid threshold friction velocity, and air density at the lowest WRF level are obtained with the standard simulation: $u_* = 0.95$ m s$^{-1}$, $u_{*,ft} = 0.21$ m s$^{-1}$, $\rho_a = 1.29$ kg m$^{-3}$. Very small deviations from these values are obtained with simulations S1 to S4.

As expected, a decrease in the average particle diameter specified at the lower boundary leads to a modification of the slope of the vertical profile of mass mixing ratio (Figure 6.5a). Indeed, when considering an equilibrium between turbulent diffusion and downward settling of particles, the vertical profile of mass mixing ratio is expected to follow a power law of the type $az^{-b}$, in which the exponent $b$ is proportional to the particle terminal fall velocity (e.g., Budd, 1966; Gordon & Taylor, 2009). Taking into account that the terminal fall velocity decreases with decreasing particle diameter, the mass mixing ratio will decrease with height at a lower rate when considering a lower average particle diameter at $z_{LB}$. Of course, an increase in the mass mixing ratio leads to an increase in the particle mass flux (Figure 6.5b). Therefore, this configuration leads to an even stronger overestimation of $Q_{FC1}$ during the month of July 2015. From Figure 6.5b, it can be seen that both the standard configuration and the simulation S1 lead to a greater mass flux in suspension than in saltation, which is not in agreement with both field measurements (e.g., Nishimura & Nemoto, 2005) and numerical simulations (Figure 4.7b).

In Figures 6.5c-d, the influence of the particle horizontal velocity specified at the lower boundary on the vertical profiles of mass mixing ratio and mass flux is presented. While the use of equation 6.7 yields a particle velocity of 0.6 m s$^{-1}$ at the current time stamp, equation 6.9 estimates a particle horizontal velocity of 6.6 m s$^{-1}$ at $z_{LB}$. Naturally, this difference of one order of magnitude in particle velocity leads to a decrease of the mass mixing ratio by one order of magnitude (equation 6.8). As expected, the slope of the mass mixing ratio profile is kept unchanged and only a shift towards lower values is observed. This leads to a significant decrease in the mass flux in suspension (Figure 6.5d) and therefore to a significant underestimation of $Q_{FC1}$ compared to measurements during July 2015.
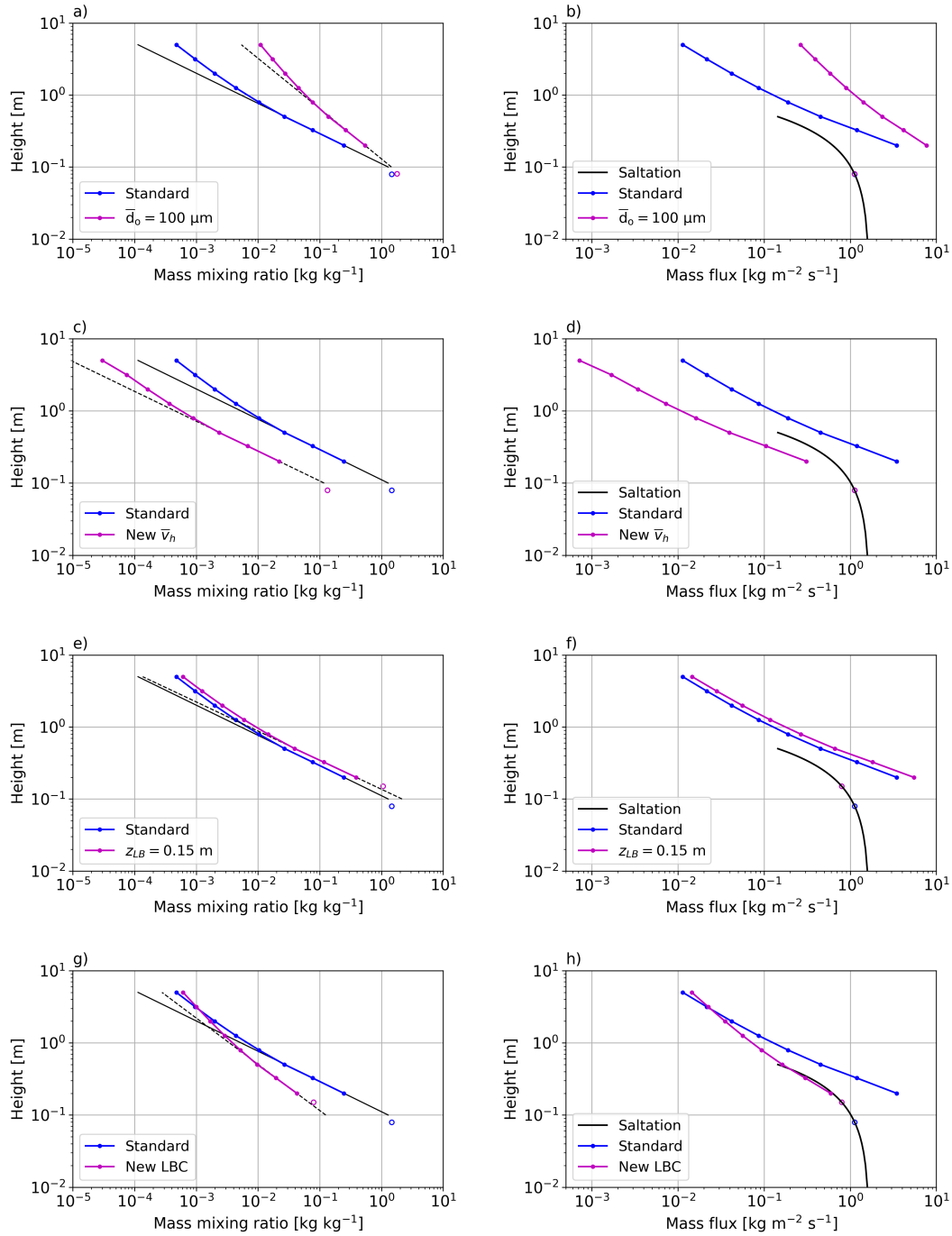
Figure 6.5: Average vertical profiles of mass mixing ratio and mass flux in the first 5 m a.g.l. at D17 on 17 July 2015 00:00 UTC. The results obtained with simulations S1 (a-b), S2 (c-d), S3 (e-f) and S4 (g-h) are compared with those obtained with the standard settings. The mass mixing ratio and mass flux specified at the lower boundary are indicated by the empty circles. On the left-hand side figures, the black lines indicate a fit of the mass mixing ratio to a power law. On the right-hand side figures, the vertical profile of mass flux in saltation is also presented for comparison.

According to equation 6.4, when the friction velocity is equal to 0.95 m s$^{-1}$, the lower boundary condition is specified at a height of 0.08 m. In Figures 6.5e-f, the effect of fixing $z_{LB}$ to 0.15 m height is analyzed. Taking into account that the mass flux in saltation is assumed to decrease with height according to an exponential decay (equation 6.5) and that the particle horizontal velocity is assumed constant in height (equation 6.7), the mass flux and mass mixing ratio specified at 0.15 m are lower than the values imposed at 0.08 m (Figures 6.5e-f). However, since the mass mixing ratio specified at $z_{LB} = 0.15$ m is higher than the mass mixing ratio obtained with the standard configurations at the same height (the fit to the power law is used to estimate the mass mixing ratio below 0.2 m), an increase in the mass mixing ratio and mass flux in suspension is actually obtained with simulation S3.

Overall, as long as the numerical mesh is sufficiently discretized, the vertical profile of mass mixing ratio in a log-log graph will not deviate significantly from a straight line crossing the point ($m_{bs_o}, z_{LB}$), independently of the height at which the lower boundary of equation 6.3a is specified. In fact, its slope is solely dependent on the terminal fall velocity and turbulence diffusivity. Considering that the mass mixing ratio in saltation is expected to follow an exponential decay with height and not a power law (see section 2.3.1), it is clear that the application of equations 6.3a-b inside the saltation layer will lead to erroneous vertical profiles of mass and number mixing ratios in suspension.

In simulation S4, both $z_{LB}$, $\bar{d}_o$ and $\bar{v}_h$ are modified in comparison to the standard settings. The alternative set of parameterizations considered in simulation S4 solves part of the model inconsistencies discussed in section 6.1.2. The results obtained with this simulation are presented in Figures 6.5g-h. It can be seen that the increase in particle horizontal velocity leads to a significant reduction in $m_{bs_o}$ and that decreasing $\bar{d}_o$ leads to a reduction in the slope of the mass mixing ratio profile (Figure 6.5g). Above 1 m height, the results obtained with simulation S4 do not deviate significantly from those obtained with the standard configuration. However, below 1 m height, lower values of mass mixing ratio and mass flux are obtained. Furthermore, the mass flux in suspension becomes more consistent with the mass flux profile specified in the saltation layer and with the trends observed in the literature (Figure 6.5h).

In Figure 6.6, the time series of the 30-minute averaged 2-m horizontal wind velocity and lower and upper FlowCapt transport rates presented in Figure 6.3 for the month of July 2015 are again depicted and compared to the results obtained in simulation S4. It can be seen that the new set of parameterizations solves the model overestimation of $Q_{FC1}$ and significantly improves the comparison with the FlowCapt measurements (Figure 6.6c). Some differences between model and measurements can nevertheless be observed, but they are highly correlated with the underestimation/overestimation of the wind field (Figure 6.6a). The transport rate over the upper FlowCapt, $Q_{FC2}$, is still considerably underestimated by the model (Figure 6.6b). As discussed in the previous paragraph, between 1 and 2 m height, the mass flux obtained with the standard and new configuration is of the same order of magnitude. An improved agreement can possibly be obtained by adjusting the average particle diameter and the turbulence diffusivity coefficient. However, a more detailed analysis of these two quantities is required to
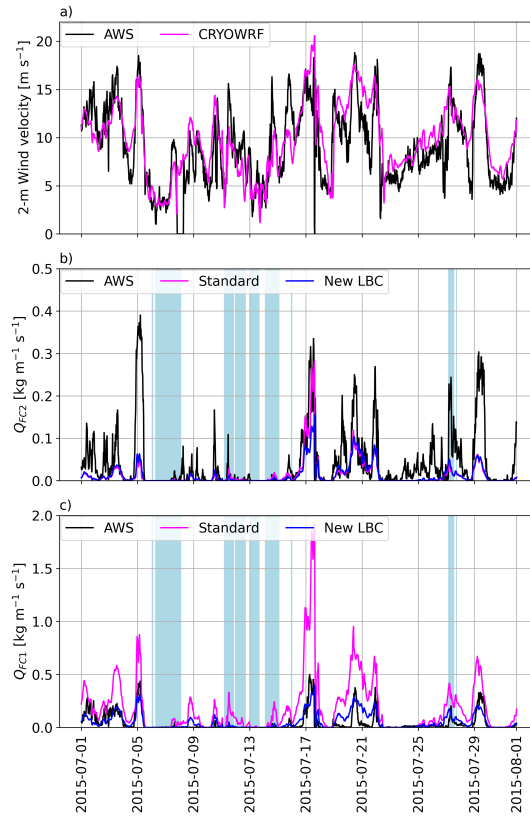
Figure 6.6: Time series of 30-minutes averaged 2-m horizontal wind velocity (a), upper FlowCapt transport rate (b) and lower FlowCapt transport rate (c) obtained from the atmospheric weather station and the 3-km resolution simulation at D17 for the month of July 2015. Both the time series obtained with the standard settings and simulation S4 are presented. The vertical bars on the middle and lower panels indicate the occurrence of snowfall events with a minimum intensity of 0.025 mm w.e.

guarantee that the values are kept within an acceptable range.

## 6.5   Conclusions

In this chapter, the capabilities of the CRYOWRF model to estimate the onset and intensity of blowing snow events were assessed. To this end, CRYOWRF simulations were performed in the region around Dumont d'Urville, in coastal Adélie Land, from September 2014 to September 2015. The computational domain includes the automatic weather station D17, from which continuous measurements of different meteorological quantities are available during the full simulation time period.

When comparing simulation results with field measurements, it can be seen that the model is able to successfully simulate the meteorological conditions at D17, in particular the surface pressure, potential temperature, and wind velocity. The agreement between simulations and measurements improves when the horizontal grid resolution is increased from 9 to 3 km. The effect of grid resolution is particularly noticeable on the time series of the 2-m wind

velocity, which highlights the importance of grid resolution to correctly simulate the processes of snow transport and sublimation. Notwithstanding, the finer resolution of 3 km is not able to fully capture the variability seen in the measurements, in particular the maximum and minimum wind velocities. Taking into account that the mass flux of blowing snow particles scales approximately with $u_*^3$, the mismatch between modeled and measured wind velocities must be taken into account in the direct comparison between the modeled and measured transport rates. Improvements in the near-surface wind field might only be obtained with an increase in horizontal resolution and a better representation of the spatial and temporal evolution of the roughness length.

The ability of the CRYOWRF model to simulate the mass flux in suspension is evaluated by comparing the vertically integrated mass flux against FlowCapt measurements in the first 2 m a.g.l. It can be seen that the model is able to capture the seasonality of blowing snow, which is related to the magnitude of the wind velocity and the value of the threshold for the onset of saltation. Overall, during winter, snow transport events are very frequent and of high intensity due to the high wind velocity and the low fluid threshold. During summer, snow transport is more rare and of low intensity due to the low wind velocity and the high fluid threshold. However, during summer, the model underestimates the frequency of occurrence of blowing snow due to the overestimation of the fluid threshold. This can be due to the fluid threshold parameterization itself or to a misrepresentation of the snow surface characteristics at D17. Therefore, a detailed analysis of the simulated snow cover is needed to further investigate this issue.

From the analysis of the physical model implemented in CRYOWRF, it is concluded that the modeling of the saltation-suspension interface is not fully consistent with the premises behind the saltation and suspension models themselves. For instance, taking into account that the advection-diffusion equations represent the interplay between particle settling and turbulence diffusion, characteristic of particles in suspension, they are not valid close to the surface, but only above approximately 0.1 m height. Indeed, close to the surface, the particle mass flux is defined by an exponential decay, which is characteristic of the motion of particles in saltation. Therefore, the use of this expression in the first 0.1 m above the surface cannot yield a good estimate of the mass flux transported in suspension. An improved representation of the saltation-suspension interface is obtained by specifying the lower boundary at a height of 0.15 m, where both the advection-diffusion equations and the exponential decay can be considered approximately valid.

In addition, from the comparison between the parameterizations used and the conclusions drawn in the previous chapters, it is concluded that the expression used for the particle horizontal velocity considerably underestimates the particle velocity above 0.015 m height. In this way, an alternative parameterization is proposed, which guarantees that the particle horizontal velocity is within the range of values observed in the literature.

By changing the height of the lower boundary condition, the particle horizontal velocity,

and the average particle diameter, the comparison between simulation results and FlowCapt measurements improves significantly for the month of July 2015. However, between 1 and 2 m height, both this new set of parameterizations and the standard configuration lead to an underestimation of the particle mass flux in comparison to the FlowCapt measurements. Further investigation is needed in order to understand this disagreement, both regarding the accuracy of the turbulence diffusivity and the terminal fall velocity, as well as regarding the uncertainty of the FlowCapt measurements.

The study carried out in this chapter highlights the importance of the lower boundary condition for snow suspension, which is typically overlooked in the development of blowing snow schemes. The mass mixing ratio of particles in suspension decreases with height following approximately a power law. Therefore, the value specified at the lower boundary specifies the maximum value of the mass mixing ratio. Taking into account the importance of the lower boundary condition on the vertical profiles of mass mixing ratio and mass flux of blowing snow particles, further investigation on the details of the saltation system and the saltation-suspension interface (vertical profiles of mass flux, concentration, velocity and particle size distribution) is needed to improve the parameterizations used. Experimental studies developed with natural snow are of particular importance for deepening our understanding of the phenomenon and to validate detailed numerical models which revealed to be essential for the complete study of the particle-wind-bed interactions.

In order to assess the performance of large-scale numerical models such as CRYOWRF, continuous measurements of blowing snow mass flux, as those considered in this study, are of the utmost importance. Taking into account the large vertical gradients of particle mass flux and concentration in the first 2 m a.g.l., the use of vertically averaged mass flux measurements seems to be preferable for large-scale model validation in comparison to single-point measurements (e.g., SPC). However, as previously mentioned, further efforts are still needed to assess the uncertainty of the FlowCapt sensor. At D47, an AWS located at an elevation of 1560 m a.s.l. and 100 km further inland than D17, similar FlowCapt measurements are also available between 2010 and 2012 (Amory, 2020). This data set can be used to further assess the new set of parameterizations proposed in this work.

The fact that CRYOWRF couples the capabilities of WRF with those from the detailed snow model SNOWPACK makes CRYOWRF ideal for investigating the effect of snow transport and sublimation at large scales. The use of SNOWPACK as the land-surface model of WRF makes it possible to envision a tighter coupling between the snow surface characteristics and the snow saltation parameterizations, which are expected to influence not only the onset of snow transport, but also the intensity and dynamics of snow saltation. Future developments in understanding the effect of the snow surface characteristics on the saltation dynamics can easily be incorporated in CRYOWRF and, therefore, further improve the estimates of blowing snow transport and sublimation.

# 7 Conclusions and perspectives

The cold and snow-covered regions on Earth influence the global climate system, are home to a broad range of species, and are a source of fresh water for many communities worldwide. However, they are today endangered ecosystems, strongly affected by global warming and climate change. These facts strengthen the need to improve our understanding of the geophysical phenomena that control snow-covered regions and ice sheet dynamics. In particular, the importance of snow transport events to the mass and energy balances of snow-covered regions has long been acknowledged by the scientific community. Several atmospheric and snow models are currently enriched with blowing snow schemes that represent the aeolian transport of snow and quantify the induced changes in snow height and the amount of snow sublimation. However, the correct assessment of these quantities remains a challenge. This is due to the complexity of the phenomenon, the adverse environmental conditions for field observations, the uncertainties in the parameters that control blowing snow transport and sublimation, but also due to inaccuracies in the blowing snow schemes themselves.

In order to contribute to an improved representation of snow transport in large-scale models, this thesis focuses on the dynamics of snow saltation - the hopping of snow particles close to the surface. Snow saltation is a sub-grid process in these models and is, therefore, parameterized. Despite their simplicity, parameterizations can produce satisfying results if the underlying assumptions are valid and the dominant phenomena are properly quantified. From the analysis of snow saltation parameterizations used in atmospheric models, we found two main caveats: first, the effect of the snow surface characteristics and its variability on the different quantities of interest is highly simplified; second, the models are based on inconsistent assumptions regarding the scaling of the near-surface particle velocity with the friction velocity outside the saltation layer (henceforth friction velocity). With respect to this second point, parameterizations based on the assumption that the near-surface particle velocity scales with the friction velocity, and others that assume that this same quantity is invariant with respect to the friction velocity can be found in the same snow transport model.

In order to investigate these issues, a Large Eddy Simulation flow solver coupled with a Lagrangian stochastic model (LES-LSM) was used. This model revealed to correctly reproduce

99

the main characteristics of the saltation system observed in previous models and measurements. Moreover, it proved to be a very important tool for the systematic analysis of this complex phenomenon.

The simulations showed that the snow surface characteristics play an important role in the snow saltation dynamics. The snow surface characteristics significantly influence the mass flux in saltation, especially at high friction velocities. In addition, they control some near-surface quantities, such as the surface shear stress during saltation and the near-surface particle velocity. In atmospheric models, there is one single parameter that is explicitly specified as a function of the snow surface characteristics: the surface shear stress that leads to the onset of snow saltation (denoted fluid threshold). This quantity is assumed to be equal to the surface shear stress during saltation and is used to compute both the near-surface particle velocity and the particle mass flux. However, neither the empirical coefficients used to compute these last variables nor their scaling with the friction velocity change with the snow surface characteristics. Moreover, the simulation results presented in this work and the different experimental and numerical studies available in the literature do not fully agree on the scaling of the surface shear stress with the friction velocity, nor on its relation to the fluid threshold. Finally, it is not clear whether this single parameter is sufficient to correctly characterize the effect of the snow surface characteristics on the quantities of interest in large-scale models.

Using the LES-LSM model, we have shown that, depending on the snow surface characteristics and the respective aerodynamic entrainment, rebound, and splash parameters, the snow saltation dynamics can be characterized by two regimes: one dominated by aerodynamic entrainment and the other by splash, depending on the friction velocity. This finding contrasts with sand saltation models, which usually neglect the role of aerodynamic entrainment, but is in agreement with some snow saltation models available in the literature. At low wind velocities, for which snow saltation is dominated by aerodynamic entrainment, the near-surface particle velocity is expected to scale with the friction velocity, while at medium to high wind velocities, snow saltation is dominated by splash and the near-surface particle velocity is expected to be invariant with respect to the friction velocity. Therefore, the parameterization used in some atmospheric models to compute the rate of decrease of particle mass flux with height is only in agreement with a saltation system dominated by aerodynamic entrainment. Thus, it might not be suitable at medium to high friction velocities, for which snow saltation is expected to be dominated by splash.

This detailed study of the saltation system performed with the LES-LSM was then used to assess the blowing snow scheme of CRYOWRF, a coupled atmosphere-snowpack model. By comparing CRYOWRF simulations with field measurements of blowing snow mass flux, we found that the model significantly overestimates the particle mass flux during winter. This issue could largely be solved by improving the scaling of the saltating particles velocity with the wind velocity, which was previously assumed to be invariant with respect to the friction velocity and the height above the surface, and by correcting the region of validity of the equations being employed. For instance, taking into account that advection-diffusion-type

equations are unable to characterize the particle motion in saltation, it is essential to restrict their use to the suspension layer (above approximately 0.1-0.2 m height). The lower boundary condition can nevertheless be provided by a snow saltation model based on the assumption that the exponential decay of the mass flux with height is still a reasonable approximation between 0.1 and 0.2 m above the surface. The analysis performed with CRYOWRF highlights the importance of correctly describing snow transport in the saltation layer, which has strongly motivated our study. Moreover, it strengthens the need for detailed assessments such as those conducted in this thesis. Other atmospheric models that also represent the process of snow transport can equally benefit from the analysis undertaken.

In addition to the snow saltation parameterizations, the selected horizontal grid resolution is also an important factor when simulating snow transport events. It influences the model's ability to correctly represent the friction velocity, which is the dominant parameter controlling the intensity of snow transport. This poses a challenge to large-scale simulations, which typically employ relatively coarse grids. The correct modeling of the frequency of snow transport events is also an important aspect in large-scale simulations. CRYOWRF is able to correctly capture the seasonality of blowing snow, but overestimates the fluid threshold, especially during the summer months. Therefore, further studies are needed to better simulate this quantity. Different equations are available in the literature, but they are typically tailored for a specific snow model. Therefore, they are challenging to compare and evaluate outside their respective model.

In this work, we have shown how small-scale numerical simulations can be used to improve our understanding of the saltation system and the parameterizations used in large-scale models. However, in order to fully use small-scale models to upscale the process of snow saltation, the accuracy of the models' inner parameters must be improved. This concerns the particle density, the particle drag coefficient, as well as the parameters used to compute the surface processes of aerodynamic entrainment, rebound and splash. Regarding the particle density, its correct estimation is also relevant for the calculation of particle mass flux using particle counts and the respective particle diameter measured with optical devices. Long-lasting assumptions, such as the use of the density of ice and of the drag coefficient of a sphere, need to be further challenged and investigated. In addition, improvements in the representation of the snow surface characteristics in small-scale models are also necessary, for instance, regarding the effect of interparticle cohesion on the different surface processes. To this end, field and wind tunnel experiments performed with natural snow are much needed. These issues call for modelers and experimentalists to collaborate: while modelers must understand what can be measured and make sure the model parameters are likely to be adjusted; experimentalists should be able to recognize the quantities that the modelers actually need.

The correct prediction of snow transport and sublimation at large scales has a variety of challenges. The full understanding of the processes involved is a multi-disciplinary endeavour, requiring contributions from both atmospheric and snow scientists. In addition to what was already suggested, future developments in this field must include the large-scale assessment

of blowing snow sublimation using the improved blowing snow scheme of CRYOWRF and its comparison with satellite products. Moreover, an extensive comparison between simulations and the existing data sets of blowing snow mass flux and snow height must be performed, for example, concerning the MOSAiC expedition. Finally, more experimental campaigns measuring the vertical profiles of particle mass flux and velocity are much needed to continue improving the numerical models and the assessment of snow transport and sublimation in the polar and high-mountain regions.

# A Wind tunnel experiments of snow saltation

The study presented in this appendix was performed in collaboration with the Research Group Prof. Coletti from ETH Zurich. A manuscript with some of the findings will be submitted for publication:

Petersen, A., Melo, D. B., Lehning, M. and Coletti, F. Experimental assessment of particle lift and drag during snow saltation. In preparation.

DBM and AP performed the wind tunnel experiments. AP performed the PTV analysis and post-processing. DBM processed the snow and air velocity measurements. AP and DBM analyzed the results with contributions from all co-authors. ML and FC established the collaboration, supervised the project and secured its funding. DBM and AP wrote the current version of the text.

## A.1 Introduction

In order to investigate the saltation dynamics and kinematics, wind tunnel experiments based on high-speed imaging of saltating snow were conducted in Davos, Switzerland. The PTV technique is used to detect and track the particles in saltation, which allows the calculation of Lagrangian statistics of particle velocity and acceleration. In addition, using pitot tube pressure measurements to estimate the wind velocity in the near-surface region, the drag and lift forces applied to the saltating snow particles are computed and analyzed. From the analysis of the results, conclusions are drawn regarding the validity of some assumptions made in snow saltation models. The wind tunnel facility and experimental setup are presented in section A.2. The characteristics of the snow cover used in the experiments and the PTV analysis are presented in section A.3. Finally, the main conclusions are summarized in section A.4.

## A.2   Methodology

Wind tunnel experiments using natural snow were performed at the WSL Institute for Snow and Avalanche Research SLF in Davos, Switzerland, during January-February 2022. The wind tunnel is located at 1670 m above sea level, has a cross-section area of 1×1 m$^2$ and a total length of 14 m. Naturally deposited snow is collected in trays after each snowfall and transported to the tunnel without disturbing the snowpack. A total of four trays guarantees a snow cover fetch of 8 m, which is preceded by 6 m of roughness elements (see Figure A.1a). The roughness elements (spikes and leggos) promote a faster growth of the turbulent boundary layer. These facilities have been used in the past to study a variety of snow drift issues, ranging from snow saltation onset to the coupling between wind velocity fluctuations and snow saltation mass flux (e.g., Clifton et al., 2006; Crivelli et al., 2016; Paterna et al., 2016; Walter et al., 2014).

Prior to the experiments, the snow density is measured with a snow density cutter, which is a snow sampler of a well defined volume. Moreover, the penetration resistance of the snow is measured with a SnowMicroPen (SMP) (Schneebeli et al., 1999). The SMP is a penetrometer composed of a rod with a measuring tip. The obtained force signal is a measure of the snow hardness.

A high-speed camera CMOS with macro lens Nikon Micro-Nikkor 200 mm f/4 is used to acquire shadowgraphy images of saltation snow at a frequency of 5 kHz. Backlighting is provided by a LED over a 5×5 cm$^2$ window. The camera is positioned at approximately 6.3 m downstream of the beginning of the snow cover. Slightly downstream of the measurement window, the air stagnation pressure is measured with an array of pitot tubes at a frequency of 20 Hz (Figure A.1b). The pitot tubes are positioned between 2.5 and 10 cm above the snow surface, allowing pressure measurements within the logarithmic layer during saltation. The static pressure is measured with a wall-mounted pressure probe at the same streamwise position as the the



|     (a)     |     (b)     |

Figure A.1: Pictures of the experimental setup portraying the snow cover and the roughness elements (a), as well as the pitot tube array and the high sped camera (b). Note that the pitot tubes are not at the height considered during the experiments. [Photo credit: Alec Petersen]

array of pitot tubes. By neglecting the vertical and crosswise pressure gradients, the measured static pressure is considered representative of the static pressure at the pitot tubes and used to compute the wind velocity at each probe. In addition, a Mini-Air van anemometer is mounted on the mast of the pitot tubes, providing low-frequency (1 Hz) air velocity and temperature measurements. It is placed at 0.6 m height above the snow surface.

A 2D PTV method based on the 4th best estimate algorithm (Ouellette et al., 2006) provided time-resolved particle positions. Particle velocities and accelerations are determined from the particle position using convolution with the first and second derivatives of a Gaussian kernel, following the procedure established by Voth et al. (2002). In addition, the mean diameter, aspect ratio and orientation of all detected particles are estimated by the particle detection algorithm.

## A.3  Results and discussion

Taking into account the need for undisturbed, naturally deposited snow, the number of experiments conducted at the wind tunnel are limited by the meteorological conditions and the number of trays available. There were four days of favorable conditions during the experimental campaign and the best data set was obtained on 2 February 2022. On this day, images for saltating snow were recorded for an average Mini-Air velocity of 7.9, 8.5, 9.1 and 9.4 m s$^{-1}$. For the lowest air velocity, the saltation process was highly intermittent, and for the two highest, the large concentration of particles close to the surface significantly hindered particle detection and tracking. In this way, only the results for the 8.5 m s$^{-1}$ event are presented and discussed.

### A.3.1  Snow properties

On 2 February 2022, a total of 7 cm of snow was collected during 4 hours immediately before the experiments. The falling snow crystals were significantly rounded and the trays were additionally loaded with snow particles that were blown from the roof of the wind tunnel premises. This led to a relatively compact layer of fresh snow. The average snow density measured with the density cutter yielded 93 kg m$^{-3}$.

The Python package *snowmicropyn*[1] is used to process the SMP signal. The averaged and smoothed SMP force signal is presented in Figure A.2a. In Figure A.2b, the snow density derived from the SMP signal is shown. It is computed with the parameterization proposed by Calonne et al. (2020). Before inserting the SMP into the snowpack, some trial measurements were performed without any resistance (air signal). These results are also presented in the figures for comparison. The dashed line highlights the location of the snow surface, as predicted by the post-processing software. The measurements are not performed down to the full depth of the snowpack to avoid the contact of the tip of the SMP with the base of the metal trays.

---

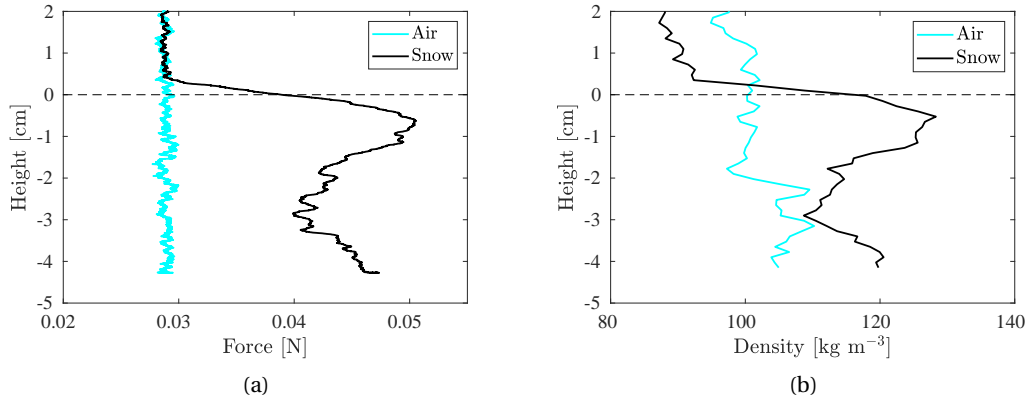[1]https://snowmicropyn.readthedocs.io/en/latest/index.html

Figure A.2: Force signal obtained with the SMP (a) and snow density derived from the parameterization of Calonne et al. (2020) (b). The measurements were performed over the snow cover collected on 2 February 2022. The air signal is also presented as a reference.

As expected, the snow and air signals significantly deviate from each other at the snowpack surface (Figure A.2a). However, this is not always obtained over a layer of fresh snow due to its low density. For instance, when the measurements were performed over a layer of fresh snow with an average manual density of 70 kg m$^{-3}$, a negligible difference was observed between the air and snow signals. In Figure A.2b, it can be seen that the snow density derived from the SMP signal yields an average value of 118 kg m$^{-3}$, which agrees well with the manual measurement of 93 kg m$^{-3}$. However, when considering all the sampled snow layers the lower/higher SMP force signal and the respective snow density do not always correspond to the lower/higher manual snow density measurement. In addition, for two snowpacks with similar manual snow densities (70 and 78 kg m$^{-3}$), considerably different SMP signals are obtained. The weak correlation between manual and SMP density measurements might be related to the weak resistance force sustained by a snowpack of freshly deposited snow. Indeed, in Figure A.2b, the values of density derived from the air and snow signals do not deviate significantly.

During the experimental campaign, relatively similar snow covers were used in the experiments (freshly fallen snow, 1-day and 2-day old snow). Nevertheless, some slight differences in the threshold wind velocity for saltation onset were observed. Future studies, targeting for instance the effect of the snow cover characteristics on the saltation system, might require additional snow measurements to fully characterize the snow cover (e.g., grain type, size, snow temperature and hand hardness index). In addition, the meteorological conditions during snowfall and the experiments themselves might help understanding the behavior of the snow cover when subjected to strong winds. Indeed, the results show that snow density and SMP measurements alone might not be sufficient to fully characterize lightly compacted snowpacks.

The particle size distribution of the particles in saltation is presented in Figure A.3. The particle diameter is obtained by fitting an ellipse to all detected particles and by computing the average
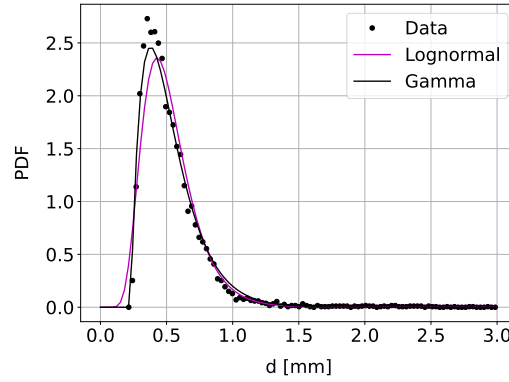
Figure A.3: Probability density function (PDF) of the snow particles diameter. Particles detected in a 5×5 cm$^2$ window on 2 February 2022, for a Mini-Air average velocity of 8.5 m s$^{-1}$.

between the two axis of the fitted ellipse. The size distribution shows good agreement with both a 2-parameter Gamma distribution (typically obtained in field experiments, e.g., R. A. Schmidt, 1982), as well as a lognormal distribution (assumed in the LES-LSM simulations presented in chapter 4). However, the average diameter (540 $\mu$m) is significantly higher than the values obtained in previous PTV field studies of fresh snow saltation (e.g., 276 $\mu$m in Aksamit & Pomeroy, 2016), as well in field measurements performed with the SPC (e.g., Nishimura & Nemoto, 2005; Nishimura et al., 2014). Similar PDFs are obtained when dividing the saltating particles into 5 vertical bins, which is in agreement with the LES-LSM results obtained below 5 cm height (Figure 4.10).

### A.3.2 Particle velocity and acceleration

In order to compute the average vertical profiles of particle velocity and acceleration, the measurement window is divided into multiple horizontal layers. At each layer, average values of velocity and acceleration are computed considering all tracked particles in the layer.

The average particle velocity and acceleration along the streamwise direction are presented in Figure A.4. The vertical profiles of the upward and downward populations are presented separately to facilitate the analysis. In Figure A.4a, the average wind velocity obtained from the first 4 pitot tubes is presented for comparison. A fit of the average wind velocity profile to a logarithmic function ($u_* = 0.39$ m s$^{-1}$, $z_o = 10^{-5}$ m) is also shown for reference. As expected, the particle streamwise velocity is lower than the wind velocity (Figure A.4a). Moreover, considering that the particles are continuously accelerated by the fluid flow along their trajectories, the downward population is traveling at a higher velocity than the upward population. Similarly to the wind profile, the particle streamwise velocity follows approximately a logarithmic trend with height. These results are in agreement with the findings of Nishimura et al. (2014), who measured the particle velocity of saltating snow in a wind tunnel between 1.5 and 12 cm above the snow surface. However, they differ from the wind tunnel experiments of saltating sand performed by Ho et al. (2011) and Creyssels et al. (2009), who found a linear increase in the
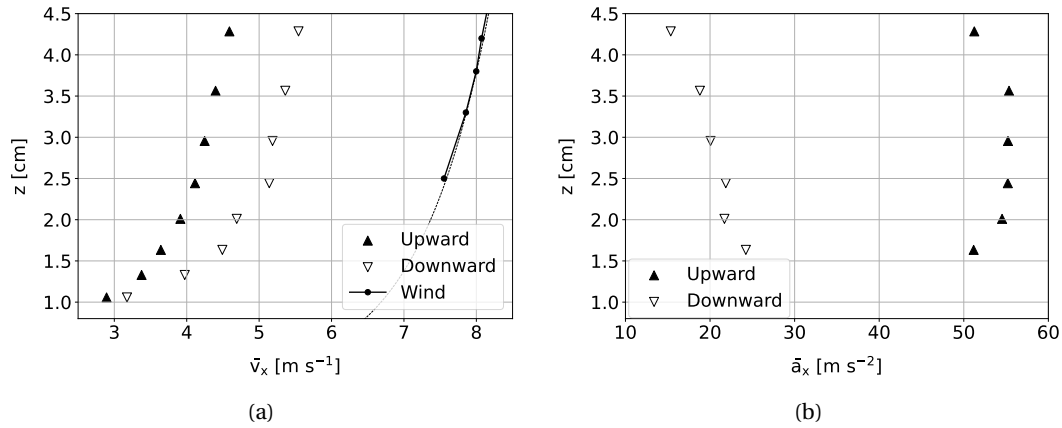
Figure A.4: Average particle velocity (a) and acceleration (b) in the streamwise direction. The vertical profiles of the upward and downward populations are presented separately. In (a), the average wind velocity measured by the lowest 4 pitot tubes is also presented for comparison, together with a fit to a logarithmic function. Results obtained on 2 February 2022, for a Mini-Air average velocity of 8.5 m s$^{-1}$.

particle streamwise velocity with height in the first 3 and 4 cm above the surface, respectively. The particle velocity relative to the time-averaged air velocity (henceforth mean particle relative velocity) in the streamwise direction is higher when the particles are moving upwards than when they are moving downwards. This is clearly visible in the acceleration profiles (Figure A.4b). In fact, the upward population experiences a stronger acceleration in the streamwise direction than the downward population.

The average particle velocity and acceleration along the vertical direction are presented in Figure A.5. The upward population exhibits greater absolute velocities in the vertical direction than the downward population (Figure A.5a). Differently from a ballistic motion only subjected to the gravitational force, the downward moving particles are not able to restore (in modulus) the vertical velocity that they exhibit in their upward motion. This is justified by the stronger acceleration felt by the upward population (in modulus) in comparison with the downward population (Figure A.5b). When the particles are moving upwards, the aerodynamic force has the same direction as the gravitational force and contributes to decelerate them. Differently, when the particles are moving downward, their acceleration in the vertical direction is approximately given by the acceleration of gravity. In summary, the results show that the effect of the vertical component of the aerodynamic force along the upward motion is significant, but it is probably minor along the downward motion. The fact that the aerodynamic forces in the vertical direction are higher during the upward motion in comparison with the downward motion is justified by the fact that the mean particle relative velocity is also higher when the particles are moving upward than downward (recall Figure A.4). In contrast with the measurement results, the vertical component of the aerodynamic force is neglected in the early model of Kawamura (1951). However, in most saltation models, the effect of aerodynamic drag is taken into account in both the horizontal and vertical directions (e.g., Doorschot & Lehning, 2002; Sørensen, 1991).
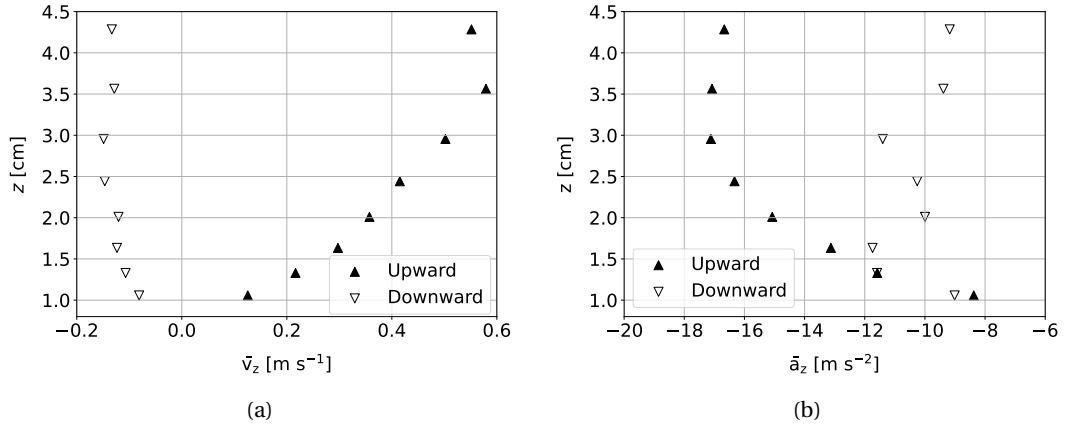
Figure A.5: Average particle velocity (a) and acceleration (b) in the vertical direction. The vertical profiles of the upward and downward populations are presented separately. Results obtained on 2 February 2022, for a Mini-Air average velocity of $8.5 \mathrm{~m~s^{-1}}$.

### A.3.3 Analysis of the drag and lift forces

As previously mentioned, the only measure of the air velocity in the experimental field-of-view comes from pitot tube measurements. These allow us to define a time-averaged log-law profile (see Figure A.4a), which we use to solve for the mean fluid velocity at each snow particle trajectory location, and thus to estimate the mean relative velocity between the snow particles and the time-averaged air velocity. Using the definition of drag and lift as the aerodynamic forces opposing and perpendicular to the relative velocity vector, respectively, and our measurements of snow particle acceleration, we estimate the mean forces felt by each particle over the course of its trajectory. In this analysis, it is assumed that the only forces applied to the particles in saltation are the gravitational and the aerodynamic forces. This assumption was previously discussed in section 2.2.

Figure A.6a shows the mean drag force profiles, normalized by the magnitude of the gravitational force. Both the streamwise ($x$) and vertical ($z$) components in the lab frame-of-reference are presented. In addition, the profiles obtained for the upward and downward populations are presented separately to better visualize how drag acts upon the snow particles during different stages of their trajectories. As expected, upward moving particles are being pushed along by drag as well as pushed downwards. Downward moving particles, which are traveling faster than their upward moving counterparts, experience a smaller drag in the streamwise direction and nearly none in the vertical direction. Figure A.6b shows the same plot, but for the mean lift forces. On average, the lift force is found to be one order of magnitude smaller than the drag force. Regarding the upward moving particles, lift contributes to push them forward in the streamwise direction and slightly counteracts the effect of drag in the vertical direction. The downward moving particles are negligibly affected by lift in the streamwise direction. In the vertical direction, these particles are pushed downwards by lift, which is of the same order of magnitude as the drag force. Therefore, the aerodynamic force in the vertical
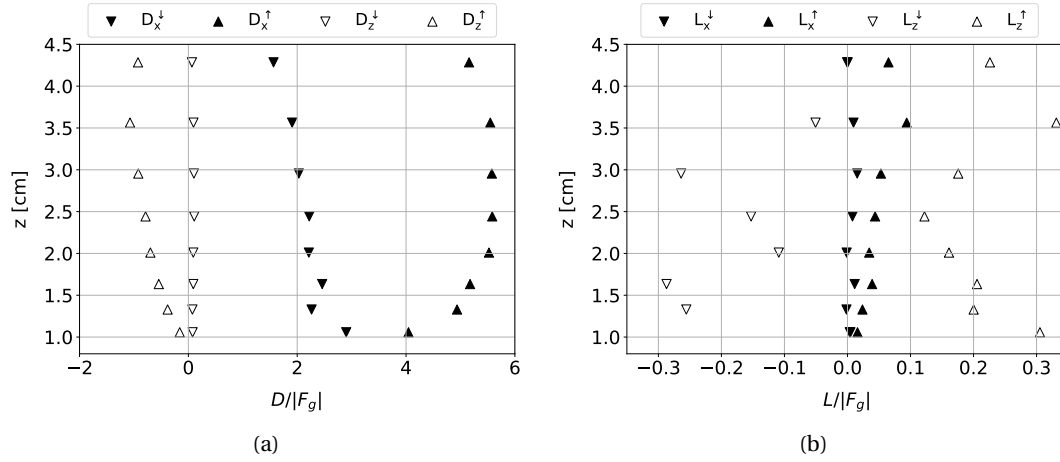
Figure A.6: Mean drag force (a) and lift force (b) (normalized by gravity) felt by snow particles at varying heights above the snow surface. Profiles are separated into streamwise ($x$) and vertical ($z$) components as well as by upward and downward moving populations.

direction applied to the downward moving particles is almost null.

In Figure A.7, the probability density function of the ratio between the experimentally-determined drag coefficient, and the one given by Schiller-Naumann (Clift et al., 1978) for a sphere of an equivalent diameter is presented. The expression of Schiller-Naumann is currently used in the LES-LSM model (see section 3.2). While the mode of the distribution is not far from 1, Schiller-Naumann generally underestimates the drag coefficient, by up to eight times its predicted value. On average, the experimental drag coefficient is 2.5 times that of Schiller-Naumann, highlighting the need to better assess the aerodynamic properties of snow particles in saltation.

Unlike the results presented in Figures A.4, A.5 and A.6, the computed drag coefficient is a function of the particle mass and frontal area. Therefore, it depends on the assumed particle density, shape and size. In the current calculations, the particles are assumed spherical and the 2D shadowgraphy images are used to estimate the average particle diameter. Moreover, the particles are assumed to have the density of ice ($917 \, \text{kg m}^{-3}$). Both assumptions might not be appropriate to characterize fresh snow particles saltating over a limited fetch. Indeed, the reduced number of impacts with the surface restricts the occurrence of particle fragmentation, rounding and densification. The uncertainties regarding the particle mass and frontal area hinder the accuracy of the current drag coefficient estimates. Nevertheless, the disagreement between the experimentally-determined drag coefficient and the expression of Schiller-Naumann shown in Figure A.7 highlights the need to assess the validity of these different assumptions.

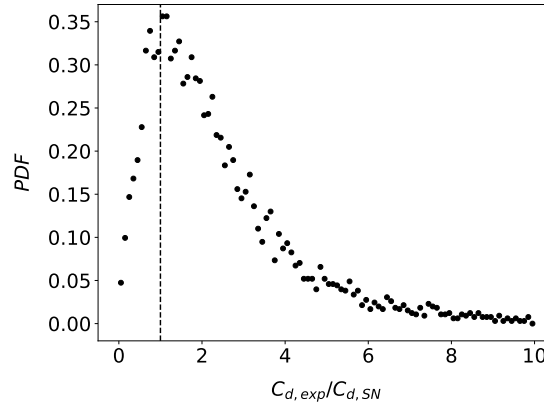Figure A.7: Probability density function of the ratio between the experimentally-determined drag coefficient, versus the Schiller-Naumann coefficient for spheres of an equivalent diameter (Clift et al., 1978). The vertical dashed line indicates a ratio of 1.

## A.4   Conclusion

The dynamics of saltating snow was experimentally studied in a wind tunnel using time-resolved PTV. The experimental setup allowed the measurement of the particle velocity and acceleration in the first 5 cm above the snow surface, as well as the calculation of the drag and lift forces applied to the saltating particles along their trajectories.

The observed profiles of particle velocity and acceleration can be explained in light of the theoretical understanding of the saltation process. In addition, they reveal the weak contribution of the aerodynamic force in the vertical motion of the downward moving particles. By dividing the aerodynamic force into its drag and lift components, it can be seen that drag is indeed larger than lift by approximately one order of magnitude. These results validate the typical assumption of neglecting lift in comparison to drag, which is used in several saltation models. In addition, the analysis revealed that the experimentally-determined drag coefficient is significantly higher than the one derived for spherical particles with the same characteristic diameter. This observation puts into question two commonly used assumptions: the spherical shape of saltating particles and that they have approximately the density of ice. Therefore, further investigation is needed to improve our understanding of the shape, size and density of snow particles in saltation.

The experimental analysis of snow saltation is a challenging endeavor for multiple reasons. Firstly, the use of naturally deposited snow restricts the number of experiments that can be performed during one experimental campaign. Secondly, the fact that the resultant snow layer exhibits different characteristics depending on the meteorological conditions upon formation in the clouds, during deposition and at the subsequent hours before the experiments hinders the development of experimental measurements under repeatable conditions. Taking into account these limitations, the experimental study of snow saltation requires a precise characterization of the snow cover. This is attempted in this study with the use of the SMP.

However, a clear link between resistance force and snow density was not obtained, probably due to the use of fresh snow in the experiments. Therefore, other snow properties such as grain size, shape, hand hardness index and temperature must also be assessed in order to ensure a more complete characterization of the snow cover.

Regarding the use of PTV techniques, the fast increase of the near-surface particle concentration with the wind velocity limits the range of wind velocities for which particle detection and tracking can be successfully attained. This limits the study of snow saltation dynamics over a large range of friction velocities. Nevertheless, wind tunnel experiments based on imaging techniques provide remarkable details about the saltation dynamics and kinematics, which are difficult to attain with other measurement techniques. These detailed observations are ideal for model validation and the development of improved parameterizations for large-scale models.

# B Supplementary results

In this appendix, supplementary results obtained with the standard CRYOWRF simulations described in chapter 6 are shown. Figure B.1 presents the same quantities depicted in Figure 6.1, but refers to the month of November 2014.
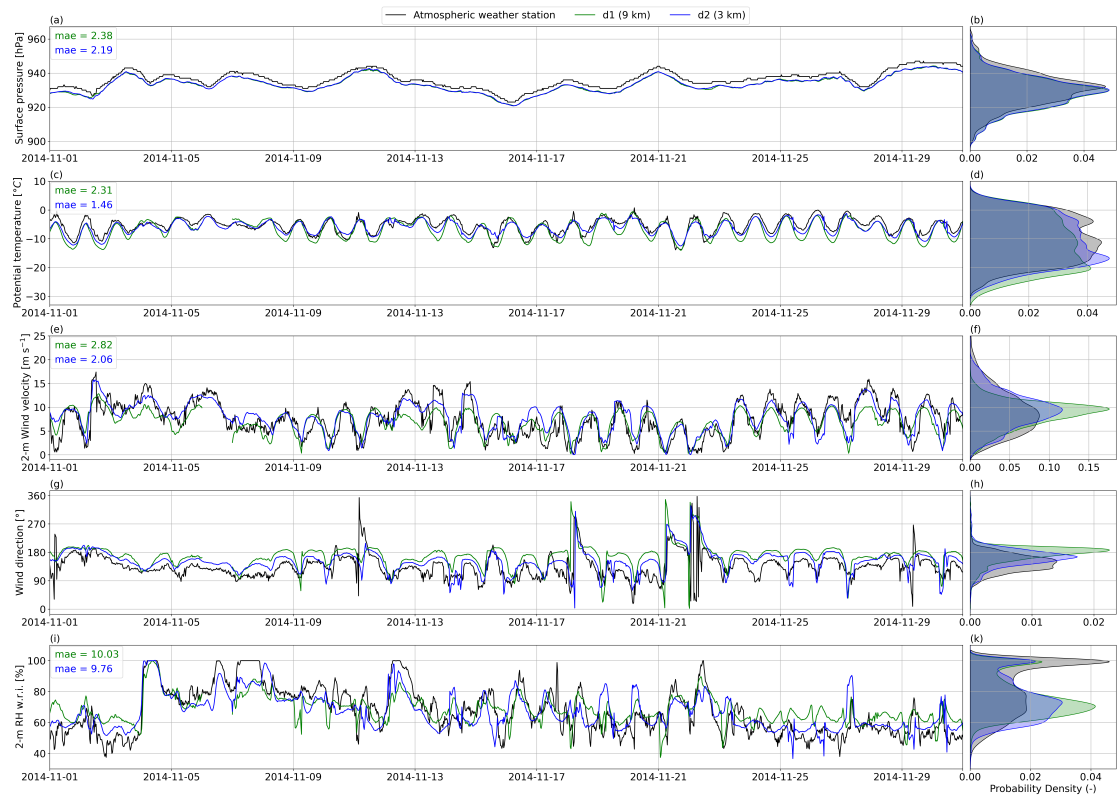


Figure B.1: Time series of 30-mnt averaged surface pressure (a), 2-m potential temperature (c), 2-m horizontal wind velocity (e), wind direction (g), and 2-m relative humidity w.r.i. (i) obtained from the atmospheric weather station at D17 and the 9-km and 3-km resolution simulations at D17, d1 and d2, respectively (November 2014). Results obtained with the standard settings. On the upper left corner of each time series, *mae* indicates the mean absolute error regarding the full simulation time period (1 September 2014 - 1 September 2015) obtained for each variable and for each domain. The probability density functions obtained from the 1-year time series of the measurements at D17 and the simulations are presented for each variable on the right-hand side of each time series (b, d, f, h, k).

Similarly, Figure B.2 portrays the same variables depicted in Figure 6.3, but refers to the months of September and October 2014.
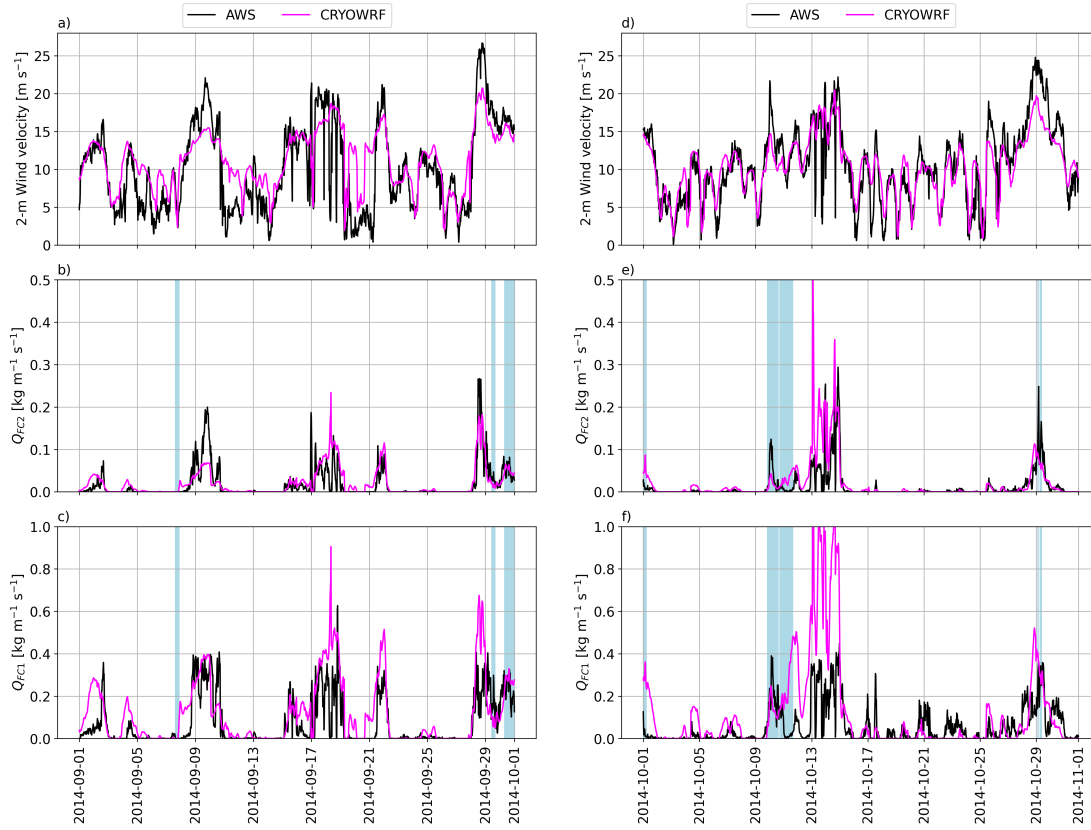


Figure B.2: Time series of 30-minute averaged 2-m horizontal wind velocity (a and d), upper FlowCapt transport rate (b and e) and lower FlowCapt transport rate (c and f) obtained from the automatic weather station and the 3-km resolution simulation at D17. Results obtained with the standard settings. The panels on the left correspond to the month of September 2014, while the panels on the right correspond to the month of October 2014. The vertical bars on the middle and lower panels indicate the occurrence of snowfall events with a minimum intensity of 0.025 mm w.e. Note that the limits of the y-axis differ from those considered in Figure 6.3.

# Bibliography

Aksamit, N. O., & Pomeroy, J. W. (2016). Near-surface snow particle dynamics from particle tracking velocimetry and turbulence measurements during alpine blowing snow storms. *The Cryosphere, 10*(6), 3043–3062. https://doi.org/10.5194/tc-10-3043-2016

Aksamit, N. O., & Pomeroy, J. W. (2018). Scale Interactions in Turbulence for Mountain Blowing Snow. *Journal of Hydrometeorology, 19*(2), 305–320. https://doi.org/10.1175/JHM-D-17-0179.1

Albertson, J. D., & Parlange, M. B. (1999). Natural integration of scalar fluxes from complex terrain. *Advances in Water Resources, 23*, 239–252. https://doi.org/10.1016/S0309-1708(99)00011-1

Almeida, M. P., Andrade, J. S., & Herrmann, H. J. (2006). Aeolian Transport Layer. *Physical Review Letters, 96*(1), 018001. https://doi.org/10.1103/PhysRevLett.96.018001

Ammi, M., Oger, L., Beladjine, D., & Valance, A. (2009). Three-dimensional analysis of the collision process of a bead on a granular packing. *Physical Review E : Statistical, Nonlinear, and Soft Matter Physics, 79*, 021305. https://doi.org/10.1103/PhysRevE.79.021305

Amory, C., Trouvilliez, A., Gallée, H., Favier, V., Naaim-Bouvet, F., Genthon, C., Agosta, C., Piard, L., & Bellot, H. (2015). Comparison between observed and simulated aeolian snow mass fluxes in Adélie Land, East Antarctica. *The Cryosphere, 9*(4), 1373–1383. https://doi.org/10.5194/tc-9-1373-2015

Amory, C. (2020). Drifting-snow statistics from multiple-year autonomous measurements in Adélie Land, East Antarctica. *The Cryosphere, 14*(5), 1713–1725. https://doi.org/10.5194/tc-14-1713-2020

Amory, C., Gallée, H., Naaim-Bouvet, F., Favier, V., Vignon, E., Picard, G., Trouvilliez, A., Piard, L., Genthon, C., & Bellot, H. (2017). Seasonal Variations in Drag Coefficient over a Sastrugi-Covered Snowfield in Coastal East Antarctica. *Boundary-Layer Meteorology, 164*(1), 107–133. https://doi.org/10.1007/s10546-017-0242-5

Amory, C., Genthon, C., & Favier, V. (2020). A drifting snow data set (2010-2018) from coastal Adelie Land, Eastern Antarctica [Dataset]. *Zenodo.* https://doi.org/10.5281/zenodo.3630497

Amory, C., Kittel, C., Le Toumelin, L., Agosta, C., Delhasse, A., Favier, V., & Fettweis, X. (2021). Performance of MAR (v3.11) in simulating the drifting-snow climate and surface mass

balance of Adélie Land, East Antarctica. *Geoscientific Model Development, 14*(6), 3487–3510. https://doi.org/10.5194/gmd-14-3487-2021

AMS American Meteorological Society. (2012). *Glossary of Meteorology: Drifting Snow*. Retrieved July 25, 2023, from https://glossary.ametsoc.org/wiki/Drifting_snow

Anderson, R. S., & Haff, P. K. (1988). Simulation of Eolian Saltation. *Science, 241*(4867), 820–823. https://doi.org/10.1126/science.241.4867.820

Anderson, R. S., & Haff, P. K. (1991). Wind modification and bed response during saltation of sand in air. In O. E. Barndorff-Nielsen & B. B. Willetts (Eds.), *Aeolian grain transport 1* (pp. 21–51). Springer Vienna.

Anderson, R. S., & Hallet, B. (1986). Sediment transport by wind: Toward a general model. *GSA Bulletin, 97*(5), 523–535. https://doi.org/10.1130/0016-7606(1986)97<523:STBWTA>2.0.CO;2

Anderson, R. S., Sørensen, M., & Willetts, B. B. (1991). A review of recent progress in our understanding of aeolian sediment transport. In O. E. Barndorff-Nielsen & B. B. Willetts (Eds.), *Aeolian grain transport 1* (pp. 1–19). Springer Vienna.

Araoka, K., & Maeno, N. (1981). Dynamical behaviors of snow particles in the saltation layer. *Proceedings of the Third Symposium on Polar Meteorology and Glaciology, 19*, 253–263.

Bagnold, R. A. (1941). *The physics of blown sand and desert dunes*. Dover Publications.

Bagnold, R. A. (1973). The nature of saltation and of 'bed-load' transport in water. *Proceedings of the Royal Society of London A, 332*(1591), 473–504. https://doi.org/10.1098/rspa.1973.0038

Bauer, B. O., & Davidson-Arnott, R. G. D. (2014). Aeolian particle flux profiles and transport unsteadiness. *Journal of Geophysical Research: Earth Surface, 119*(7), 1542–1563. https://doi.org/10.1002/2014JF003128

Boisramé, G. F. S., & Carroll, R. W. H. (2023). Exploring Climate-Driven agricultural water shortages in a Snow-Fed basin using a water allocation model and Machine learning. *Journal of Hydrology, 621*, 129605. https://doi.org/10.1016/j.jhydrol.2023.129605

Bou-Zeid, E., Meneveau, C., & Parlange, M. (2005). A scale-dependent Lagrangian dynamic model for large eddy simulation of complex turbulent flows. *Physics of Fluids, 17*(2), 025105. https://doi.org/10.1063/1.1839152

Budd, W. F. (1966). The Drifting of Nonuniform Snow Particles. In *Studies in Antarctic Meteorology* (pp. 59–70). https://doi.org/10.1029/AR009p0059

Calonne, N., Richter, B., Löwe, H., Cetti, C., ter Schure, J., Van Herwijnen, A., Fierz, C., Jaggi, M., & Schneebeli, M. (2020). The RHOSSA campaign: multi-resolution monitoring of the seasonal evolution of the structure and mechanical stability of an alpine snowpack. *The Cryosphere, 14*(6), 1829–1848. https://doi.org/10.5194/tc-14-1829-2020

Canuto, C., Hussaini, M. Y., Quarteroni, A., & Zang, T. A. (1988). *Spectral Methods in Fluid Dynamics*. Springer Berlin, Heidelberg.

Chepil, W. S. (1959). Equilibrium of Soil Grains at the Threshold of Movement by Wind. *Soil Science Society of America, 23*(6), 422–428. https://doi.org/10.2136/sssaj1959.03615995002300060019x

Chritin, V., Bolognesi, R., & Gubler, H. (1999). FlowCapt: a new acoustic sensor to measure snowdrift and wind velocity for avalanche forecasting. *Cold Regions Science and Technology, 30*(1), 125–133. https://doi.org/10.1016/S0165-232X(99)00012-9

Clift, R., Grace, J., Weber, M., & Weber, M. (1978). *Bubbles, drops, and particles*. Academic Press.

Clifton, A., & Lehning, M. (2008). Improvement and validation of a snow saltation model using wind tunnel measurements. *Earth Surface Processes and Landforms, 33*(14), 2156–2173. https://doi.org/10.1002/esp.1673

Clifton, A., Rüedi, J.-D., & Lehning, M. (2006). Snow saltation threshold measurements in a drifting-snow wind tunnel. *Journal of Glaciology, 52*(179), 585–596. https://doi.org/10.3189/172756506781828430

Comola, F., Gaume, J., Kok, J. F., & Lehning, M. (2019). Cohesion-Induced Enhancement of Aeolian Saltation. *Geophysical Research Letters, 46*(10), 5566–5574. https://doi.org/10.1029/2019GL082195

Comola, F., Giometto, M. G., Salesky, S. T., Parlange, M. B., & Lehning, M. (2019). Preferential deposition of snow and dust over hills: governing processes and relevant scales. *Journal of Geophysical Research: Atmospheres, 124*(14), 7951–7974. https://doi.org/10.1029/2018JD029614

Comola, F., Kok, J. F., Lora, J. M., Cohanim, K., Yu, X., He, C., McGuiggan, P., Hörst, S. M., & Turney, F. (2022). Titan's Prevailing Circulation Might Drive Highly Intermittent, Yet Significant Sediment Transport. *Geophysical Research Letters, 49*(7), e2022GL097913. https://doi.org/10.1029/2022GL097913

Comola, F. (2017). *Stochastic modeling of snow transport and hydrologic response in alpine terrain* (Doctoral dissertation). Ecole Polytechnique Fédérale de Lausanne. Lausanne, Switzerland.

Comola, F., Kok, J. F., Gaume, J., Paterna, E., & Lehning, M. (2017). Fragmentation of wind-blown snow crystals. *Geophysical Research Letters, 44*(9), 4195–4203. https://doi.org/https://doi.org/10.1002/2017GL073039

Comola, F., & Lehning, M. (2017). Energy- and momentum-conserving model of splash entrainment in sand and snow saltation. *Geophysical Research Letters, 44*(3), 1601–1609. https://doi.org/10.1002/2016GL071822

Creyssels, M., Dupont, P., Moctar, A. O. E., Valance, A., Cantat, I., Jenkins, J. T., Pasini, J. M., & Rasmussen, K. R. (2009). Saltating particles in a turbulent boundary layer: experiment and theory. *Journal of Fluid Mechanics, 625*, 47–74. https://doi.org/10.1017/S0022112008005491

Crivelli, P., Paterna, E., Horender, S., & Lehning, M. (2016). Quantifying Particle Numbers and Mass Flux in Drifting Snow. *Boundary-Layer Meteorology, 161*(3), 519–542. https://doi.org/10.1007/s10546-016-0170-9

Dai, X., & Huang, N. (2014). Numerical simulation of drifting snow sublimation in the saltation layer. *Scientific Reports, 4*(1), 6611. https://doi.org/10.1038/srep06611

Déry, S. J., Taylor, P., & Xiao, J. (1998). The Thermodynamic Effects of Sublimating, Blowing Snow in the Atmospheric Boundary Layer. *Boundary-Layer Meteorology*, *89*(2), 251–283. https://doi.org/10.1023/A:1001712111718

Déry, S. J., & Yau, M. K. (1999). A Bulk Blowing Snow Model. *Boundary-Layer Meteorology*, *93*(2), 237–251. https://doi.org/10.1023/A:1002065615856

Diebold, M., Higgins, C., Fang, J., Bechmann, A., & Parlange, M. B. (2013). Flow over Hills: A Large-Eddy Simulation of the Bolund Case. *Boundary-Layer Meteorology*, *148*(1), 177–194. https://doi.org/10.1007/s10546-013-9807-0

Dietrich, W. E. (1982). Settling velocity of natural particles. *Water Resources Research*, *18*(6), 1615–1626. https://doi.org/10.1029/WR018i006p01615

Dong, Z., Liu, X., Wang, H., & Wang, X. (2003). Aeolian sand transport: a wind tunnel model. *Sedimentary Geology*, *161*(1), 71–83. https://doi.org/10.1016/S0037-0738(02)00396-2

Doorschot, J., & Lehning, M. (2002). Equilibrium Saltation: Mass Fluxes, Aerodynamic Entrainment, and Dependence on Grain Properties. *Boundary-Layer Meteorology*, *104*(1), 111–130. https://doi.org/10.1023/A:1015516420286

Doorschot, J., Lehning, M., & Vrouwe, A. (2004). Field measurements of snow-drift threshold and mass fluxes, and related model simulations. *Boundary-Layer Meteorology*, *113*(3), 347–368. https://doi.org/10.1007/s10546-004-8659-z

Dupont, S., Bergametti, G., Marticorena, B., & Simoëns, S. (2013). Modeling saltation intermittency. *Journal of Geophysical Research: Atmospheres*, *118*(13), 7109–7128. https://doi.org/10.1002/jgrd.50528

Durán, O., Claudin, P., & Andreotti, B. (2011). On aeolian transport: Grain-scale interactions, dynamical mechanisms and scaling laws. *Aeolian Research*, *3*(3), 243–270. https://doi.org/10.1016/j.aeolia.2011.07.006

Durán, O., Andreotti, B., & Claudin, P. (2012). Numerical simulation of turbulent sediment transport, from bed load to saltation. *Physics of Fluids*, *24*(10), 103306. https://doi.org/10.1063/1.4757662

Fierz, C., Armstrong, R. L., Durand, Y., Etchevers, P, Greene, E., McClung, D. M., Nishimura, K., Satyawali, P. K., & Sokratov, S. A. (2009). *The international classification for seasonal snow on the ground.* IHP–VII Technical Documents in Hydrology, No 83, IACS contribution No 1, UNESCO-IHP.

Filhol, S., & Sturm, M. (2015). Snow bedforms: A review, new data, and a formation model. *Journal of Geophysical Research: Earth Surface*, *120*(9), 1645–1669. https://doi.org/10.1002/2015JF003529

Gallée, H. (1998). Simulation of blowing snow over the antarctic ice sheet. *Annals of Glaciology*, *26*, 203–206. https://doi.org/10.3189/1998AoG26-1-203-206

Gauer, P. (2001). Numerical modeling of blowing and drifting snow in Alpine terrain. *Journal of Glaciology*, *47*(156), 97–110. https://doi.org/10.3189/172756501781832476

Gaume, J., & Puzrin, A. M. (2021). Mechanisms of slab avalanche release and impact in the Dyatlov Pass incident in 1959. *Communications Earth & Environment*, *2*(1), 1–11. https://doi.org/10.1038/s43247-020-00081-8

Gerber, F., Sharma, V., & Lehning, M. (2022). Reproducibility dataset for CRYOWRF validation [Dataset]. *EnviDat.* https://doi.org/10.16904/envidat.347

Gerber, F., Sharma, V., & Lehning, M. (2023). CRYOWRF—Model Evaluation and the Effect of Blowing Snow on the Antarctic Surface Mass Balance. *Journal of Geophysical Research: Atmospheres, 128*(12), e2022JD037744. https://doi.org/10.1029/2022JD037744

Giometto, M. G., Christen, A., Egli, P. E., Schmid, M. F., Tooke, R. T., Coops, N. C., & Parlange, M. B. (2017). Effects of trees on mean wind, turbulence and momentum exchange within and above a real urban environment. *Advances in Water Resources, 106*, 154–168. https://doi.org/10.1016/j.advwatres.2017.06.018

Giometto, M. G., Christen, A., Meneveau, C., Fang, J., Krafczyk, M., & Parlange, M. B. (2016). Spatial Characteristics of Roughness Sublayer Mean Flow and Turbulence Over a Realistic Urban Surface. *Boundary-Layer Meteorology, 160*(3), 425–452. https://doi.org/10.1007/s10546-016-0157-6

Goff, J. A., & Gratch, S. (1945). Thermodynamic properties of moist air. *ASHVE Transactions, 51*, 125–157.

Gordon, M., Savelyev, S., & Taylor, P. A. (2009). Measurements of blowing snow, part II: Mass and number density profiles and saltation height at Franklin Bay, NWT, Canada. *Cold Regions Science and Technology, 55*(1), 75–85. https://doi.org/10.1016/j.coldregions.2008.07.001

Gordon, M., & Taylor, P. A. (2009). Measurements of blowing snow, Part I: Particle shape, size distribution, velocity, and number flux at Churchill, Manitoba, Canada. *Cold Regions Science and Technology, 55*(1), 63–74. https://doi.org/10.1016/j.coldregions.2008.05.001

Groot Zwaaftink, C. D., Diebold, M., Horender, S., Overney, J., Lieberherr, G., Parlange, M. B., & Lehning, M. (2014). Modelling Small-Scale Drifting Snow with a Lagrangian Stochastic Model Based on Large-Eddy Simulations. *Boundary-Layer Meteorology, 153*(1), 117–139. https://doi.org/10.1007/s10546-014-9934-2

Guala, M., Manes, C., Clifton, A., & Lehning, M. (2008). On the saltation of fresh snow in a wind tunnel: Profile characterization and single particle statistics. *Journal of Geophysical Research: Earth Surface, 113*(F3). https://doi.org/10.1029/2007JF000975

Hancock, H., Eckerstorfer, M., Prokop, A., & Hendrikx, J. (2020). Quantifying seasonal cornice dynamics using a terrestrial laser scanner in Svalbard, Norway. *Natural Hazards and Earth System Sciences, 20*(2), 603–623. https://doi.org/10.5194/nhess-20-603-2020

Hersbach, H., Bell, B., Berrisford, P., Hirahara, S., Horányi, A., Muñoz-Sabater, J., Nicolas, J., Peubey, C., Radu, R., Schepers, D., Simmons, A., Soci, C., Abdalla, S., Abellan, X., Balsamo, G., Bechtold, P., Biavati, G., Bidlot, J., Bonavita, M., ... Thépaut, J.-N. (2020). The ERA5 global reanalysis. *Quarterly Journal of the Royal Meteorological Society, 146*(730), 1999–2049. https://doi.org/10.1002/qj.3803

Ho, T. D., Valance, A., Dupont, P., & Ould El Moctar, A. (2011). Scaling Laws in Aeolian Sand Transport. *Physical Review Letters, 106*(9), 094501. https://doi.org/10.1103/PhysRevLett.106.094501

Hofer, S., Amory, C., Kittel, C., Carlsen, T., Le Toumelin, L., & Storelvmo, T. (2021). The Contribution of Drifting Snow to Cloud Properties and the Atmospheric Radiative Budget Over Antarctica. *Geophysical Research Letters*, *48*(22), e2021GL094967. https://doi.org/10.1029/2021GL094967

Howat, I. M., Porter, C., Smith, B. E., Noh, M.-J., & Morin, P. (2019). The Reference Elevation Model of Antarctica. *The Cryosphere*, *13*(2), 665–674. https://doi.org/10.5194/tc-13-665-2019

Huang, N., Wang, C., & Pan, X. (2010). Simulation of aeolian sand saltation with rotational motion. *Journal of Geophysical Research: Atmospheres*, *115*(D22). https://doi.org/10.1029/2009JD013593

Huang, N., Zhang, Y., & D'Adamo, R. (2007). A model of the trajectories and midair collision probabilities of sand particles in a steady state saltation cloud. *Journal of Geophysical Research: Atmospheres*, *112*(D8). https://doi.org/10.1029/2006JD007480

Hui, F., Kang, J., Liu, Y., Cheng, X., Gong, P., Wang, F., Li, Z., Ye, Y., & Guo, Z. (2017). AntarcticaLC2000: The new Antarctic land cover database for the year 2000. *Science China Earth Sciences*, *60*(4), 686–696. https://doi.org/10.1007/s11430-016-0029-2

Jiménez, J. (2004). Turbulent Flows over Rough Walls. *Annual Review of Fluid Mechanics*, *36*, 173–196. https://doi.org/10.1146/annurev.fluid.36.050802.122103

Kawamura, R. (1951). Study of sand movement by wind [NASA Technical Translation (NASA-TT-F-14215), 1972]. *Reports of Physical Sciences Research Institute of Tokyo University*, (5).

Khvorostyanov, V. I., & Curry, J. A. (2002). Terminal Velocities of Droplets and Crystals: Power Laws with Continuous Parameters over the Size Spectrum. *Journal of the Atmospheric Sciences*, *59*(11), 1872–1884. https://doi.org/10.1175/1520-0469(2002)059<1872:TVODAC>2.0.CO;2

Kok, J. F., Parteli, E. J. R., Michaels, T. I., & Karam, D. B. (2012). The physics of wind-blown sand and dust. *Reports on Progress in Physics*, *75*(10), 106901. https://doi.org/10.1088/0034-4885/75/10/106901

Kok, J. F., & Renno, N. O. (2006). Enhancement of the emission of mineral dust aerosols by electric forces. *Geophysical Research Letters*, *33*(19). https://doi.org/10.1029/2006GL026284

Kok, J. F., & Renno, N. O. (2008). Electrostatics in Wind-Blown Sand. *Physical Review Letters*, *100*(1), 014501. https://doi.org/10.1103/PhysRevLett.100.014501

Kok, J. F., & Renno, N. O. (2009). A comprehensive numerical model of steady state saltation (COMSALT). *Journal of Geophysical Research: Atmospheres*, *114*(D17). https://doi.org/10.1029/2009JD011702

Kuipers Munneke, P., van den Broeke, M. R., Lenaerts, J. T. M., Flanner, M. G., Gardner, A. S., & van de Berg, W. J. (2011). A new albedo parameterization for use in climate models over the Antarctic ice sheet. *Journal of Geophysical Research: Atmospheres*, *116*(D5). https://doi.org/10.1029/2010JD015113

Lämmel, M., Dzikowski, K., Kroy, K., Oger, L., & Valance, A. (2017). Grain-scale modeling and splash parametrization for aeolian sand transport. *Physical Review E, 95*(2), 022902. https://doi.org/10.1103/PhysRevE.95.022902

Lehning, M., Löwe, H., Ryser, M., & Raderschall, N. (2008). Inhomogeneous precipitation distribution and snow transport in steep terrain. *Water Resources Research, 44*(7). https://doi.org/10.1029/2007WR006545

Lehning, M., Bartelt, P., Brown, B., Russi, T., Stöckli, U., & Zimmerli, M. (1999). SNOWPACK model calculations for avalanche warning based upon a new network of weather and snow stations. *Cold Regions Science and Technology, 30*(1), 145–157. https://doi.org/10.1016/S0165-232X(99)00022-1

Lehning, M., Doorschot, J., & Bartelt, P. (2000). A snowdrift index based on SNOWPACK model calculations. *Annals of Glaciology, 31*, 382–386. https://doi.org/10.3189/172756400781819770

Leinonen, J., Lebsock, M. D., Tanelli, S., Sy, O. O., Dolan, B., Chase, R. J., Finlon, J. A., von Lerber, A., & Moisseev, D. (2018). Retrieval of snowflake microphysical properties from multifrequency radar observations. *Atmospheric Measurement Techniques, 11*(10), 5471–5488. https://doi.org/10.5194/amt-11-5471-2018

Lenaerts, J. T. M., & van den Broeke, M. R. (2012). Modeling drifting snow in Antarctica with a regional climate model: 2. Results. *Journal of Geophysical Research: Atmospheres, 117*(D5). https://doi.org/10.1029/2010JD015419

Lenaerts, J. T. M., van den Broeke, M. R., Déry, S. J., van Meijgaard, E., van de Berg, W. J., Palm, S. P., & Sanz Rodrigo, J. (2012). Modeling drifting snow in Antarctica with a regional climate model: 1. Methods and model evaluation. *Journal of Geophysical Research: Atmospheres, 117*(D5). https://doi.org/10.1029/2011JD016145

Li, B., & McKenna Neuman, C. (2012). Boundary-layer turbulence characteristics during aeolian saltation. *Geophysical Research Letters, 39*(11). https://doi.org/10.1029/2012GL052234

Li, G., Zhang, J., Herrmann, H. J., Shao, Y., & Huang, N. (2020). Study of Aerodynamic Grain Entrainment in Aeolian Transport. *Geophysical Research Letters, 47*(11), e2019GL086574. https://doi.org/10.1029/2019GL086574

Liston, G., & Sturm, M. (2004). The role of winter sublimation in the Arctic moisture budget. *Hydrology Research, 35*(4-5), 325–334. https://doi.org/10.2166/nh.2004.0024

Maccario, L., Sanguino, L., Vogel, T. M., & Larose, C. (2015). Snow and ice ecosystems: not so extreme. *Research in Microbiology, 166*(10), 782–795. https://doi.org/10.1016/j.resmic.2015.09.002

Martin, R. L., & Kok, J. F. (2017). Wind-invariant saltation heights imply linear scaling of aeolian saltation flux with shear stress. *Science Advances, 3*(6), e1602569. https://doi.org/10.1126/sciadv.1602569

Martin, R. L., Kok, J. F., Hugenholtz, C. H., Barchyn, T. E., Chamecki, M., & Ellis, J. T. (2018). High-frequency measurements of aeolian saltation flux: Field-based methodology and applications. *Aeolian Research, 30*, 97–114. https://doi.org/10.1016/j.aeolia.2017.12.003

## BIBLIOGRAPHY

Maxey, M. R., & Riley, J. J. (1983). Equation of motion for a small rigid sphere in a nonuniform flow. *The Physics of Fluids*, *26*(4), 883–889. https://doi.org/10.1063/1.864230

McEwan, I. K., & Willetts, B. B. (1991). Numerical model of the saltation cloud. In O. E. Barndorff-Nielsen & B. B. Willetts (Eds.), *Aeolian grain transport 1* (pp. 53–66). Springer Vienna.

Mitchell, D. L. (1996). Use of Mass- and Area-Dimensional Power Laws for Determining Precipitation Particle Terminal Velocities. *Journal of the Atmospheric Sciences*, *53*(12), 1710–1723. https://doi.org/10.1175/1520-0469(1996)053<1710:UOMAAD>2.0.CO;2

Morrison, H., & Grabowski, W. W. (2008). A Novel Approach for Representing Ice Microphysics in Models: Description and Tests Using a Kinematic Framework. *Journal of the Atmospheric Sciences*, *65*(5), 1528–1548. https://doi.org/10.1175/2007JAS2491.1

Mott, R., & Lehning, M. (2010). Meteorological Modeling of Very High-Resolution Wind Fields and Snow Deposition for Mountains. *Journal of Hydrometeorology*, *11*(4), 934–949. https://doi.org/10.1175/2010JHM1216.1

Munters, W., Meneveau, C., & Meyers, J. (2016). Shifted periodic boundary conditions for simulations of wall-bounded turbulent flows. *Physics of Fluids*, *28*(2), 025112. https://doi.org/10.1063/1.4941912

Nalpanis, P., Hunt, J. C. R., & Barrett, C. F. (1993). Saltating particles over flat beds. *Journal of Fluid Mechanics*, *251*, 661–685. https://doi.org/10.1017/S0022112093003568

Namikas, S. L. (2003). Field measurement and numerical modelling of aeolian mass flux distributions on a sandy beach. *Sedimentology*, *50*(2), 303–326. https://doi.org/10.1046/j.1365-3091.2003.00556.x

Nemoto, M., & Nishimura, K. (2004). Numerical simulation of snow saltation and suspension in a turbulent boundary layer. *Journal of Geophysical Research: Atmospheres*, *109*(D18). https://doi.org/10.1029/2004JD004657

Niiya, H., & Nishimura, K. (2017). Spatiotemporal Structure of Aeolian Particle Transport on Flat Surface. *Journal of the Physical Society of Japan*, *86*(5), 054402. https://doi.org/10.7566/JPSJ.86.054402

Niiya, H., & Nishimura, K. (2022). Hysteresis and Surface Shear Stresses During Snow-Particle Aeolian Transportation. *Boundary-Layer Meteorology*, *183*(3), 447–467. https://doi.org/10.1007/s10546-022-00688-8

Nishimura, K., & Hunt, J. C. R. (2000). Saltation and incipient suspension above a flat particle bed below a turbulent boundary layer. *Journal of Fluid Mechanics*, *417*, 77–102. https://doi.org/10.1017/S0022112000001014

Nishimura, K., & Nemoto, M. (2005). Blowing snow at Mizuho station, Antarctica. *Philosophical Transactions of the Royal Society A: Mathematical, Physical and Engineering Sciences*, *363*(1832), 1647–1662. https://doi.org/10.1098/rsta.2005.1599

Nishimura, K., Yokoyama, C., Ito, Y., Nemoto, M., Naaim-Bouvet, F., Bellot, H., & Fujita, K. (2014). Snow particle speeds in drifting snow: Snow particle speeds in drifting snow. *Journal of Geophysical Research: Atmospheres*, *119*(16), 9901–9913. https://doi.org/10.1002/2014JD021686

Okaze, T., Niiya, H., & Nishimura, K. (2018). Development of a large-eddy simulation coupled with Lagrangian snow transport model. *Journal of Wind Engineering and Industrial Aerodynamics*, *183*, 35–43. https://doi.org/10.1016/j.jweia.2018.09.027

Ortner, G., Bründl, M., Kropf, C. M., Röösli, T., Bühler, Y., & Bresch, D. N. (2023). Large-scale risk assessment on snow avalanche hazard in alpine regions. *Natural Hazards and Earth System Sciences*, *23*(6), 2089–2110. https://doi.org/10.5194/nhess-23-2089-2023

Ouellette, N. T., Xu, H., & Bodenschatz, E. (2006). A quantitative study of three-dimensional Lagrangian particle tracking algorithms. *Experiments in Fluids*, *40*(2), 301–313. https://doi.org/10.1007/s00348-005-0068-7

Owen, P. R. (1964). Saltation of uniform grains in air. *Journal of Fluid Mechanics*, *20*(2), 225–242. https://doi.org/10.1017/S0022112064001173

Pähtz, T., Clark, A. H., Valyrakis, M., & Durán, O. (2020). The Physics of Sediment Transport Initiation, Cessation, and Entrainment Across Aeolian and Fluvial Environments. *Reviews of Geophysics*, *58*(1), e2019RG000679. https://doi.org/10.1029/2019RG000679

Pähtz, T., Omeradžić, A., Carneiro, M. V., Araújo, N. A. M., & Herrmann, H. J. (2015). Discrete Element Method simulations of the saturation of aeolian sand transport. *Geophysical Research Letters*, *42*(6), 2063–2070. https://doi.org/https://doi.org/10.1002/2014GL062945

Palm, S. P., Kayetha, V., Yang, Y., & Pauly, R. (2017). Blowing snow sublimation and transport over Antarctica from 11 years of CALIPSO observations. *The Cryosphere*, *11*(6), 2555–2569. https://doi.org/10.5194/tc-11-2555-2017

Paterna, E., Crivelli, P., & Lehning, M. (2016). Decoupling of mass flux and turbulent wind fluctuations in drifting snow. *Geophysical Research Letters*, *43*(9), 4441–4447. https://doi.org/10.1002/2016GL068171

Paterna, E., Crivelli, P., & Lehning, M. (2017). Wind tunnel observations of weak and strong snow saltation dynamics. *Journal of Geophysical Research: Earth Surface*, *122*(9), 1589–1604. https://doi.org/10.1002/2016JF004111

Pomeroy, J. W. (1989). A Process-Based Model of Snow Drifting. *Annals of Glaciology*, *13*, 237–240. https://doi.org/10.3189/S0260305500007965

Pomeroy, J. W., & Gray, D. M. (1990). Saltation of snow. *Water Resources Research*, *26*(7), 1583–1594. https://doi.org/10.1029/WR026i007p01583

Pomeroy, J. W., & Male, D. H. (1992). Steady-state suspension of snow. *Journal of Hydrology*, *136*(1), 275–301. https://doi.org/10.1016/0022-1694(92)90015-N

Prandtl, L. (1935). The mechanics of viscous flows. In W. F. Durand (Ed.), *Aerodynamic Theory III* (pp. 34–208). Springer Berlin.

Raderschall, N., Lehning, M., & Schär, C. (2008). Fine-scale modeling of the boundary layer wind field over steep topography. *Water Resources Research*, *44*(9). https://doi.org/10.1029/2007WR006544

Rasmussen, K. R., & Sørensen, M. (2008). Vertical variation of particle speed and flux density in aeolian saltation: Measurement and modeling. *Journal of Geophysical Research: Earth Surface*, *113*(F2). https://doi.org/10.1029/2007JF000774

Raupach, M. R. (1991). Saltation layers, vegetation canopies and roughness lengths. In O. E. Barndorff-Nielsen & B. B. Willetts (Eds.), *Aeolian grain transport 1* (pp. 83–96). Springer Vienna.

Rees, K. N., Singh, D. K., Pardyjak, E. R., & Garrett, T. J. (2021). Mass and density of individual frozen hydrometeors. *Atmospheric Chemistry and Physics, 21*(18), 14235–14250. https://doi.org/10.5194/acp-21-14235-2021

Rice, M. A., Willetts, B. B., & McEwan, I. K. (1995). An experimental study of multiple grain-size ejecta produced by collisions of saltating grains with a flat bed. *Sedimentology, 42*(4), 695–706. https://doi.org/10.1111/j.1365-3091.1995.tb00401.x

Rice, M. A., Willetts, B. B., & McEwan, I. K. (1996). Observations of collisions of saltating grains with a granular bed from high-speed cine-film. *Sedimentology, 43*(1), 21–31. https://doi.org/10.1111/j.1365-3091.1996.tb01456.x

Robinson, D. A., & Estilow, T. W. (2021). Rutgers Northern Hemisphere 24 km Weekly Snow Cover Extent, September 1980 Onward, Version 1 [Dataset]. *National Snow and Ice Data Center*. https://doi.org/10.7265/zzbm-2w05

Saffman, P. G. (1965). The lift on a small sphere in a slow shear flow. *Journal of Fluid Mechanics, 22*(2), 385–400. https://doi.org/10.1017/S0022112065000824

Sato, T., Kosugi, K., & Sato, A. (2001). Saltation-layer structure of drifting snow observed in wind tunnel. *Annals of Glaciology, 32*, 203–208. https://doi.org/10.3189/172756401781819184

Scarchilli, C., Frezzotti, M., Grigioni, P., De Silvestri, L., Agnoletto, L., & Dolci, S. (2010). Extraordinary blowing snow transport events in East Antarctica. *Climate Dynamics, 34*(7), 1195–1206. https://doi.org/10.1007/s00382-009-0601-0

Schiller, L., & Nauman, A. Z. (1933). Über die grundlegenden Berechnungen bei der Schwersraftaufbereitung. *Zeitschrift des Vereines Deutscher Ingenieure, 77*(12), 318–320.

Schlögl, S., Lehning, M., Nishimura, K., Huwald, H., Cullen, N. J., & Mott, R. (2017). How do Stability Corrections Perform in the Stable Boundary Layer Over Snow? *Boundary-Layer Meteorology, 165*(1), 161–180. https://doi.org/10.1007/s10546-017-0262-1

Schmidt, D. S., Schmidt, R. A., & Dent, J. D. (1998). Electrostatic force on saltating sand. *Journal of Geophysical Research: Atmospheres, 103*(D8), 8997–9001. https://doi.org/10.1029/98JD00278

Schmidt, R. A. (1980). Threshold Wind-Speeds and Elastic Impact in Snow Transport. *Journal of Glaciology, 26*(94), 453–467. https://doi.org/10.3189/S0022143000010972

Schmidt, R. A. (1982). Vertical profiles of wind speed, snow concentration, and humidity in blowing snow. *Boundary-Layer Meteorology, 23*(2), 223–246. https://doi.org/10.1007/BF00123299

Schmidt, R. (1981). Estimates of threshold windspeed from particle sizes in blowing snow. *Cold Regions Science and Technology, 4*(3), 187–193. https://doi.org/10.1016/0165-232X(81)90003-3

Schneebeli, M., Pielmeier, C., & Johnson, J. B. (1999). Measuring snow microstructure and hardness using a high resolution penetrometer. *Cold Regions Science and Technology, 30*(1), 101–114. https://doi.org/10.1016/S0165-232X(99)00030-0

Schultz, M. P., & Flack, K. A. (2007). The rough-wall turbulent boundary layer from the hydraulically smooth to the fully rough regime. *Journal of Fluid Mechanics, 580*, 381–405. https://doi.org/10.1017/S0022112007005502

Shao, Y., Raupach, M. R., & Findlater, P. A. (1993). Effect of saltation bombardment on the entrainment of dust by wind. *Journal of Geophysical Research: Atmospheres, 98*(D7), 12719–12726. https://doi.org/10.1029/93JD00396

Shao, Y., & Li, A. (1999). Numerical Modelling of Saltation in the Atmospheric Surface Layer. *Boundary-Layer Meteorology, 91*(2), 199–225. https://doi.org/10.1023/A:1001816013475

Shao, Y., & Lu, H. (2000). A simple expression for wind erosion threshold friction velocity. *Journal of Geophysical Research: Atmospheres, 105*(D17), 22437–22443. https://doi.org/10.1029/2000JD900304

Shao, Y., & Mikami, M. (2005). Heterogeneous Saltation: Theory, Observation and Comparison. *Boundary-Layer Meteorology, 115*(3), 359–379. https://doi.org/10.1007/s10546-004-7089-2

Sharma, V., Parlange, M. B., & Calaf, M. (2017). Perturbations to the Spatial and Temporal Characteristics of the Diurnally-Varying Atmospheric Boundary Layer Due to an Extensive Wind Farm. *Boundary-Layer Meteorology, 162*(2), 255–282. https://doi.org/10.1007/s10546-016-0195-0

Sharma, V., Comola, F., & Lehning, M. (2018). On the suitability of the Thorpe–Mason model for calculating sublimation of saltating snow. *The Cryosphere, 12*(11), 3499–3509. https://doi.org/10.5194/tc-12-3499-2018

Sharma, V., Gerber, F., & Lehning, M. (2021). Reproducibility Dataset for CRYOWRF v1.0 [Dataset]. *EnviDat.* https://doi.org/10.16904/envidat.232

Sharma, V., Gerber, F., & Lehning, M. (2023). Introducing CRYOWRF v1.0: multiscale atmospheric flow simulations with advanced snow cover modelling. *Geoscientific Model Development, 16*(2), 719–749. https://doi.org/10.5194/gmd-16-719-2023

Sigmund, A., Dujardin, J., Comola, F., Sharma, V., Huwald, H., Melo, D. B., Hirasawa, N., Nishimura, K., & Lehning, M. (2022). Evidence of Strong Flux Underestimation by Bulk Parametrizations During Drifting and Blowing Snow. *Boundary-Layer Meteorology, 182*, 119–146. https://doi.org/10.1007/s10546-021-00653-x

Skamarock, W. C., Klemp, B., Dudhia, J., Gill, O., Liu, Z., Berner, J., Wang, W., Powers, G., Duda, G., Barker, D., & Huang, X.-y. (2019). *A Description of the Advanced Research WRF Model Version 4.1* (tech. rep. No. NCAR/TN-556+STR). https://doi.org/10.5065/1dfh-6p97

Sommer, C. G., Wever, N., Fierz, C., & Lehning, M. (2018). Investigation of a wind-packing event in Queen Maud Land, Antarctica. *The Cryosphere, 12*(9), 2923–2939. https://doi.org/10.5194/tc-12-2923-2018

Sørensen, M. (1991). An analytic model of wind-blown sand transport. In O. E. Barndorff-Nielsen & B. B. Willetts (Eds.), *Aeolian grain transport 1* (pp. 67–81). Springer Vienna.

Sørensen, M. (2004). On the rate of aeolian sand transport. *Geomorphology, 59*(1), 53–62. https://doi.org/10.1016/j.geomorph.2003.09.005

Sotiropoulou, G., Vignon, É., Young, G., Morrison, H., O'Shea, S. J., Lachlan-Cope, T., Berne, A., & Nenes, A. (2021). Secondary ice production in summer clouds over the Antarctic

coast: an underappreciated process in atmospheric models. *Atmospheric Chemistry and Physics*, *21*(2), 755–771. https://doi.org/10.5194/acp-21-755-2021

Steger, C. R., Reijmer, C. H., van den Broeke, M. R., Wever, N., Forster, R. R., Koenig, L. S., Kuipers Munneke, P., Lehning, M., Lhermitte, S., Ligtenberg, S. R. M., Miège, C., & Noël, B. P. Y. (2017). Firn Meltwater Retention on the Greenland Ice Sheet: A Model Comparison. *Frontiers in Earth Science*, *5*. https://doi.org/10.3389/feart.2017.00003

Sugiura, K., Nishimura, K., Maeno, N., & Kimura, T. (1998). Measurements of snow mass flux and transport rate at different particle diameters in drifting snow. *Cold Regions Science and Technology*, *27*(2), 83–89. https://doi.org/10.1016/S0165-232X(98)00002-0

Sulia, K. J., & Harrington, J. Y. (2011). Ice aspect ratio influences on mixed-phase clouds: Impacts on phase partitioning in parcel models. *Journal of Geophysical Research: Atmospheres*, *116*(D21). https://doi.org/10.1029/2011JD016298

Tagliavini, G., McCorquodale, M., Westbrook, C., Corso, P., Krol, Q., & Holzner, M. (2021). Drag coefficient prediction of complex-shaped snow particles falling in air beyond the Stokes regime. *International Journal of Multiphase Flow*, *140*, 103652. https://doi.org/10.1016/j.ijmultiphaseflow.2021.103652

Takeuchi, M. (1980). Vertical profile and Horizontal Increase of Drift-Snow Transport. *Journal of Glaciology*, *26*(94), 481–492. https://doi.org/10.3189/S0022143000010996

Thorpe, A. D., & Mason, B. J. (1966). The evaporation of ice spheres and ice crystals. *British Journal of Applied Physics*, *17*(4), 541–548. https://doi.org/10.1088/0508-3443/17/4/316

Tobias, W., Manfred, S., Klaus, J., Massimiliano, Z., & Bettina, S. (2023). The future of Alpine Run-of-River hydropower production: Climate change, environmental flow requirements, and technical production potential. *Science of The Total Environment*, *890*, 163934. https://doi.org/10.1016/j.scitotenv.2023.163934

Trouvilliez, A., Naaim-Bouvet, F., Bellot, H., Genthon, C., & Gallée, H. (2015). Evaluation of the FlowCapt Acoustic Sensor for the Aeolian Transport of Snow. *Journal of Atmospheric and Oceanic Technology*, *32*(9), 1630–1641. https://doi.org/10.1175/JTECH-D-14-00104.1

Ungar, J. E., & Haff, P. K. (1987). Steady state saltation in air. *Sedimentology*, *34*(2), 289–299.

van den Broeke, M., König-Langlo, G., Picard, G., Kuipers Munneke, P., & Lenaerts, J. (2010). Surface energy balance, melt and sublimation at neumayer station, east antarctica. *Antarctic Science*, *22*(1), 87–96. https://doi.org/10.1017/S0954102009990538

van Wessem, J. M., van de Berg, W. J., Noël, B. P. Y., van Meijgaard, E., Amory, C., Birnbaum, G., Jakobs, C. L., Krüger, K., Lenaerts, J. T. M., Lhermitte, S., Ligtenberg, S. R. M., Medley, B., Reijmer, C. H., van Tricht, K., Trusel, L. D., van Ulft, L. H., Wouters, B., Wuite, J., & van den Broeke, M. R. (2018). Modelling the climate and surface mass balance of polar ice sheets using RACMO2 – Part 2: Antarctica (1979–2016). *The Cryosphere*, *12*(4), 1479–1498. https://doi.org/10.5194/tc-12-1479-2018

Vignon, É., Alexander, S. P., DeMott, P. J., Sotiropoulou, G., Gerber, F., Hill, T. C. J., Marchand, R., Nenes, A., & Berne, A. (2021). Challenging and Improving the Simulation of Mid-Level Mixed-Phase Clouds Over the High-Latitude Southern Ocean. *Journal of*

*Geophysical Research: Atmospheres, 126*(7), e2020JD033490. https://doi.org/10.1029/2020JD033490

Vionnet, V., Martin, E., Masson, V., Guyomarc'h, G., Naaim-Bouvet, F., Prokop, A., Durand, Y., & Lac, C. (2014). Simulation of wind-induced snow transport and sublimation in alpine terrain using a fully coupled snowpack/atmosphere model. *The Cryosphere, 8*(2), 395–415. https://doi.org/10.5194/tc-8-395-2014

Vionnet, V., Martin, E., Masson, V., Lac, C., Naaim Bouvet, F., & Guyomarc'h, G. (2017). High-Resolution Large Eddy Simulation of Snow Accumulation in Alpine Terrain. *Journal of Geophysical Research: Atmospheres, 122*(20), 11, 005–11, 021. https://doi.org/10.1002/2017JD026947

Voth, G. A., Porta, A. L., Crawford, A. M., Alexander, J., & Bodenschatz, E. (2002). Measurement of particle accelerations in fully developed turbulence. *Journal of Fluid Mechanics, 469*, 121–160. https://doi.org/10.1017/S0022112002001842

Walden, V. P., Warren, S. G., & Tuttle, E. (2003). Atmospheric Ice Crystals over the Antarctic Plateau in Winter. *Journal of Applied Meteorology and Climatology, 42*(10), 1391–1405. https://doi.org/10.1175/1520-0450(2003)042<1391:AICOTA>2.0.CO;2

Walter, B., Horender, S., Voegeli, C., & Lehning, M. (2014). Experimental assessment of Owen's second hypothesis on surface shear stress induced by a fluid during sediment saltation. *Geophysical Research Letters, 41*(17), 6298–6305. https://doi.org/10.1002/2014GL061069

Wang, D., Wang, Y., Yang, B., Zhang, W., & Lancaster, N. (2008). Statistical analysis of sand grain/bed collision process recorded by high-speed digital camera. *Sedimentology, 55*(2), 461–470. https://doi.org/10.1111/j.1365-3091.2007.00909.x

Wang, Z., Huang, N., & Pähtz, T. (2019). The Effect of Turbulence on Drifting Snow Sublimation. *Geophysical Research Letters, 46*(20), 11568–11575. https://doi.org/10.1029/2019GL083636

Werner, B. T. (1990). A Steady-State Model of Wind-Blown Sand Transport. *The Journal of Geology, 98*(1), 1–17.

White, B. R., & Schulz, J. C. (1977). Magnus effect in saltation. *Journal of Fluid Mechanics, 81*(3), 497–512. https://doi.org/10.1017/S0022112077002183

Woods, C. P., Stoelinga, M. T., & Locatelli, J. D. (2008). Size Spectra of Snow Particles Measured in Wintertime Precipitation in the Pacific Northwest. *Journal of the Atmospheric Sciences, 65*(1), 189–205. https://doi.org/10.1175/2007JAS2243.1

Xing, M., & He, C. (2013). 3D ejection behavior of different sized particles in the grain-bed collision process. *Geomorphology, 187*, 94–100. https://doi.org/10.1016/j.geomorph.2013.01.002

Yu, H., Li, G., Huang, N., & Lehning, M. (2022). Idealized Study of a Static Electrical Field on Charged Saltating Snow Particles. *Frontiers in Earth Science, 10*.

Yu, H., Li, G., Walter, B., Lehning, M., Zhang, J., & Huang, N. (2023). Wind conditions for snow cornice formation in a wind tunnel. *The Cryosphere, 17*(2), 639–651. https://doi.org/10.5194/tc-17-639-2023

## BIBLIOGRAPHY

Zhang, X., Li, Y., Cui, K., Sun, Y., Zhang, X., Zheng, G., Zhao, M., Wang, B., & Yang, H. (2023). Deciphering the turnover of bacterial groups in winter agricultural soils. *Science of The Total Environment, 891*, 164672. https://doi.org/10.1016/j.scitotenv.2023.164672

# Daniela Brito Melo

📍 Route du Bois 10, 1024 Ecublens VD (Switzerland)

✉ daniela.britomelo@epfl.ch

📱 +41 767821009

🆔 https://orcid.org/0000-0003-1685-9197

**Date of birth** 11 December 1991

**Nationality** Portuguese, Cape Verdean

## RESEARCH EXPERIENCE

### 2018 – Present
### PhD CANDIDATE IN MECHANICS

School of Architecture, Civil and Environmental Engineering (ENAC)
Ecole Polytechnique Fédérale de Lausanne (EPFL)
Lausanne (Switzerland)

**Fluid dynamics & Snow physics:**
- Numerical modeling of atmospheric flows and wind-driven transport of snow using a Large Eddy Simulation flow solver coupled with a Lagrangian stochastic model.
- Analysis and development of parameterizations for large-scale models of blowing snow.
- Numerical simulations using the coupled atmosphere-snowpack model, CRYOWRF.
- Experimental study of snow transport in a wind tunnel.
- Teaching assistant in the MSc course "Physics and Hydrology of Snow".

### 2017 – 2018
### RESEARCH ASSISTANT

Department of Mechanical Engineering
Instituto Superior Técnico (IST) – University of Lisbon
Lisbon (Portugal)

**Aero/hydrodynamics of wind turbines and marine propellers:**
- Development of numerical models based on the lifting line theory.
- Numerical modeling of marine propellers using the RANS model ReFRESCO.
- Model validation: analysis of the flow around the blades and in the wakes.
- Model verification: analysis of the accuracy and precision of numerical models.

## EDUCATION

### 2009 – 2016
### MASTER'S IN MECHANICAL ENGINEERING
### (3 yrs BSc + 2 yrs MSc)

Instituto Superior Técnico (IST) – University of Lisbon
Lisbon (Portugal)

- Aero/hydrodynamics, thermodynamics and energy conversion technologies.
- Applied computation.
- Mechanical design.

129

## SKILLS

**Languages:**
- Portuguese (native)
- English (proficient)
- French (intermediate)

**Programming skills:**
- Languages: FORTRAN, MATLAB, C++, Python
- High-performance computing: MPI, OpenMP
- Linux environment and Shell scripting

## VOLUNTEER WORK

2021 – 2022
### COMMITEE MEMBER FOR DIVERSITY AND INCLUSION
Diversity Office at ENAC (EPFL)

- Preparation of workshops for Bachelor and Master students covering bias awareness and training, harassment and disabilities on the EPFL campus.

2005 – 2017
### SCOUTING
Lisbon (Portugal)

- Planning and supervision of activities for teenagers (outdoor activities and community service).
- Organization of events for up to 80 participants: logistics and moderation of debates.

## PUBLICATIONS & PRESENTATIONS

### JOURNAL ARTICLES

**D. B. Melo**, A. Sigmund, M. Lehning (2023). Understanding snow saltation parameterizations: lessons from theory, experiments and numerical simulations. *EGUsphere* [in review to *The Crysphere*].

**D. B. Melo**, V. Sharma, F. Comola, A. Sigmund, M. Lehning (2022). Modeling snow saltation: the effect of grain size and interparticle cohesion. *J. Geophys. Res. Atmos.*, 127(1), e2021JD035260.

J. Baltazar, **D. B. Melo**, D. Rijpkema (2020). Analysis of the blade boundary-layer flow of a marine propeller using a RANS solver. *Ocean Eng.*, 211, 107633.

**D. B. Melo**, J. Baltazar, J. A. C. Falcão de Campos (2018). A Numerical Wake Alignment Method for Horizontal Axis Wind Turbines with the Lifting Line Theory, *J. Wind Eng. Ind.*, 174, 382-390.

### CONFERENCE PRESENTATIONS

**D. B. Melo**, A. Sigmund, V. Sharma, M. Lehning. Parameterizing snow saltation: the exponential decay of the mass flux profile and its relation to the saltation dynamics, In *IGS International Symposium on Snow*, Davos, September 2022.

**D. B. Melo**, A. Petersen, F. Coletti, B. Walter, M. Jaggi, M. Lehning. High-speed imaging of snow saltation: wind tunnel experiments using natural snow, In *EGU General Assembly*, Vienna & Online, May 2022.

**D. B. Melo**, V. Sharma, F. Gerber, F. Comola, A. Sigmund, M. Lehning. A review in snow saltation dynamics and its implications for the surface mass balance, In *AGU Fall Meeting*, New Orleans LA & Online, December 2021.

**D. B. Melo**, J. Baltazar, J. A. C. Falcão de Campos. A Numerical Wake Alignment Method for Horizontal Axis Wind Turbines with the Lifting Line Theory, In *WINERCOST'17*, Coimbra, April 2017.

### SCIENCE OUTREACH

**D. B. Melo** (2023). Highlighted Paper – Human Errors in Snow Models, *EGU Blogs: Cryospheric Sciences* [Blog]. https://blogs.egu.eu/divisions/cr/2023/05/26/human-errors-in-snow-models/